Search for the decay of a heavy Higgs boson decaying to two light Higgs bosons using a kinematic fit

Dissertation zur Erlangung des Doktorgrades
an der Fakultät für
Mathematik, Informatik und Naturwissenschaften
Fachbereich Physik
Der Universität Hamburg

vorgelegt von
Malte Hoffmann
aus Münster

Hamburg, 2016

Gutachter der Dissertation:	Prof. Dr. Peter Schleper Dr. Alexei Raspereza
Gutachter der Disputation:	Prof. Dr. Erika Garutti Prof. Dr. Johannes Haller Prof. Dr. Günter Sigl

Abstract

The Compact Muon Solenoid (CMS) detector is one of two multi-purpose detectors located underground in the Large Hadron Collider (LHC) tunnel at CERN in Geneva. In this thesis, a search for a heavy Higgs boson decaying to two light Higgs is presented. The search is performed on proton-proton collision data with an integrated luminosity of $2.30\,\mathrm{fb}^{-1}$ and a centre-of-mass energy of 13 TeV recorded by the CMS detector in 2015. To increase the sensitivity of the analysis, a kinematic fitting tool (HHKinFit) tailored to the needs of the analysis is developed. It was first used in the analysis of 8 TeV data [1] and was more recently used in an 13 TeV analysis [2]. Since then, further improvements to the HHKinFit have been implemented. The analysis presented in this thesis will mark the first use of the HHKinFit fit probability to further increase the sensitivity of the analysis. As no excess is observed, exclusion limits on the cross-section times branching ratio of the signal are set and interpreted in the post-Higgs Minimal Supersymmetric Standard Model (hMSSM) and the non-alignment Two Higgs Doublet Model (2HDM).

Zusammenfassung

Der Compact Muon Solenoid (CMS) Detektor ist einer von zwei Mehrzweck-Detektoren die sich im Tunnel des Large Hadron Colliders (LHC) am CERN in Genf befinden. In dieser Arbeit wird eine Suche nach einem schweren Higgs Boson, welches in zwei leichte Higgs Bosonen zerfällt, präsentiert. Untersucht wurden Daten aus Proton-Proton Kollisionen mit einer integrierten Luminosität von $2.30\,\mathrm{fb}^{-1}$ bei einer Schwerpunktsenergie von 13 TeV. Die Daten wurden im Jahr 2015 vom CMS Detektor aufgenommen. Um die Sensitivität der Suche zu erhöhen, wurde ein kinematischer Fit (HHKinFit) entwickelt, der auf die Bedürfnisse der Suche abgestimmt ist. Der HHKinFit wurde zuerst für die Suche in 8 TeV Daten [1] und zuletzt für einer weiteren Suche in 13 TeV Daten [2] benutzt. Nach weiteren Verbesserungen wird in der Analyse dieser Doktorarbeit erstmals die Fitwahrsheinlichkeit des HHKinFits genutzt um die Sensitivität der Analyse weiter zu erhöhen. Da in den Daten kein Überschuss beobactet wird, werden Ausschlussgrenzen auf das Produkt von Wirkungsquerschnitt und Verzweigungsverhältnis bestimmt, die im Rahmen des post-Higgs Minimalen Supersymmetrischen Standardmodells (hMSSM) und des non-alignement Zwei Higgs Doublet Modells interpretiert werden.

Contents

List of Figures

List of Tables

Chapter 1

Introduction

Since the beginning of recorded history, humankind has strived to gain more and more knowledge about the laws of nature and to perceive, as the often quoted Goethe put it, "was die Welt im Innersten zusammenhält" (whatever holds the world together in its inmost folds'). One of the latest endeavours to get closer to the answer of these questions is the Large Hadron Collider (LHC), a particle collider build at CERN in Geneva, Switzerland.

At the LHC, protons are collided with a center-of-mass energy of 13 TeV, the highest energy particle collisions ever created by humans, granting particle physicists access to energy regions never observed before. After ten years of construction, the first proton-proton collisions have finally been observed in November 2009. In the years 2010 and 2011, while the accelerator was running at a center-of-mass energy of 7 TeV, the two multi-purpose experiments CMS and ATLAS were able to collect more than $5\,\mathrm{fb}^{-1}$ of data each. In 2012, the LHC was operated at a center-of-mass energy of 8 TeV and even higher instantaneous luminosities were reached, resulting in a total of $21.8\,\mathrm{fb}^{-1}$ of data collected by the CMS experiment. After the first long shutdown from 2013-2015, the LHC was restarted in 2015 and soon produced proton-proton collisions with a new record center-of-mass energy of 13 TeV. The CMS experiment recorded $3.81\,\mathrm{fb}^{-1}$ of data during this running period.

The currently best description of the most fundamental particles and forces we know of, is given by the Standard Model (SM). Since its introduction, many phenomena and new particles predicted by the SM were later confirmed by experimental observations, the latest being the Higgs boson, of which the discovery was announced on the 4th of July 2012 by the CMS and ATLAS experiments [3]. But despite the huge success of the SM and its very accurate description of nature at low energies, still some questions are left unanswered and indicate, that the SM is still incomplete. Several extensions of the SM have been suggested to overcome these shortcomings. In some of these extensions, an extended Higgs sector would give rise to more physical Higgs mass eigenstates.

In this thesis, a search for a heavy Higgs boson decaying into two light Higgs bosons and further into two bottom quarks and two tau leptons in $2.30\,\mathrm{fb}^{-1}$ of 13 TeV data recorded by the CMS detector in 2015 is presented. The analysis will make heavy use of a kinematic fit, the HHKinFit, developed and tailored specifically for the needs of this analysis. The fit was first used in the analysis of 8 TeV data [1] and was more recently used in an 13 TeV analysis [2]. Since then, further improvements to the HHKinFit have been implemented. The fit makes it possible to precisely determine the mass of a resonantly produced heavy Higgs decaying to two light Higgs and further into tau lepton and b quark pairs. Furthermore, the fit probability of the HHKinFit can be used to separate signal from background events. This feature of the kinematic fit will be used for the first time in the analysis presented in this thesis. No excess in data is observed and exclusion limits will be set. The results will be interpreted in the post-Higgs Minimal Supersymmetric Standard Model (hMSSM) and in the so called non-alignment Two Higgs Doublet Model (2HDM).
To identify b jets, the resolution of the CMS vertex detector is of utmost importance, as it is used to reconstruct the displaced secondary vertices of b-quark decays. In the year-end technical shutdown 2016/2017, the detector will be upgraded to a version that better fits the high instantaneous luminosity environment soon expected at the LHC. An analysis of data collected by an irradiated prototype of the new digital readout chip (ROC) in a positron beam at DESY, will be presented in this thesis.
The contents of this thesis is structured as follows:
First, the SM of particle physics, its short comings, and an example for a possible extension resulting in the manifestation of an additional heavy Higgs boson will be presented in chapter 2.
In Chapter 3, the LHC and the different components of the CMS detector and the trigger components are described, before the Particle Flow (PF) and several other event reconstruction algorithms are introduced.
The beam test study of an irradiated prototype of the new ROC for the phase I pixel detector upgrade is presented in Chapter 4.
Chapter 5 introduces the HHKinFit, a kinematic fitting tool for heavy Higgs decays. Systematic studies on the stability and the resolutions that can be achieved by applying the fit are presented.
The HHKinFit is finally used for an heavy Higgs analysis, searching for heavy Higgs bosons decaying to two light Higgs bosons that further decay to two b quarks and two tau leptons which is discussed and described in detail in Chapter 6. The conclusion and outlook of this thesis is given in Chapter 7.

Chapter 2

Theoretical Background

The Standard Model (SM) [4] of particle physics successfully describes the constituents of matter and their interactions. Nonetheless the model has some theoretical and experimental shortcomings and therefore can not be a fundamental theory. In some potential extension of the SM, a second Higgs doublet is expected, leading to four more Higgs mass eigenstates. One such theory, that would also solve some of the shortcomings of the SM in an elegant way, is Supersymmetry (SUSY). In the following chapter a short introduction of the SM will be given. The general Two Higgs-doublet model and the special case of the two Higgs doublets in the Minimal Supersymmetric Standard Model (MSSM) will be introduced. The outline of this chapter follows in parts [5].

2.1 Standard Model of particle physics

The SM gives a description of all particles and their interactions, excluding the force of gravity. All particles can be classified as either fermions or bosons, where fermions are particles with half integer spin, and bosons are particles with integer spins. All elementary fermions have a spin of $\frac{1}{2}$. They are the fundamental building blocks of matter. Within the SM, spin 1 bosons are the transmitters of the fundamental forces.
Fermions can be divided into two types, quarks and leptons. Leptons can be electrically charged or uncharged and take part in the electromagnetic and weak interaction. Quarks additionally take part in strong interactions. Fermions can further be divided into three families, where each family consists of a charged lepton, a neutral lepton (neutrino), an up-type and a down-type quark. The masses of the particles are free parameters of the theory, that have been determined experimentally since the discovery of the electron in 1897. While neutrinos have no mass in the initial formulation of the SM, it has been shown experimentally that they must posses at least some mass as neutrino oscillations have been observed. The masses of the particles range from very small masses of at most a few eV for neutrinos up to masses of $\approx 173\,\mathrm{GeV}$ for the top-quark.
The interactions between particles can be derived theoretically by the principle of local

gauge invariance. In theories with a local gauge invariance, the Lagrangian of the theory does not change under local (i.e. position dependent) gauge transformations. This is achieved by introducing gauge fields to the theory that compensate for any changes in the Lagrangian that would be introduced by the application of a certain group of local symmetry operations. The SM is based on the symmetry group of unitary gauge transformations given by

$$G_{SM} = SU(3)_C \otimes SU(2)_L \otimes U(1)_Y. \tag{2.1}$$

Herein, $SU(3)_C$ denotes the group of the strong interaction formalized by quantum chromodynamics (QCD). The electroweak-isospin group $SU(2)_L$ and the hypercharge group $U(1)_Y$ are combined to form the electroweak interaction group $SU(2)_L \otimes U(1)_Y$. The force carriers of the strong interaction are called gluons, the charge associated with $SU(3)_C$ is called color. For reasons of renormalizability three color degrees of freedom are needed. They are named after the three colors that composite human sight: red, green and blue. While quarks/antiquarks carry a single color/anticolor charge, gluons carry a color and anticolor charge combination. This would allow for nine different color-anticolor combinations, but as no strong interaction between colorless bound quark states are observed, the one possible colorless singlet states is of no relevance. This leaves eight different linear independent gluon representations.
As gluons are colored themselves, they also couple to each other. This leads to the effect, that the energy stored in the gluonic field between two strongly interacting quarks increases as the distance between them increases. As soon as the energy stored in the field becomes big enough, it is energetically preferred to create a new quark-antiquark pair between the two quarks. Due to this effect, quarks can never be observed alone, but only in color-neutral groups (hadrons). Hadrons consist of a quark and an antiquark (meson) or of three quarks (baryon). The gluon-gluon interaction is also responsible for the short reach of the strong force of $\mathcal{O}(1\,\mathrm{fm})$.
In the electroweak theory, the observed force carriers Z^0, $W^{\pm}$ and the photon of the weak and electromagnetic interactions are a result of the mixture of the gauge fields of $SU(2)_L$ and $U(1)_Y$. This combination is known as the "Glashow-Salam-Weinberg" theory. The gauge fields associated with $SU(2)_L$ are W^1_μ, W^2_μ and W^3_μ. The field of $U(1)_Y$ is denoted as B_μ. It is associated with the hypercharge Y, which relates to the electric charge Q and Isospin I_3 by:

$$Q = I_3 + \frac{Y}{2} \tag{2.2}$$

The W_μ^1 and W_μ^2 fields have a weak isospin of $I_3 = \pm 1$. They mix and the eigenstates associated with the $W^\pm$ mass eigenvalues can be given by:

$$W_\mu^\pm = \frac{1}{\sqrt{2}}(W_\mu^1 \pm iW_\mu^2) \tag{2.3}$$

Similarly, the W_μ^3 and B_μ fields mix to give rise to the Z^μ and the A^μ field, associated with the Z^0-boson and the photon respectively

$$\begin{pmatrix} A^\mu \\ Z^\mu \end{pmatrix} = \begin{pmatrix} \cos\theta_W & \sin\theta_W \\ -\sin\theta_W & \cos\theta_W \end{pmatrix} \begin{pmatrix} B_\mu \\ W_\mu^3 \end{pmatrix}. \tag{2.4}$$

Herein, θ_W is the Weinberg angle defined as the ratio of the $SU(2)_L$ and $U(1)_Y$ couplings. Experiments have measured θ_W to be $\theta_W = 0.23126(5)$ [6]. Fermions with the exception of the neutrino can exist in left-handed or right-handed states as they have non-integer spin. As the neutrino is assumed to be massless in the SM, it can only exist in the left-handed state. As the right-handed states have no weak isospin, the $W^\pm$-bosons only couple to left-handed states. The Z^0 boson and photon also couple to right-handed states. Photons only couple to charged particles.
In Fig. 2.1, the six quarks, six leptons and four gauge bosons are listed with some of their quantum numbers.

As experimental observations have shown that gauge bosons of the weak interaction have mass and introducing mass terms for bosons or fermions by hand would destroy the local gauge invariance of the theory, masses must instead be introduced dynamically. This is achieved by the Higgs mechanism. The Higgs mechanism leaves the Lagrangian but not the vacuum state unchanged under electroweak-symmetry operations. This is known as spontaneous symmetry breaking. The Higgs field is a scalar self-interacting field with a ground state realized at a non-zero value of the field strength. Particle masses can then be reinterpreted as the particle interacting with the omni-present ground state of the field.
The Higgs field is represented by a doublet with a charged and a neutral complex component

$$\Phi = \begin{pmatrix} \Phi^+ \\ \Phi^0 \end{pmatrix}. \tag{2.5}$$

The most general non trivial renormalizable potential, invariant under $SU(2)_L$ is given by:

$$V(\Phi) = \mu^2|\Phi|^2 + \lambda|\Phi|^4. \tag{2.6}$$

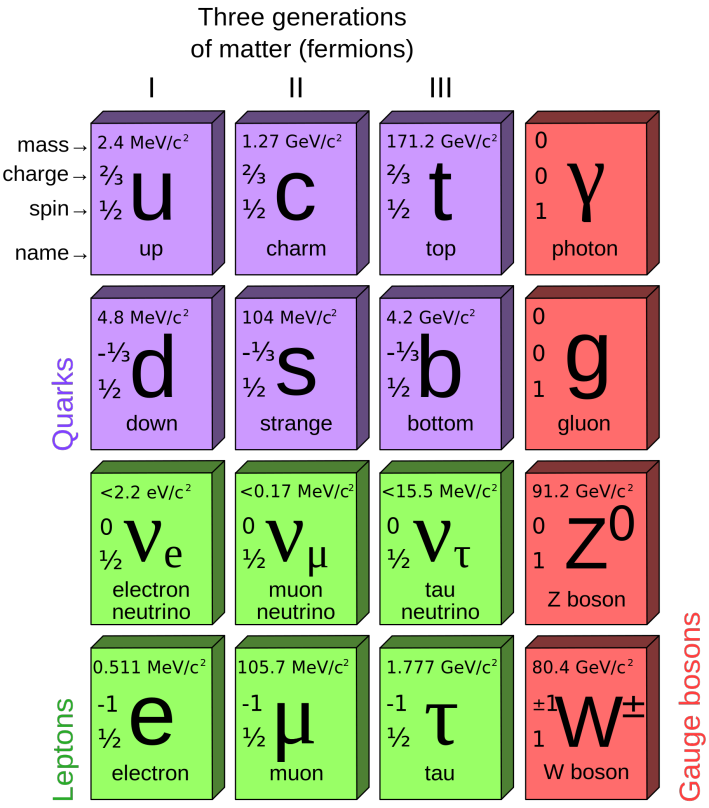

Figure 2.1: The fermions and bosons included in the SM excluding the Higgs [7].

For combinations of a negative values of μ^2 and a positive value of λ the potential has an infinite number of minima with non-zero vacuum expectation value of

$$v = \sqrt{\frac{-\mu^2}{2\lambda}}. \tag{2.7}$$

By considering perturbations around an arbitrarily chosen electrically neutral vacuum state given by

$$\Phi = \frac{1}{\sqrt{2}} \begin{pmatrix} 0 \\ v \end{pmatrix}, \tag{2.8}$$

one can obtain the Higgs field with the massive Higgs boson h. According to Goldstone's theorem, three massless Goldstone bosons would be introduced by breaking the symmetry spontaneously. However, as shown by Brout, Englert [8] and Higgs [9, 10], under a suitable choice of gauge, these additional degrees of freedom are absorbed by the longitudinal components of the $W^{\pm}$ and Z bosons, giving them their masses and resulting in a Higgs field given by:

$$\Phi = \frac{1}{\sqrt{2}} \begin{pmatrix} 0 \\ v + h \end{pmatrix}. \tag{2.9}$$

The quantum excitation of one of the neutral Higgs field components at the ground state can be detected as a scalar particle: the Higgs boson. The mass terms of the $W^{\pm}$, Z and h boson are given by:

$$m_W = \frac{1}{2} g v \tag{2.10}$$

$$m_Z = \frac{m_W}{\cos\theta_W} \tag{2.11}$$

$$m_h = \sqrt{-2\mu^2} \tag{2.12}$$

The fermions become massive as they interact with the Higgs ground state via the Yukawa coupling. Their mass is given by

$$m_f = \lambda_f \frac{v}{\sqrt{2}}, \tag{2.13}$$

where λ_f is a free parameter for each fermion of the theory. The mass of the fermions is proportional to their respective coupling strengths.
On the 4th of July 2012, the CMS and ATLAS experiment announced the discovery of a boson. Its mass has been measured with $m = 125.09 \pm 0.21(\text{stat.}) \pm 0.11(\text{syst.})\,\text{GeV}$ [3]. Within the uncertainties, the properties of this particle, like e.g. the branching ratios, production cross section and spin, are consistent with the properties expected for a Higgs boson.

2.2 Shortcomings of the SM

Although the SM was successfully used to make many predictions that could later be confirmed with high accuracy, some questions remain which can not be answered by the SM. This means that the SM can only be seen as a low energy limit of a more fundamental theory. In the following, the shortcomings of the SM will be described and Supersymmetry (SUSY), a possible extension that can solve a lot of these shortcomings, will be introduced.
Gravity is not included in the SM. This means that at the latest, the SM will fail to properly describe nature at the Planck scale ($\approx 10^{19}$ GeV), where gravity cannot be neglected anymore. A more advanced theory which is similar to the SM for small energies, could be a solution to this problem.
Furthermore, SUSY can lead to the unification of coupling constants at high energies (GUT scale at $\approx 10^{16}\,\text{GeV}$). The running of the coupling constants for the SM and for a SM with a minimal supersymmetric extension (MSSM), are shown in Fig. 2.2. As the coupling constants do not converge in the SM, it can not be the sole low energy phenomenon of a grand unified theory (GUT). There is no really compelling argument why their has to be a unification of the forces. But as it would be very elegant and

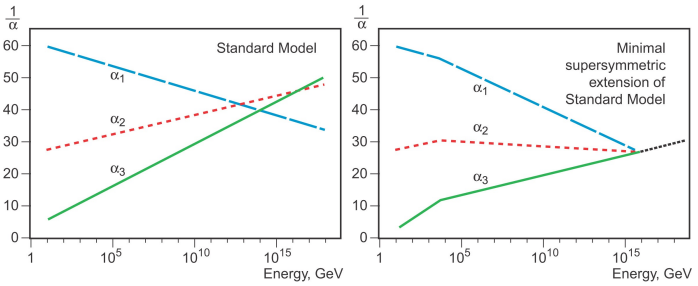

Figure 2.2: Running of the coupling constants with increasing energy for the SM (left) and within the minimal supersymmetric model (right) [11].

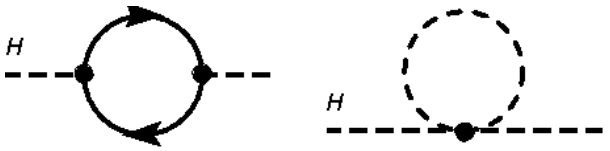

Figure 2.3: Corrections of the Higgs mass by fermion loops (left) can in part be compensated by the scalar superpartners (right) [12].

simple and in the past, following elegant and simple ideas was often very fruitful, the possibility of the unification of the forces in SUSY models is a good indicator that SUSY might be realized in nature.

Within the SM, the Higgs mass is influenced by fermion loops (see Fig. 2.3). The Higgs mass is the sum of the bare Higgs mass $m_{H,\text{bare}}$ and the corrections resulting from fermion loops Δm_H^2

$$m_H^2 = m_{H,\text{bare}}^2 + \Delta m_H^2. \tag{2.14}$$

A fermion which couples to the Higgs field with a coupling constant of λ_F, contributes to the fermion loop correction with the following term:

$$\Delta m_H^2 = -\frac{\|\lambda_F\|^2}{8\pi^2}\Lambda_{UV}^2, \tag{2.15}$$

where Λ_{UV}^2 is the cut-off value at the validity limit of the SM. If Λ_{UV}^2 would be at the Planck scale, the Higgs mass would be bigger than the estimated Higgs mass ($m_H^2 = (100\,\text{GeV})^2$) by a factor of $\approx 10^{30}$. For the Higgs mass to be roughly at the estimated value, $m_{H,\text{bare}}^2$ would have to be tuned relative to the value of Λ_{UV}^2. This problem is known as the fine tuning or the hierarchy problem. SUSY would solve this problem very elegantly through the introduction of additional particles, which add corrections to the Higgs mass that counteract the corrections of the SM fermions in Eq. 2.15 in such a way, that only a logarithmic dependence on Λ_{UV}^2 remains.

Another shortcoming of the SM is that it contains no viable candidate for a dark matter particle. Only about 4% of the universe consist of the matter we know [13]. Around 73% consist of dark energy. The remaining 23% consist of dark matter. As dark matter does not interact through strong or electromagnetic interactions, and as the weak interaction

is negligible over long distances only the dark matter interaction by gravity has been observed. The only SM particle, which could be a viable dark matter candidate is the neutrino, as neutrinos only interact weakly and, although not explained by the SM, have been experimentally found to have mass. But as we know from structure formations of the universe, that dark matter consists of slow moving particles and as neutrino move with speeds close to the speed of light due to their very small mass, neutrinos can be ruled out as the major constituent of dark matter. SUSY models could provide a lightest supersymmetric particle (LSP) which does not decay and only interacts weakly. This LSP could make up most of the dark matter in the universe [14].

2.3 Supersymmetry

In SUSY theories, for every boson a new supersymmetric fermion and for every fermion a new supersymmetric boson is introduced [15]. The SM particle and its supersymmetric partner are identical in every quantum number except spin. The spin of the supersymmetric particle S_n is derived from the spin of the SM particle S_m by subtracting $\frac{1}{2}$, the exception being Higgs particles for which $\frac{1}{2}$ is added to the spin of the SM particle. This can be expressed by introducing an anticommutative spinor Q

$$Q|fermion\rangle = |boson\rangle \qquad Q|boson\rangle = |fermion\rangle. \tag{2.16}$$

Every theory that is invariant under Q is a SUSY theory. The superpartners of the leptons l are called sleptons $\tilde{l}$. Squarks $\tilde{q}$ are the partners of the quarks q. Gauginos $\tilde{g}$ are the partners of the gauge bosons. Left and right-handed fermions have different superpartners. A selectron that is the superpartner of a left-handed electron is denoted with $\tilde{e}_L$, despite it not having chirality due to its spin of 0.
As no SUSY particles have been discovered yet, the mass of the supersymmetric particles must be greater than the mass of their SM partners. This means SUSY has to be a broken symmetry. For SUSY to still be a solution to the fine tuning problem explained in Sec. 2.2, the mass of the SUSY particles should be around $\approx 1\,\text{TeV}$ so that the correction terms to the Higgs mass from SM and from SUSY particles cancel each other out.
In many SUSY models R-parity is introduced as a new multiplicative conserved quantum number

$$R = (-1)^{2S+3(B-L)}. \tag{2.17}$$

S denotes the Spin. B and L denote the baryon and lepton number. R-parity is 1 for all SM particles and -1 for all SUSY particles. There are several consequences arising from R-parity conservation. As long as R-parity is conserved, SUSY particles can only be produced in pairs. Furthermore, R-parity conservation leads to a stable, lightest

supersymmetric particle (LSP) at the end of each decay chain. If the LSP does not take part in the electromagnetic and strong interaction, it is therefore a possible dark matter candidate.
As we do not know how the mechanism that breaks the symmetry works, we have to explicitly introduce all possible SUSY breaking terms, which leads to at least 105 free parameters in addition to the 19 free parameters of the SM to describe a minimal supersymmetric model. If a specific SUSY breaking mechanism is assumed, the number of free parameters can be reduced.

2.3.1 Higgs Sector in the MSSM

In SUSY theories, a second Higgs doublet is needed firstly, to avoid a gauge anomaly in the electroweak gauge symmetry, which would render it inconsistent as a quantum theory and secondly because, due to the structure of supersymmetric theories, only $Y = \frac{1}{2}$ Higgs doublets can couple to up-type quarks to give them their mass while only a $Y = -\frac{1}{2}$ doublet can give masses to down-type quarks and charged leptons. The vacuum expectation values of the two Higgs-doublet fields $\Phi_u = (\Phi_u^+, \Phi_u^0)$ and $\Phi_d = (\Phi_d^-, \Phi_d^0)$ are given by

$$\langle \Phi_u \rangle = \frac{1}{\sqrt{2}} \begin{pmatrix} 0 \\ v_u \end{pmatrix} \tag{2.18}$$

$$\langle \Phi_d \rangle = \frac{1}{\sqrt{2}} \begin{pmatrix} v_d \\ 0 \end{pmatrix} \tag{2.19}$$

where the normalization has been chosen such that $v^2 = v_d^2 + v_u^2 = 4\frac{m_W^2}{g^2}$ [16]. From the eight degrees of freedom of the two complex doublets, three determine the mass of the $W^\pm$ and Z^0 bosons. The remaining five degrees lead to five physical Higgs particles. Two CP-even scalars h and H, where H denotes the heavier of the two, one CP-odd scalar A and two charged Higgs bosons $H^\pm$. Due to constraints on the Higgs sector imposed by the supersymmetric structure, at tree level all Higgs sector parameters are determined by two free parameters. The ratio of the vacuum expectation values

$$\tan\beta = \frac{v_u}{v_d}, \tag{2.20}$$

and one of the Higgs masses, conventionally chosen to be the mass of the pseudoscalar Higgs m_A. The tree level mass of the lightest Higgs state is constraint to be lighter than the Z boson $m_h < m_Z$, however it has been shown, that higher order radiative corrections are of extreme importance [17]. The dominant contribution to these corrections can be attributed to the incomplete cancellation of the top and stop loops. The stop mass is dependent on the Higgs mass parameter μ and the SUSY breaking mechanism,

which means that the electroweak symmetry breaking scale is tightly coupled to the scale of SUSY M_S, where M_S is defined as the geometric average of the two stop masses $M_S = \sqrt{m_{\tilde{t}_1} m_{\tilde{t}_2}}$.
Most searches for direct manifestation of the heavier H, $H^{\pm}$ and A states by ATLAS and CMS have been concentrating on a region of large $\tan\beta \gtrsim 5 - 10$. The reason for this is that for an acceptable amount of fine-tuning the SUSY-scale should be of the order of $M_S \approx 1\,\text{TeV}$ but for $\tan\beta \lesssim 3 - 5$ and $M_S \lesssim 3\,\text{TeV}$ the observed value of $m_h = 125\,\text{GeV}$ is excluded [18].

2.3.2 Heavy Higgs Phenomenology in the low $\tan\beta$ region

As recently shown in [19], by relaxing the requirement on M_S, the region of low $\tan\beta$ can be reopened for heavy Higgs searches. Scenarios that feature a high SUSY-scale of $M_S = 10$ - $100\,\text{TeV}$, like split-SUSY [20] and high-scale SUSY [21] have been considered in the past. In these theories, all scalar particles, except for the SM-like Higgs boson, have very high masses and the solution to the hierarchy problem usually given by SUSY models is abandoned. As these models would put the extended Higgs sector out of reach of the LHC, they are of less interest for this thesis.
Another possibility is to assume that only the sfermions are very heavy. This can be the case in scenarios where the soft SUSY-breaking scalar mass terms are different for sfermions and for the two Higgs doublets. These models with decoupled m_A and M_S are called non-universal Higgs mass models [22]. Models with large values for M_S and low values for m_A have been discussed [23].
In Fig. 2.4 the contours of allowed values in the $\tan\beta$-M_S parameter space are shown. For the measured Higgs mass value of approximately $m_h = 125\,\text{GeV}$, and an assumed scale of M_S close to 1 TeV, $\tan\beta$-values below 5 can be ruled out. However, by inceasing the value of M_S by one or two orders of magnitude, $\tan\beta$-values close to 1 can be reached.

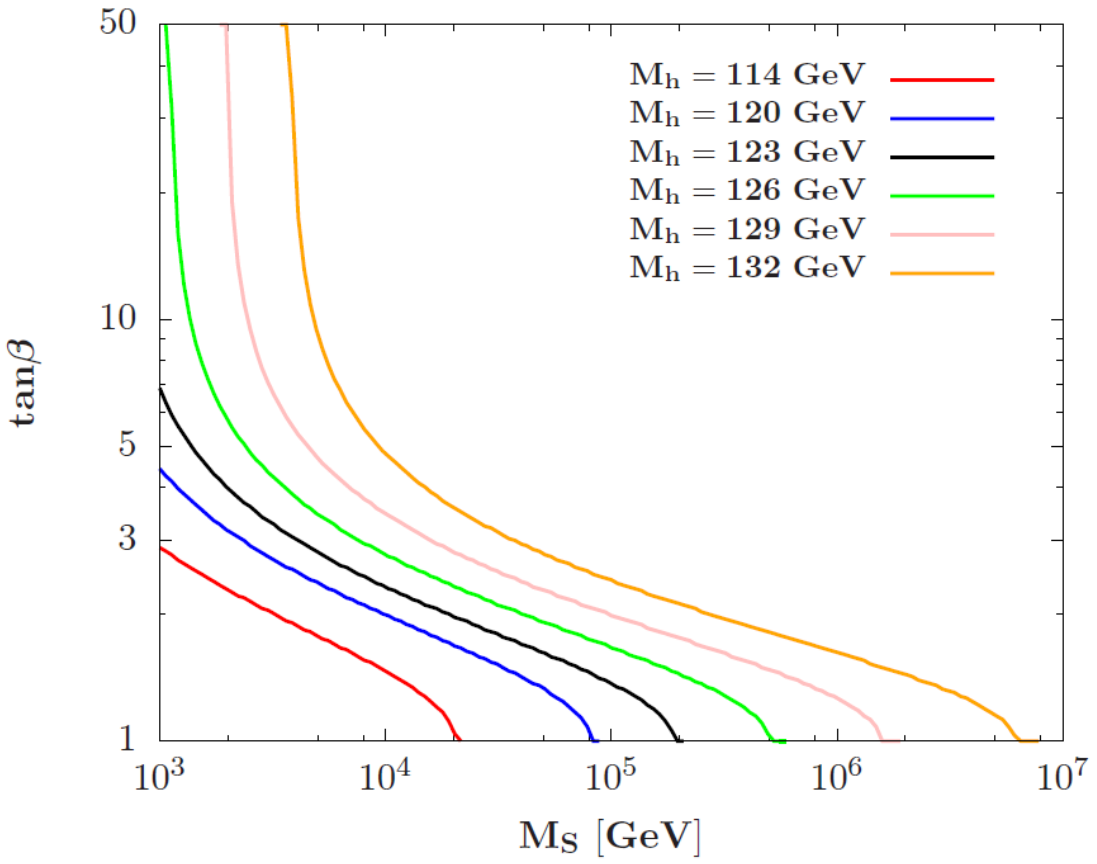

Figure 2.4: Contours of allowed values in the $\tan\beta$-M_S parameter space for fixed values of M_h between 114 and 132 GeV [19].

2.4 Heavy Higgs decays

The thesis presented in Chapter 6 searches for a heavy Higgs boson decaying to two light Higgs decaying to two b quarks and two tau leptons. A Feynman diagram of the process is shown in Fig. 2.5. The branching ratio for a heavy Higgs to decay to two light Higgs is strongly dependent on the mass of the heavy Higgs boson and the Higgs coupling parameters of the underlying theory. In the following, two possible models in which the findings of the analysis in Chapter 6 will be interpreted are introduced.

2.4.1 hMSSM

Recent results of heavy Higgs searches where the heavy Higgs decays into two light Higgs bosons have been interpreted in the so called hMSSM [24–26], which is based on the MSSM and includes the constraints given by the Higgs boson discovered at the LHC. The model was proposed as a benchmark for the low $\tan\beta$ region by the LHC cross-section working group in [27]. The hMSSM is based on the three assumptions that the Higgs boson with a mass of 125 GeV observed at the LHC is the lightest Higgs boson, that radiative corrections to the masses of the CP-even neutral states is dominated by

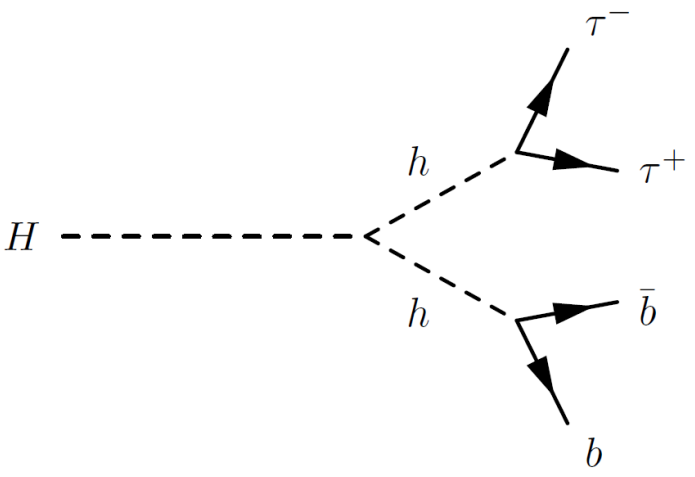

Figure 2.5: Feynman diagram of the decay of a heavy Higgs boson H to two light Higgs bosons h further decaying to two tau leptons and two b quarks.

contributions from the top and stop loops and that all SUSY particles are too heavy to influence the phenomenology at the LHC, expect for the radiative correction of the stop loops to the mass terms. In this model the masses of H, $H^{\pm}$ and A become approximately mass degenerate.

Since the hMSSM was proposed as a benchmark scenario the findings of many searches, performed during the 8 TeV running period at CMS, looking for signs of BSM Higgs bosons were combined and interpreted within the hMSSM [28]. Fig. 2.6 shows several 95% CL exclusion limits in the m_A-tan β plane of the hMSSM [28]. The exclusion limit for the H→hh→bb̄$\tau\tau$ search combined with an A→ZH search carried out at 8 TeV [1] is shown in red. It excludes approximately the region of $\tan\beta < 2.5$ between 210 GeV$<$ $m_A < 350$ GeV. In Fig. 2.7 the product of cross section and branching ratio (σ·BR) at a center-of-mass energy of $\sqrt{s} = 13$ TeV for the decay H→hh→bb̄$\tau\tau$ is shown. The cross sections and branching ratios provided by the LHC cross-section working group [29] were calculated using HDECAY [30, 31]. As can be seen, the σ·BR falls of steeply for values of $m_A > 2m_t$ as the decay H→tt̄ opens up, and quickly becomes the dominant decay channel. Since the results of the 8 TeV analyis, to which I contributed by providing the kinematic fitting tool, were published, the sensitivity of the analysis is severely limited by the low σ·BR for values of $m_A > 2m_t$. Considering this limited reach and the fact that values of $m_A < 300$ GeV are already disfavored by indirect bounds through Higgs coupling measurements (pink area in Fig. 2.6), the area of parameter space in reach for an H→hh→bb̄$\tau\tau$ search not already excluded becomes quite small. For this reason, looking for a less constrained alternative scenario, a more general model featuring a heavy Higgs decaying to two light Higgs is introduced in the next section.

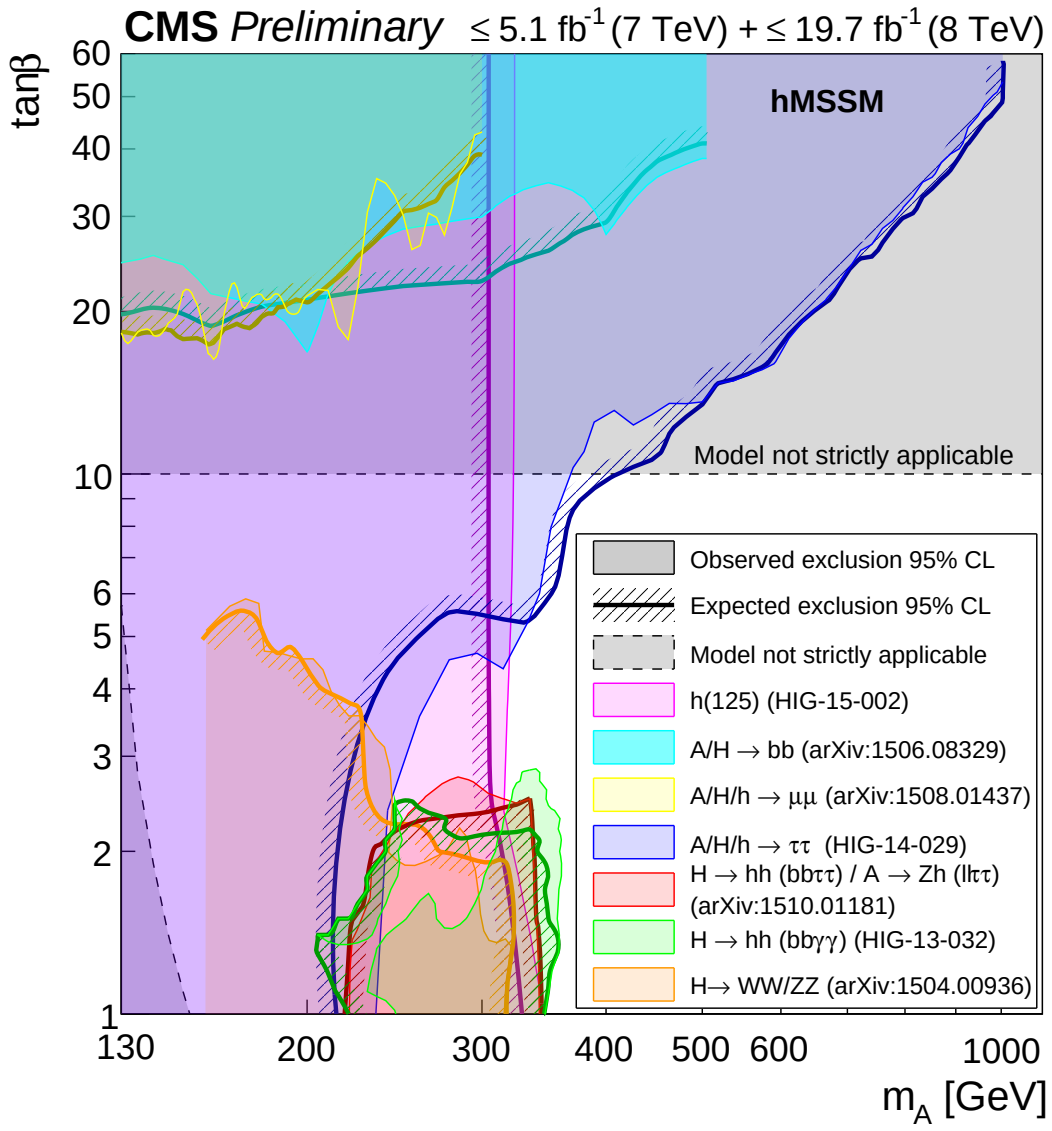

Figure 2.6: 95% CL exclusion contours of several BSM Higgs searches in the hMSSM m_A-tan β parameter space [28].

2.4.2 Two Higgs Doublet Models

Two Higgs Doublet Models (2HDMs) [32] are models in which the scalar sector consists of two complex SU(2) doublets ϕ_1 and ϕ_2 which feature a hypercharge of one. 2HDMs are well motivated, as a multitude of BSM models feature two Higgs doublets. Two example of BSM models featuring two Higgs doublets are SUSY, as introduced in Section 2.3.1 and axion models [33]. Another motivation for 2HDMs is that due to the flexibility of the scalar mass spectrum [34] and due to additional sources of CP violation, 2HDMs might be able to generate the baryon asymmetry observed in the universe.

The most general scalar potential of the two fields ϕ_1 and ϕ_2 when assuming that CP is conserved in the Higgs sector, that CP is not spontaneously broken and that all quartic terms, which are odd in either of the doublets, are eliminated due to discrete symmetries,

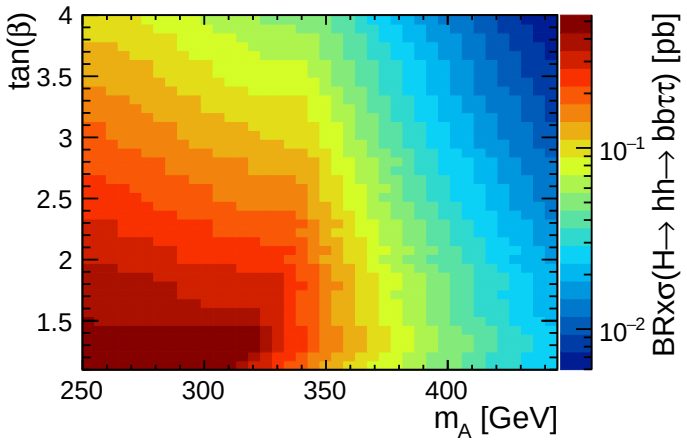

Figure 2.7: σ·branching ratio (BR) at a center-of-mass energy of $\sqrt{s} = 13\,\text{TeV}$ for the decay H→hh→b$\bar{\text{b}}\tau\tau$. The cross sections and branching ratios provided were calculated by the LHC cross-section working group [29] using HDECAY [30, 31].

can be written as:

$$\begin{aligned} V =& m_{11}^2\phi_1^\dagger\phi_1 + m_{22}^2\phi_2^\dagger\phi_2 - m_{12}^2\left(\phi_1^\dagger\phi_2 + \phi_2^\dagger\phi_1\right) + \frac{\lambda_1}{2}\left(\phi_1^\dagger\phi_1\right)^2 + \frac{\lambda_2}{2}\left(\phi_2^\dagger\phi_2\right)^2 \\ &+ \lambda_3\phi_1^\dagger\phi_1\phi_2^\dagger\phi_2 + \lambda_4\phi_1^\dagger\phi_2\phi_2^\dagger\phi_1 + \frac{\lambda_5}{2}\left[\left(\phi_1^\dagger\phi_2\right)^2 + \left(\phi_2^\dagger\phi_1\right)^2\right], \end{aligned} \tag{2.21}$$

where all parameters m_{ij} and λ_k are real.

Just as described in Section 2.3.1, the four additional degrees of freedom introduced by a second doublet lead to a total of five physical Higgs bosons: h,H,A and the two charged Higgs bosons $H^\pm$.

In general, 2HDMs feature flavor changing neutral currents (FCNCs), as the two Yukawa matrices, which are 3 by 3 matrices containing the coupling strengths of the two Higgs fields to the three fermion generations, might not be simultaneously diagonalizable. As FCNCs have not been observed in nature, further constraints must be introduced to 2HDMs to suppress tree-level FCNCs. As has been shown by Glashow, Weinberg and Paschos [35, 36], these constraints can be fulfilled, by requiring that all right-handed quarks of a given charge must couple to a single Higgs doublet. This leaves two possibilities: Either all right handed quarks couple to the same Higgs doublet (type I) or all right-handed up-type quarks couple to one of the Higgs doublets, while the right-handed down-type quarks couple to the other doublet (type II). Supersymmetric models feature a Higgs sector of type II. In the following a special case of a 2HDM of type I, in which the findings of the analysis presented in Chapter 6 will be interpreted, will be introduced.

The non-alignment 2HDM was first introduced in [37]. The model is described in the hybrid basis by the parameters m_h, m_H, $\cos(\beta-\alpha)$, $\tan\beta$, Z_4, Z_5 and Z_7. α denotes the mixing angle of the two neutral CP-even Higgs states. $\cos(\beta-\alpha)$ determines the coupling strength of the CP-even Higgs bosons to the W$^\pm$ and Z boson. The coupling

strengths are given by:

$$g_{hVV} = g_{h_{SM}VV} \sin(\beta - \alpha), \quad g_{HVV} = g_{h_{SM}VV} \cos(\beta - \alpha), \tag{2.22}$$

where $g_{h_{SM}VV}$ is the coupling strength to the vector bosons for an SM Higgs boson. $\tan\beta$ is the ratio of the vacuum expectation value of the two fields ϕ_1 and ϕ_2

$$\langle \phi_i^0 \rangle = \frac{v_i}{\sqrt{2}} e^{i\epsilon_i}, \quad \text{with } i = 1, 2, \tag{2.23}$$

where ϵ_i denotes a phase parameter and v_1 and v_2 are real and non-negative.
Z_4, Z_5 and Z_7 are the quartic couplings of the fields in the Higgs-basis defined by rotating ϕ_1 and ϕ_2:

$$H_1 = \begin{pmatrix} H_1^+ \\ H_1^0 \end{pmatrix} \equiv \frac{v_1 e^{-i\epsilon_1}\phi_1 + v_2 e^{-i\epsilon_2}\phi_2}{v}, \quad H_2 = \begin{pmatrix} H_2^+ \\ H_2^0 \end{pmatrix} \equiv \frac{-v_2 e^{i\epsilon_2}\phi_1 + v_1 e^{i\epsilon_2}\phi_2}{v}, \tag{2.24}$$

with $v^2 = v_1^2 + v_2^2$. Due to its relation to the Fermi constant and the W boson mass, the value of v^2 is fixed to $v^2 = \frac{1}{\sqrt{2}G_F} = 4\frac{m_W^2}{g^2}$. In this basis the scalar potential takes the form:

$$\begin{aligned} V =& Y_1 H_1^\dagger H_1 + Y_2 H_2^\dagger H_2 + \left[Y_3 H_1^\dagger H_2 + h.c. \right] + \frac{1}{2} Z_1 \left(H_1^\dagger H_1 \right)^2 \\ &+ \frac{1}{2} Z_2 \left(H_2^\dagger H_2 \right)^2 + Z_3 \left(H_1^\dagger H_1 \right) \left(H_2^\dagger H_2 \right) + Z_4 \left(H_1^\dagger H_2 \right) \left(H_2^\dagger H_1 \right) \\ &+ \left\{ \frac{1}{2} Z_5 \left(H_1^\dagger H_2 \right)^2 + \left[Z_6 \left(H_1^\dagger H_1 \right) + Z_7 \left(H_2^\dagger H_2 \right) \right] H_1^\dagger H_2 + h.c. \right\}, \end{aligned} \tag{2.25}$$

with all parameters $Y_1 ... Y_3, Z_1 ... Z_7$ being real, under the right choice of basis.
In the non-alignment scenario, the Higgs boson detected at the LHC is identified with the light Higgs boson, fixing m_h to 125 GeV. In order to obtain a mass hierarchy of

$$m_h = 125\,\text{GeV} < m_H < m_A = m_{H^\pm}, \tag{2.26}$$

Z_4 and Z_5 are set to $Z_4, Z_5 = -2$. Z_7 is set to zero. m_H and $\tan\beta$ will be kept as free parameters.
$\cos(\beta - \alpha)$ is constrained by measurements of the Higgs coupling strength to vector bosons. The current constraints on $\cos(\beta - \alpha)$ for a type I 2HDM with a mass of $m_H = 300\,\text{GeV}$ (left) and $m_H = 600\,\text{GeV}$ (right) are shown in Fig. 2.8. The colored areas show the compatibility with the current Higgs coupling measurements at 1σ (green), 2σ (yellow) and 3σ (blue). A value of $\cos(\beta - \alpha) = 0$ would result in SM-like couplings of the light Higgs boson.
For the non-alignment scenario suggested in [37], $\cos(\beta - \alpha)$ is fixed close to the allowed 1σ limit at $\cos(\beta - \alpha) = 0.1$ to create an interesting phenomenology for the heavy

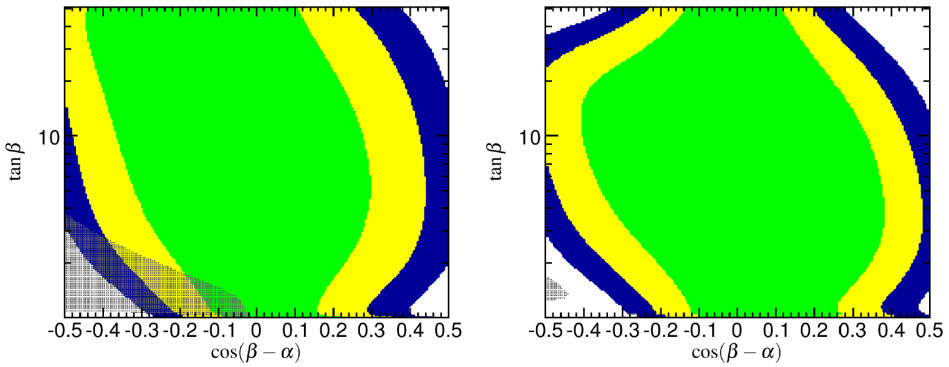

Figure 2.8: Constraints on $\cos(\beta-\alpha)$ for a type I 2HDM with a mass of $m_H = 300\,\text{GeV}$ (left) and $m_H = 600\,\text{GeV}$ (right) by measurements of th Higgs coupling strength. The colored areas show the compatibility with the current Higgs coupling measurements at 1σ (green), 2σ (yellow) and 3σ (blue) [37].

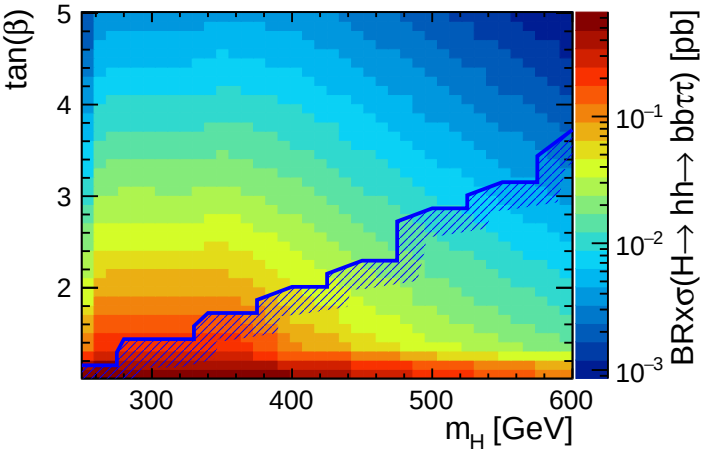

Figure 2.9: σ·BR at a center-of-mass energy of $\sqrt{s} = 13\,\text{TeV}$ for the process H→hh→bb̄$\tau\tau$ in the non-alignment 2HDM at $\cos(\beta-\alpha) = 0.1$ The area enclosed below the blue line is excluded due to stability constraints of the Higgs potential at the input scale. The cross sections and BRs have been calculated using SusHi and 2HDMC [38–46].

Higgs boson. The σ·BR at a center-of-mass energy of $\sqrt{s} = 13\,\text{TeV}$ for the process H→hh→bb̄$\tau\tau$ for this scenario is shown in Fig. 2.9. The area enclosed below the blue line is excluded due to stability constraints of the Higgs potential at the input scale. The cross sections and BRs have been calculated using SusHi and 2HDMC [38–46]. The σ·BR in this scenario stays relatively high at points of low $\tan\beta$, even for high masses of $m_H > 2m_t$. Unfortunately, the most appealing areas within this phase space are already excluded due to stability constraints of the Higgs potential. Fig. 2.10 shows the σ·BR at a center-of-mass energy of $\sqrt{s} = 13\,\text{TeV}$ for the process H→hh→bb̄$\tau\tau$ for the non-alignment scenario where the value for $\cos(\beta-\alpha)$ has been set to 0.05 (left) and 0.02 (right). For these cases the area excluded by stability constraints becomes much smaller, but at the same time the branching ratio for H→hh becomes much smaller as

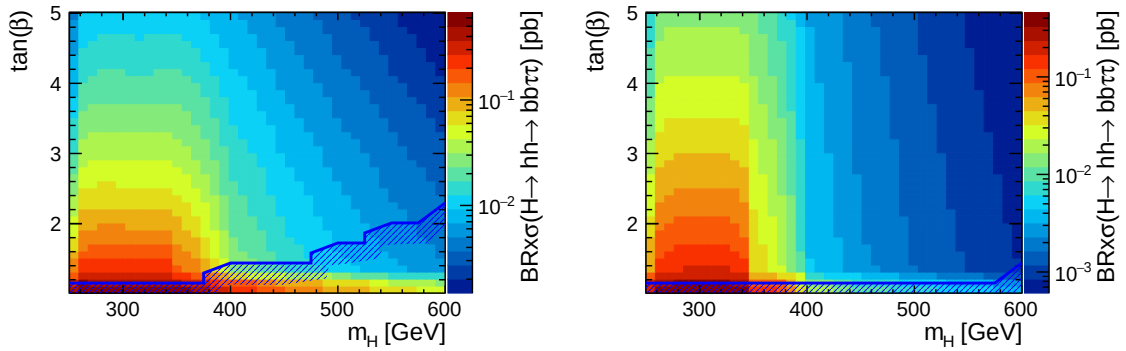

Figure 2.10: σ·BR at a center-of-mass energy of $\sqrt{s} = 13\,\text{TeV}$ for the process H→hh→b$\bar{\text{b}}\tau\tau$ for the non-alignment scenario where the value for $\cos(\beta - \alpha)$ has been set to 0.05 (left) and 0.02 (right). The cross sections and BRs have been calculated using SusHi and 2HDMC [38–46].

the coupling of the heavy Higgs to fermions is stronger compared to the non-alignment model at $\cos(\beta - \alpha) = 0.1$ and as the decay H→t$\bar{\text{t}}$ becomes kinematically allowed.

In all models presented in this chapter, the potential of the H→hh→b$\bar{\text{b}}\tau\tau$ search after 8 TeV data is constrained. The search presented in Chapter 6 will be interpreted in the hMSSM and the non-alignment 2HDM for $\cos(\beta - \alpha)$ values of 0.02 and 0.05. Additionally a model independent limit on the σ·BR will be given.

Chapter 3

The LHC and CMS-Detector

3.1 Large Hadron Collider

The Large Hadron Collider (LHC) [47] is a circular proton-proton collider operated by the European organization for nuclear research (CERN) near Geneva[1]. It is located in the tunnel formerly used by the Large Electron-Positron Collider (LEP). The LHC was designed to allow for proton collisions with a center-of-mass energy of up to 14 TeV at an instantaneous luminosity of $\mathcal{L} = 10^{34}\,\mathrm{cm}^{-2}\mathrm{s}^{-1}$. The LHC is also used to accelerate heavy Ions, like lead nuclei, which can then collide with a center-of-mass energy of up to 5.5 TeV per colliding nucleon pair. The instantaneous luminosity that can be reached with lead nuclei is $\mathcal{L} = 10^{27}\,\mathrm{cm}^{-2}\mathrm{s}^{-1}$.

The number of events per second N is given by $N = \mathcal{L}\sigma$, where σ is the cross section of the process. The Luminosity at the LHC is given by:

$$\mathcal{L} = \frac{N_b^2 n_b f_{rev} \gamma}{4\pi\epsilon_n \beta^*} F \tag{3.1}$$

The formula symbols used in this equation are:

- N_b: Number of particles per bunch.
- n_b: Number of bunches per beam.
- f_{rev}: Revolution frequency.
- γ: Lorentz factor.
- F: Reduction factor due to the crossing angle.
- ϵ_n: Normalized, transverse emittance of the beam. This is a measurement of the parallelism of the beam.

[1] In parts, the following chapter follows the "The LHC and CMS-Detector" chapter of my master thesis [5].

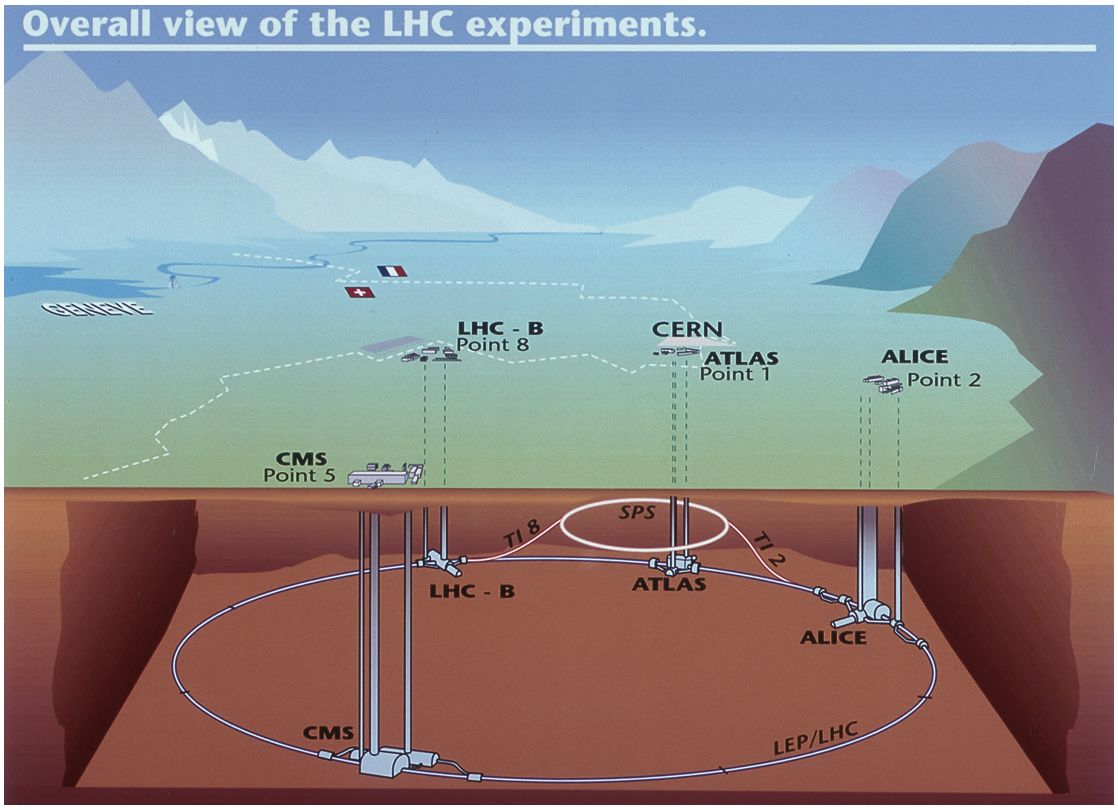

Figure 3.1: Schematic overview of the LHC and it's four main experiments [48].

- β^*: Beam size at the interaction point.

The width of the beam is defined by ϵ_n and β^*. To achieve the design luminosity of $\mathcal{L} = 10^{34} cm^{-2} s^{-1}$, 2808 bunches have to collide every 25 ns, while beam parameters are $\epsilon_n = 3.75\,\mu$m and $\beta^* = 0.55$ m. Very strong magnetic fields of about 3.4 Tesla are needed to force the 7 TeV protons onto their circular track. To reach magnetic fields of this strength, superconducting magnets cooled to 1.9° K by liquid helium are used.

The four main experiments at the LHC are ATLAS [49], CMS [50], ALICE [51] and LHCb [52]. While ATLAS and CMS are multi-purpose detectors designed for peak luminosities in proton-proton interactions to look for physics beyond the standard model, detect the Higgs and perform precise measurements of SM parameters, ALICE looks at the collision of lead ions to investigate the resulting quark-gluon plasma and LHCb focuses on the CP-violation and rare decays in b-physics. In Fig 3.1 an overview of the LHC and it's experiments is shown.

In the end of 2009, the first data was taken at the LHC with a center-of-mass energy of 900 GeV, which was then scaled up to 2360 GeV until the end of the year. The collisions achieved in that time period were the particle collisions with the highest center-of-mass energy ever created by mankind. In the years 2010 and 2011 5.2 fb^{-1} of 7 TeV data have been recorded by the CMS detector. In 2012, while the LHC was operated at a center-of-mass energy of 8 TeV, CMS recorded 21.8 fb^{-1} of data, before going into the first of

three planned long shutdowns. During this period, the LHC was upgraded by improving the safety of the magnets to prevent incidences like the one that happened on the 19th September 2008, where a magnet quench occurred damaging over 50 magnets and the vacuum pipe, delaying the start of the LHC physics program by more than a year. On the 5th of April 2015, the LHC was restarted and a center-of-mass energy of 13 TeV was soon reached. Fig. 3.2 shows the integrated delivered and recorded luminosity of the CMS detector per day for proton-proton collisions with a center of mass energy of $\sqrt{s} = 13\,\text{TeV}$. Before the winter shutdown in December 2015, the LHC delivered 4.22fb^{-1} of proton-proton collision data to the CMS experiment of which $3.81\,\text{fb}^{-1}$ were recorded.

The high energy scale reached at the LHC makes it possible to measure SM processes with never before reached precisions and to look for physics beyond the standard model in a parameter space that was not reachable with former collider experiments. On the 4th of July 2012, the CMS and ATLAS experiment announced the discovery of a new boson, whose behavior is consistent with a Higgs boson. Since then, the newly discovered boson was identified as a Higgs boson by verifying many of its properties predicted by theory. By combining the results of the 7 and 8 TeV CMS and ATLAS results, the combined measured Higgs boson mass was found to be $m_H = 125.09 \pm 0.21(\text{stat}) \pm 0.11(\text{syst})$ [53].

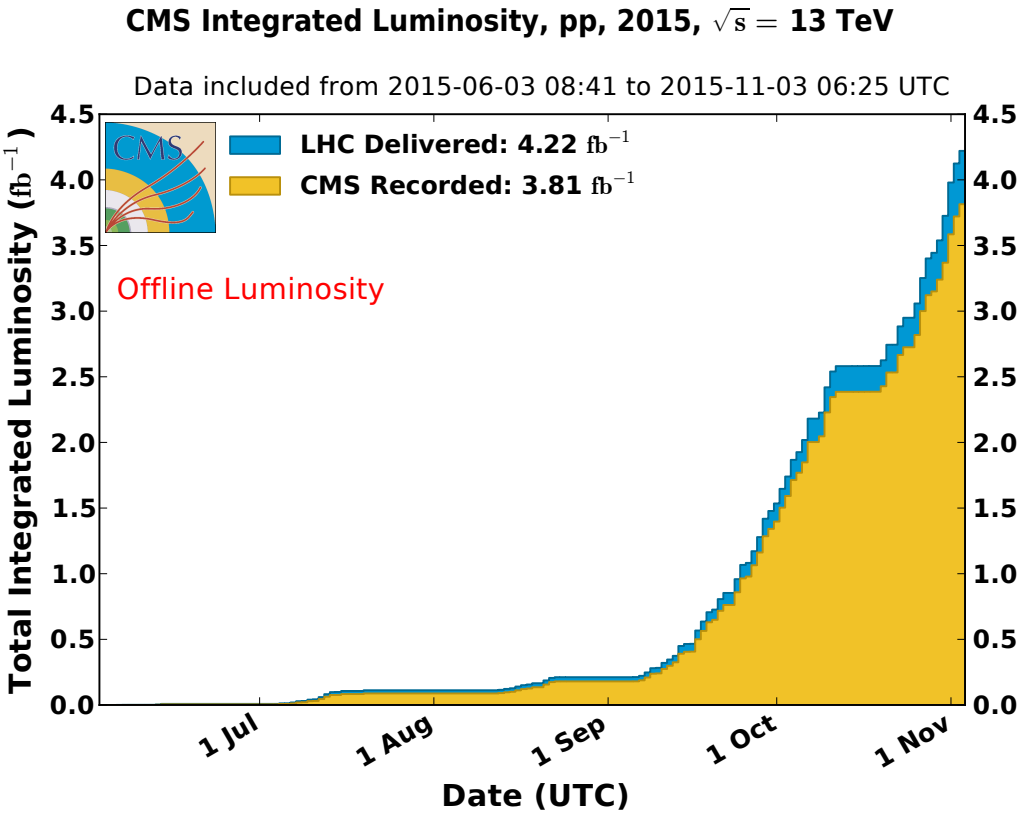

Figure 3.2: Integrated delivered and recorded luminosity of the CMS detector per day for proton-proton collisions with a center of mass energy of $\sqrt{s} = 13\,\text{TeV}$ in 2015 [54].

3.2 Kinematic Variables

In this section the most important variables used to describe the detector and the kinematic properties of an event and its particles are introduced.

The x-axis of the coordinate system used at the CMS-Detector is pointing towards the center of the LHC-ring. The y-axis is pointing upwards and the z-axis is pointing in the direction of the beam axis.

The angles used to describe the tracks of particles and the position of detectors are the polar angle θ, which is measured with respect to the z-axis, and the azimuthal angle ϕ, measured with respect to the x-axis in the x-y-plane.

The pseudorapidity η is a value for how close to the beam axis the particle is moving. It is defined as

$$\eta = -\ln \tan \frac{\theta}{2}. \tag{3.2}$$

ΔR is a Lorentz invariant measurement of distance between two objects

$$\Delta R = \sqrt{(\Delta\eta)^2 + (\Delta\phi)^2}. \tag{3.3}$$

As the longitudinal momentum of the initial partons in a proton-proton collision at the

LHC are not well known, the transverse momenta p_T of particles play an important role in describing events.

$$p_T = p \cdot \sin\theta \tag{3.4}$$

Accordingly, the missing transverse momentum $\vec{E}_{T,\text{miss}}$ is defined as the negative vectorial sum of all measured transverse particle momenta

$$\vec{E}_{T,\text{miss}} = \sum \vec{p}_T \tag{3.5}$$

and the missing transverse energy is the magnitude of $\vec{E}_{T,\text{miss}}$.

3.3 CMS detector

The very ambitious research endeavours at the LHC lead to very high requirements for the experiments. Furthermore, the very high bunch crossing rate of 40 MHz leads to pile up (PU), i.e. the occurrence of several interactions during one bunch crossing. Both have major implications for the trigger system, which has to reduce the event rate to an acceptable level, and the tracker and front-end electronics, which must be radiation hard enough to survive this very hostile environment for extended periods of time. The CMS detector [50] has been designed with these requirements in mind. It consists of several subdetectors, arranged in layers around the primary interaction point.

The main detector subsystems, from innermost to outermost, are:

- **Inner Tracker**: It consists of silicon pixel and strip detectors to reconstruct the tracks of charged particles.
- **Electromagnetic calorimeter (ECAL)**: The lead-tungstate scintillating-crystals electromagnetic calorimeter is mainly used to detect and measure the energies of photons and electrons.
- **Hadronic Calorimeter (HCAL)**: The ECAL is enveloped by a brass-scintillator sampling hadronic calorimeter. Both calorimeters are used to measure energies of hadrons.
- **Superconducting solenoid**: A superconductive solenoid provides a magnetic field of 3.8T that deflects charged particles to measure their p_T.
- **Muon detector**: Drift chambers interleaved with the magnet iron return yokes as the outermost parts of the detector are used to detect muons. Further detector types are used for the muon detection at large $|\eta|$ and for trigger purposes.

Each detector is divided into a barrel and a forward part. The barrel is the central part at low $|\eta|$. In this region, the detectors are perpendicular to the beam axis and

designed to measure particles with high transverse momenta. The forward calorimeters are endcaps placed in a region $3 \leq |\eta| \leq 5$. They measure particles with a high longitudinal momentum along the z-direction which would otherwise leave the detector undetected, leading to missing energy. A schematic overview of the CMS detector and it's subsystems is shown in Fig. 3.3.

The CMS detector has several, distinguishing features:

- Charged particles can be reconstructed with a good resolution and efficiency by the tracker. Tau leptons and b jets can be tagged efficiently, which is important for many BSM searches, as well as the $h \to b\bar{b}$ and $h \to \tau^+\tau^-$channel.
- Excellent resolution is provided by the electromagnetic calorimeter resulting in a very good photon and electron reconstruction efficiency. This is very important for e.g. $h \to \gamma\gamma$ searches.
- HCAL with large hermetic coverage. This is important, so that no strongly or electromagnetically interacting particles can escape the detector undetected. The $E_{T,\text{miss}}$ would otherwise loose its significance in indicating the presence of neutrinos or other unknown particles that only interact weakly.
- Good muon identification and di-muon-transverse-mass resolution due to the high magnetic field and the compact muon detector, giving the experiment it's name.

The whole detector has a length of 21.6 m, a diameter of 14.6 m and weights 12500 tons. In the following sections, the different subdetectors will be described in detail.

3.3.1 Inner Tracker

The inner tracker of the CMS detector was designed to measure the path of charged particles with high precision and efficiency. This detector component is of the utmost importance for the reconstruction of secondary vertices from e.g. b-quark decays, which will play an important role for the analysis presented later in this thesis in Chapter 6. The inner tracking system consists of a pixel detector and a strip detector. In a region close to the beam axis at a distance r of 4.4 to 10 cm, where the particle flux is highest, pixel detectors are used to keep the occupancy low (10^{-4} per pixel per bunch crossing) and to have a good granularity to precisely reconstruct secondary vertices from decaying b quarks and from additional soft interactions. Three pixel layers are installed in the barrel regions ($|\eta| \leq 2.5$) at a distance of 4.4, 7.3 and 10.2 cm. In the forward regions two pixel endcaps are installed at both sides at a distance of $|z| = 34.5$ and 46.5 cm covering a region from $r = 6$ to 15 cm. The size of a pixel cell is 150x100 μm. The pixel pitch of 100 μm has been chosen, to always have charge sharing between at least two pixel cells due to the drift introduced to the electrons in the sensor material by the magnetic field.

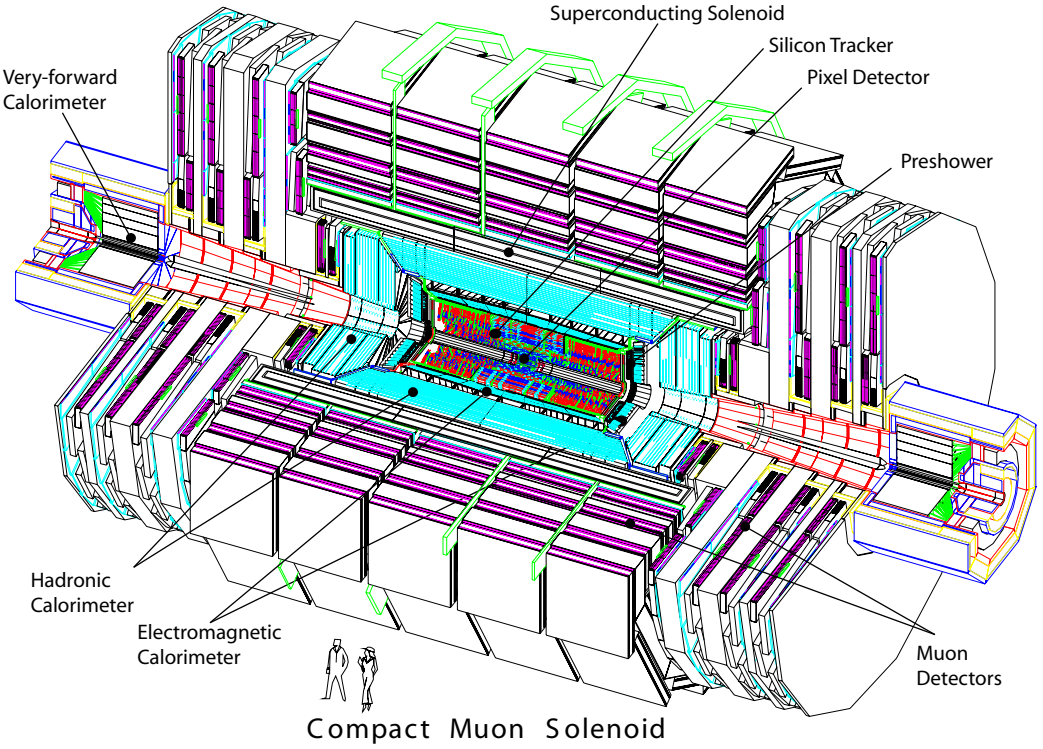

Figure 3.3: Schematic overview of the CMS detector and it's subsystems [50].

Further away from the beam axis at $20 \leq r \leq 110\,\text{cm}$ the diminished particle flux allows for the use of silicon microstrip detectors to save costs. The dimensions of the microstrip detectors vary from 10 to 25 cm in length and from 80 to 180 μm in pitch. 10 layers of microstrip detectors are installed in the barrel region while 9 endcap layers at each end cover the forward regions. Additionally 3 inner discs cover the area between the barrel layers and the endcap.

Overall a p_T resolution of 1.5% for 100 GeV particles and a hit resolution of 15 μm can be achieved with the 66 million pixels and 9.6 million silicon strips of the inner tracker [55]. In Fig. 3.4 a schematic view of the tracking system is shown. The full tracking system has a length of 5.8 m and a diameter of 2.5 m.

In the end of year technical stop 2016/2017 the pixel detector will be exchanged for an upgraded version that features an additional layer, CO_2 cooling and a digital read-out chip (ROC). A test beam analysis of a prototype ROC for this upgrade is presented in Chapter 4 of this thesis.

3.3.2 Electromagnetic Calorimeter

The electromagnetic calorimeter (ECAL) is located between the inner tracker and the hadronic calorimeter. The most important purpose of the ECAL is to measure electron and photon energies. It has been designed to reconstruct the two photons of the Higgs

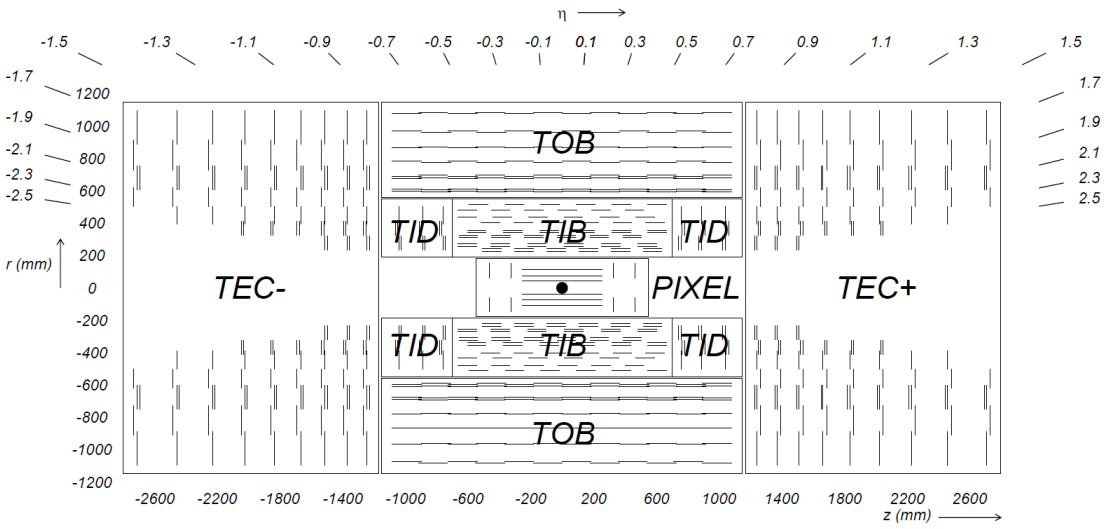

Figure 3.4: Schematic view of the CMS tracking system consisting of the pixel detector, inner barrel (TIB), outer barrel (TOB), inner disks (TID), and endcaps (TEC) [50].

decay with very high precision. For unconverted photons with a transverse energy of more than 100 GeV the energy resolution is better than 0.5%. The ECAL consists of 61200 tungstate crystals in the barrel regions, which spans a pseudorapidity region of $|\eta| \leq 1.479$ and 7324 crystals in the endcap region, which extends up to $|\eta| \leq 3.0$. The lead tungsten compound($PbWO_4$) used for the crystals is very dense, which leads to a short radiation length, but still transparent. The short radiation length is important, because the ECAL has to fit into the superconducting solenoid together with the tracker and the hadronic calorimeter. The crystals have a depth of 25.8 radiation lengths, meaning that almost all of the energy of a photon or electron will be deposited in the crystal. The crystals emit their light very fast. 80% of their light is emitted in 25 ns, which is the time between bunch crossings at the LHC design luminosity. However, the light yield of the lead tungstate crystals is low, which poses high requirements on the used photodetectors. In the barrel region, avalanche photodiodes are used as photodetectors, while the endcaps use vacuum phototriodes. A small gap exists between the ECAL barrel and endcaps at a pseudorapidity range of $1.479 < |\eta| < 1.566$. For electrons or photons in this range, no precise energy measurement can be provided.

Before the ECAL endcaps, a pre-shower (PS) detector, consisting of two lead and two silicon strip layers is employed to initiate showering processes. The resolution of the silicon strip layers was designed to be good enough to distinguish single photons from di-photon neutral pion decays.

The crystals are paired into blocks of 25 crystals which are arranged in a 5x5 geometrical pattern. For every five crystals, there is a so called very front end board. It amplifies and digitizes the signal of 5 crystals. The information from the very front end board is then transmitted to the front end board, where the information for a whole cluster of

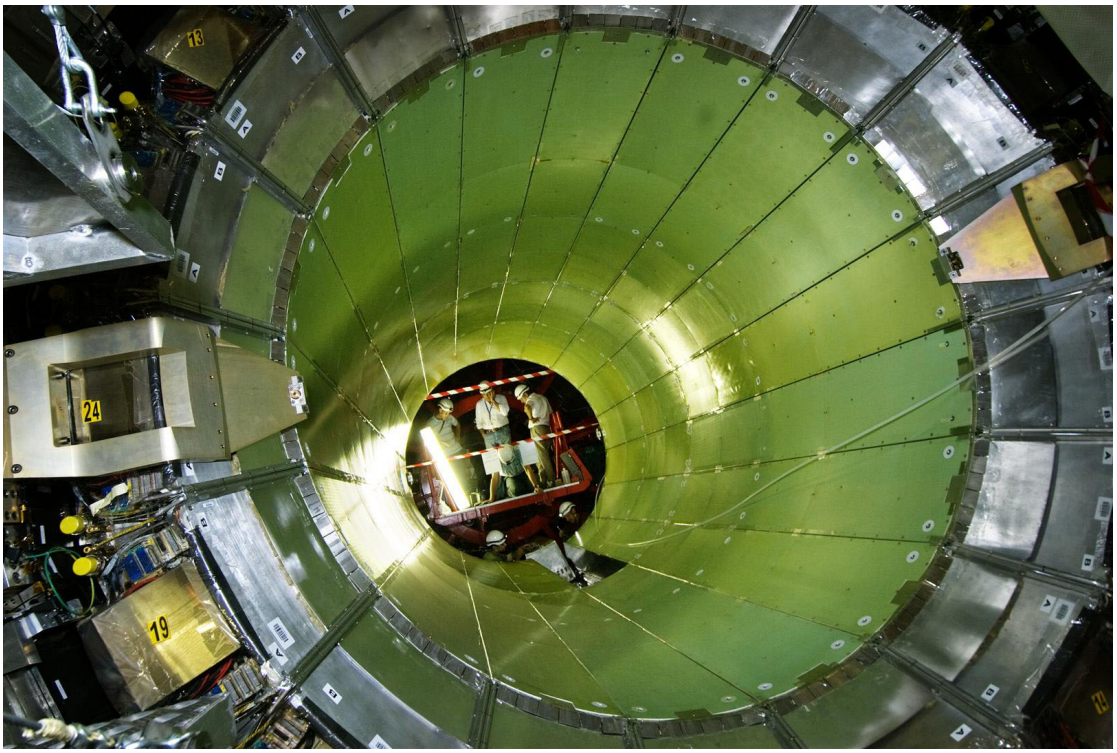

Figure 3.5: View on the inside of the electromagnetic calorimeter barrel [56].

5x5 crystals is collected and transmitted, depending on the trigger information received by the front end board.
Up to energies of 500 GeV, which is when shower leakage through the ECAL becomes relevant, the energy resolution can be parametrized by the following formula:

$$\left(\frac{\sigma}{E}\right)^2 = \left(\frac{S}{\sqrt{E}}\right)^2 + \left(\frac{N}{E}\right)^2 + C^2. \tag{3.6}$$

S is the stochastic term. It parametrizes stochastic fluctuations in scintillation and shower shape. The noise term N sums up noise contribution from electronics, digitization and pileup. C is the constant term, mainly driven by contributions from the non-uniformity of the longitudinal light collection, intercalibration errors and leakage of energy from the back of the crystals. In a test beam analysis, the central values for S, N and C were measured to be $S = 2.8\%$, $N = 0.12$ and $C = 0.30\%$. A View on the inside the ECAL barrel is shown in Fig. 3.5.

3.3.3 Hadronic Calorimeter

The hadronic calorimeter (HCAL) is the detector component responsible for measuring the energy of strongly interacting particles. It is also the most important component for indirectly measuring neutrinos, as a good resolution of the missing transverse energy is strongly depending on the hermetic coverage of the HCAL, as jets, deploying their

energy outside of the detector, will result in missing transverse energy. The HCAL can be divided into four parts. The hadron barrel (HB), hadron endcap (HE) and hadron forward (HF) are located between the ECAL and the superconducting solenoid while the hadron outside (HO) is placed outside of the solenoid. The HB covers a pseudorapidity of $|\eta| \leq 1.4$. The HE measures particles in a region $1.3 \leq |\eta| \leq 3.0$ and the HF is placed very close to the beam axis at $3.0 \leq |\eta| \leq 5.2$. The HO is placed behind the HB at a region $|\eta| \leq 1.2$. The HCAL is a sampling calorimeter, which means that it consists of alternating layers of scintillators and absorber material. In the HB, HE and HO brass was chosen as absorber material as it has a short hadronic interaction wavelength and is not magnetic. Between the layers of brass, plastic scintillator tiles are placed which are read out by optical fibers connected to photo diodes. The thickness expressed in hadronic interaction wavelengths varies between 6 and 10 in the barrel region, depending on the $|\eta|$ value. Due to its proximity to the beam pipe, the HF experiences the largest particle flux of all detector components. Therefore, radiation hard quartz fibers, read out by photomultipliers, are used as scintillator material while steel is used as absorber material.
The resolution of the HCAL barrel was studied in test beams with particle energies between 2 and 350 GeV and was found to be [57]:

$$\left(\frac{\sigma}{E}\right)^2 = \left(\frac{84.7\%}{\sqrt{E}}\right)^2 + (7.4\%)^2. \tag{3.7}$$

In Fig. 3.6 the HB is shown, as it is being inserted into the solenoid.

3.3.4 Muon detectors

The muon detectors are the outermost part of the CMS detector. They consist of four muon stations in the region $|\eta| \leq 2.4$. The muon stations are interleaved with the iron return yokes of the magnet. In the muon barrel region aluminum drift tube chambers (DT) are used to measure the muon p_T. The DTs within a chamber have two different orientations, one to measure the muon coordinate in the $r - \phi$ plane and the other orientation measures the z coordinate of the muon. In the muon endcaps cathode strip chambers (CSC) are used, which have a faster response time of approximately 1 ns and are radiation harder than the DTs. This is done because higher muon rates are expected in the forward region. The CSCs have cathode strips running radially outwards to give a measurement of the muon position on the $r-\phi$ plane while perpendicular anode wires provide a measurement of the pseudorapidity η of the muon. The DTs in the barrel region provide a position resolution of approximately 200 μm, while the CSC provide a position resolution of $100 - 200\,\mu$m depending on the η value of the measured muon.
In both, the barrel and the endcap region, additional measurements are done by resistive

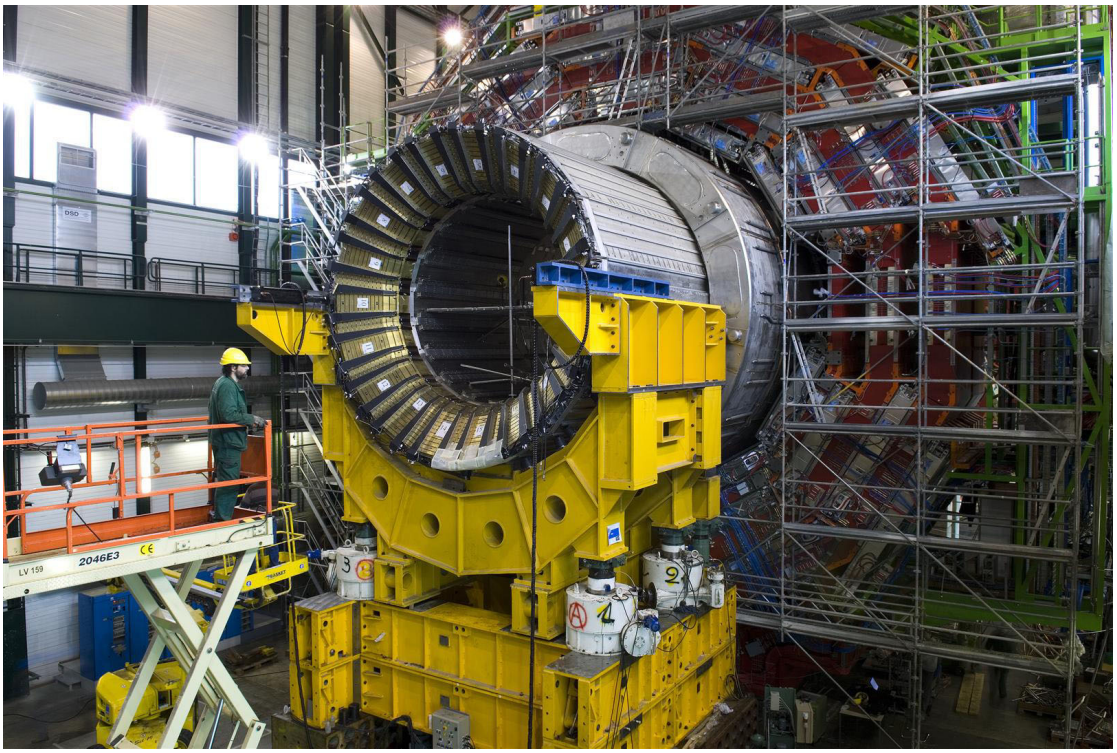

Figure 3.6: The HB, as it is inserted into the detector [58].

plate chambers (RCP). They have a relatively low momentum resolution but a fast response time and therefore a good time resolution. The RCPs are used to link a measured muon to the correct bunch crossing and can be used as a trigger for muon events. Cosmic muons are detected by the RCPs. The measurement of the muon system together with the information of the inner tracker has a p_T resolution of $1 - 10\%$ for muons with a p_T of 1 TeV. A picture of the muon barrel region is shown in Fig. 3.7.

3.3.5 Trigger System

At the LHCs design luminosity, 10^9 interactions take place per second. As the CMS experiment is only capable of recording approximately 1000 interactions per second, a system that selects the event that will be recorded for later analysis has to be employed. This work is done by the two level trigger system consisting of a combination of hardware and software triggers. The level-1 trigger [60] reports the energies deposited in the different calorimeter towers or supercrystals, if the energy exceeds a certain threshold, and hit patterns in the muon stations. The readout of the different subsystem is combined to form a p_T sorted list of object candidates. This output is collected at a global trigger, which decides if the event is processed further. The lever-1 trigger has a processing rate of around 100 kHz and is implemented purely in hardware by application-specific integrated circuits (ASICs) and programmable logic chips (FPGAs).
The second stage is the software based high level trigger (HLT) [61] which has access

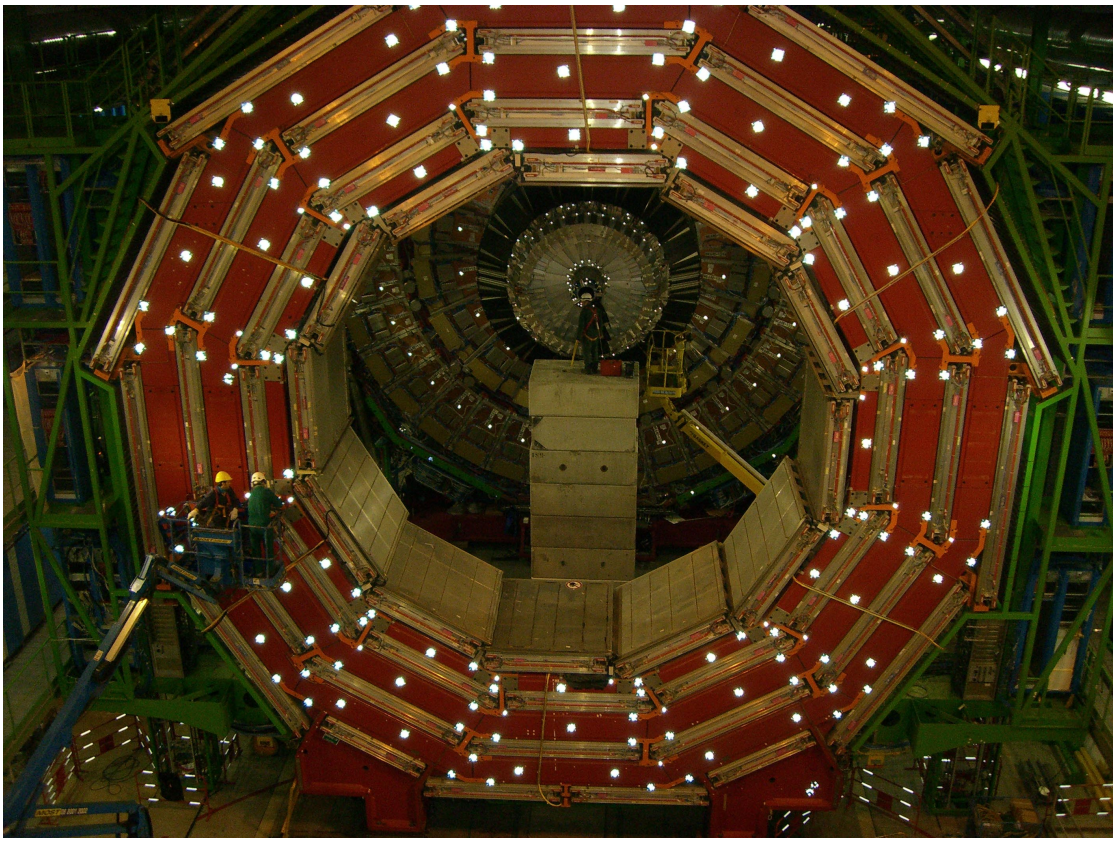

Figure 3.7: Picture of the muon chambers and the iron return yokes [59].

to the whole event information including the tracks. The objects for the HLT are reconstructed with much increased precision compared to the reconstruction by the L1 trigger system by applying algorithms similar to the algorithms used in the full offline event reconstruction. Based on the different HLT paths chosen for data acquisition, the HLT decides which of the 1000 events per second to store. Of these 1000 stored events, approximately 300 can be fully reconstructed on the fly. The remainder of the events is stored for later reconstruction.

3.4 Object Reconstruction

To make use of all the signals received by the various subcomponents of the detector during a collision, the signals have to be translated into meaningful physics objects. In the following chapter the Particle Flow (PF) algorithm, which lays the groundwork of the object reconstruction, and several algorithms build on top of the PF Algorithm to distinguish further between different particles will be described.

3.4.1 Particle Flow

The Particle Flow algorithm [62] tries to reconstruct all stable particles within a given event by combining the information from all detector sub-components. This is done in iterative steps from easiest to hardest to identify particle type. The tracks and calorimeter responses which can be attributed to a reconstructed particle are no longer considered for the rest of the algorithm.
With its high magnetic field to split up charged particles, its excellent tracking capabilities and its high granularity electromagnetic calorimeter the CMS detector is perfectly suited for this algorithm.
The algorithm starts with tracks of charged particles in the inner tracker. As the momentum resolution of the tracker for most charged particles is vastly superior to the calorimeter resolution and the direction of the particle measured by the tracker is of utmost importance for linking tracks to energy clusters, it is important to reconstruct tracks with an efficiency as close as possible to 100% while simultaneously keeping the amount of fake tracks, which might introduce large amounts of energy excesses, as small as possible. This is achieved by using an iterative approach which first reconstructs the tracks with the best track fits. The tracker hits belonging to these tracks are removed and not considered for further iterations of the track findings. With the now reduced combinatorial background, tracks with worse fits can be reconstructed with higher purity. This process is repeated five times with relaxed constraints on the distance of the track to the beam pipe in the fourth and fifth iteration, allowing for the reconstruction of tracks belonging to conversion photons, long-lived particles or particles from nuclear interactions with the tracker material.
Next the energy deposited in the calorimeters is clustered. This step is performed separately for the following components: HCAL barrel, ECAL barrel, ECAL endcaps, first PS layer and second PS layer. No clustering is done for the HF. First local energy maxima above a certain threshold are detected. The cells which measured these local maxima are then used as cluster seeds. The clusters grow outwards from cluster seeds by aggregating neighboring cells surpassing a threshold above the noise level of the specific calorimeter.
The tracks and clusters are then linked. Tracks are linked to clusters if the extended track connects to a point within the cluster boundaries. Tracks with tangents that connect to an ECAL cluster are also linked to account for possible Bremsstrahlung photons. Two clusters in different calorimeters are linked if the cluster in the finer grained cluster is enveloped by the cluster in the other calorimeter. If a track in the muon chambers together with a track in the silicon tracker returns an acceptable global fit χ^2 value, the muon track is linked with the silicon tracker track that gives the smallest χ^2 value for the global fit.

Finally the particle flow algorithm aims to reconstruct and identify all of the particles to give a complete description of the event. First each muon chamber track linked with a silicon tracker track will result in a particle flow muon if the measured momentum in the tracker is compatible within three sigma with the momentum as measured by the combined tracks. The track is removed from the tracks for further consideration and an estimate of the muon energy that was deposited in the calorimeters will be taken into account for further reconstructions.
Next the electrons are identified by looking for characteristic signs of energy loss through Bremsstrahlung and short tracks created by electron-positron showers. Again the corresponding tracks and the energy deposits in the ECAL linked to the electrons and Bremsstrahlung photons are removed from further processing.
After some further track cleaning which aims to identify and remove fake tracks, the remaining tracks are identified as charged hadrons. For calorimeter energy deposits that significantly exceed the momentum given by the linked tracks, a particle flow photon and/or a neutral hadron are created to account for the discrepancy. If the energy excess is larger than the energy measured in the ECAL, a photon and a neutral hadron are created of which the photon will have the energy deposited in the ECAL while the hadron will account for the remaining excess. Otherwise only a photon will be created. The remaining unlinked ECAL and HCAL clusters finally give rise to further photons and neutral hadrons respectively.

3.4.2 Muons

Muons are the particles that are easiest to identify in the CMS detector as they have the longest mean free path within the detector with respect to the other electromagnetically and strongly interacting particles. Therefore they have the unique property of interacting with the outermost detector components, the muon chambers.
Besides the PF algorithm muon reconstruction, there are two additional muon reconstruction algorithms, the global and the tracker muon reconstruction algorithms [63]. The global muon reconstruction starts from a track in the muon chambers and tries to match it to a track in the tracker by comparing their parameters after propagating them onto a common surface. The following global fit, which includes the muon chambers track, can improve the momentum resolution for muons with a high transverse momentum of $p_T > 200\,\text{GeV}$ with respect to a tracker-only fit.
Tracker muons are reconstructed by an inside-out approach starting from a tracker track which is then propagated out by taking into account the magnetic field, energy losses and Coulomb scattering in the detector material. The tracker track will be identified as a tracker muon if its propagated track matches to at least one so called muon segment, which is a short track stub made of DT or CSC hits.

The muon identification used for the analysis presented in Chapter 6 will make use of all three presented reconstruction algorithms in addition to some quality cuts to further improve the purity of the muons.

3.4.3 Jets

Jets are produced by the strong interaction between gluons and quarks. In simple terms they are cone shaped showers that can consist of many particles. To reconstruct jets, the jet sub-particles have to be clustered together by a clustering algorithm. The algorithm has to fulfill requirements towards infrared and collinear (IRC) safety. That means that the set of hard jets should not change if a collinear splitting is introduced into an event (collinear safety) or if a soft emission is added (infrared safety) [64].
The jet clustering algorithm used throughout this thesis is the IRC-safe $anti-k_t$ algorithm [65]. The algorithm works by providing a measure for distance d_{ij} between two entities (particles or subjets) i and j and a distance d_{iB} between an entity i and the beam direction:

$$d_{ij} = min(p_{T,i}^{-2}, p_{T,j}^{-2}) \frac{\Delta R_{i,j}^2}{R_{\text{conesize}}^2} \tag{3.8}$$

$$d_{iB} = p_{T,i}^{-2}, \tag{3.9}$$

where R_{conesize} is a variable parameter which determines the cone size of the jets. Starting with the entity with the smallest distance to the beampipe, which for this algorithm is the entity with the highest p_T, the algorithm begins the clustering process. If the distance to the closest second entity d_{ij} is smaller than the distance to the beampipe d_{iB}, the entities i and j are combined into one and the process repeats. Otherwise the entity is declared to be a final state jet and is removed from the list of remaining entities. This process repeats until no entities are left. In this way, the algorithm creates clusters around the particles with the highest p_T that are cone-shaped in η-ϕ.
To reduce the number of jets faked by noise in the hadronic calorimeter or by leptons, additional identification cuts will be applied to the jets before they are used in the analysis presented in Chapter 6.
To mitigate systematic shifts in the jet energy measurement with respect to the true jet energies, correction factors are applied [66]. The jet energy correction consists of multiple levels of corrections, with each level taking the output of the previous level as an input. First an offset correction aims to remove energy contributions from noise and pile-up. Next a MC correction is derived from simulation and removes the non-uniformity of the response in η and p_T. A residual correction follows next. It aims to remove small difference observed between simulation and data by applying a relative correction. Finally

an absolute correction derived from γ/Z+jets events, which should contain no neutrinos and therefore no missing transverse energy except from mismeasurements, is applied.

3.4.4 B-Tagging

Identifying jets stemming from a b-quark decay (b jets) is crucial for many analyses. This section introduces the Combined Secondary Vertex (CSV) algorithm which will be used to identify b-jets [67] within the analysis presented in Chapter 6. The algorithm makes use of characteristic features of b quarks like their relatively long lifetime and the high momentum spectra of their daughter particles.
Due to the non negligible lifetime of the b quark, the vertex for tracks belonging to the b-quark decay products is displaced from the primary vertex. With its high resolution tracking system the CMS detector is ideally suited to reconstruct these vertices. The CSV algorithm makes heavy use of observables related to the reconstruction of these secondary vertices, like the distance to the primary vertex in the transverse plane, the vertex mass, the number of tracks connected to the vertex and the ratio of energy carried by tracks connected to the secondary vertex to the energy of all tracks of the jet. If no secondary vertex was reconstructed, the CSV algorithm still provides some separation power by using track impact parameters of the tracks belonging to the jet constituents. They tend to be positive for particles from the decay of particles traveling in the direction of the jet-axis, like b quarks, while they have equal probability of being positive or negative for prompt tracks.
The final discriminant, called CSV-value, is a combination of two separate discriminators. One to distinguish light jets from b jets and one to distinguish c jets from b jets. A loose, medium and tight working points, corresponding to rates of jets falsely identified as b jets of about 10%, 1% and 0.1% respectively, are provided. The medium working point, used for b-tagging in the analysis presented later in this thesis, has been shown to yield an b-jet identification efficiency of about 69% [68].

3.4.5 Hadronic Taus

Tau leptons decay before they reach any of the detector components. In approximately 35% of all cases, they decay into two neutrinos and an electron or muon. The electron or muon is then reconstructed as such. In all other cases the tau lepton decays into a neutrino and one or more mesons. As can be seen from the branching ratios for the different hadronic decay modes listed in Tab. 3.1, the most dominant hadronic tau decay modes contain either one or three charged mesons (mostly pions), often accompanied by neutral pions. The clustered hadrons resulting from these hadronic decays will be denoted as hadronic taus (τ_h) for the remainder of this thesis.
The hadronic taus are reconstructed by the hadron plus strip algorithm (HPS) [69]. The

Decay Mode	**Resonance**	**Mass [MeV]**	**Branching Ratio**
$\tau^{\pm} \to \pi^{\pm}\pi^0\nu_\tau$	ρ	770	25.5%
$\tau^{\pm} \to \pi^{\pm}\nu_\tau$	-	-	10.8%
$\tau^{\pm} \to \pi^{\pm}\pi^0\pi^0\nu_\tau$	a_1	1260	9.3%
$\tau^{\pm} \to \pi^{\pm}\pi^{\mp}\pi^{\pm}\nu_\tau$	a_1	1260	9.0%
$\tau^{\pm} \to \pi^{\pm}\pi^{\mp}\pi^{\pm}\pi^0\nu_\tau$	-	-	2.7%
Other hadronic modes	-	-	7.5%
Total hadronic modes			64.8%

Table 3.1: Branching Ratios of the most dominant hadronic tau lepton decay modes [6].

algorithm starts from a PF jet reconstructed by the $anti-k_t$ algorithm with a cone size of $R_{\text{conesize}} = 0.5$. Photons from π^0 decays can convert to electrons/positrons in the tracker material. The bending of these electrons/positrons leads to π^0 calorimeter signatures that are smeared out in the azimuthal direction. Therefore the HPS algorithm tries to reconstruct π^0s in so called "strips" built out of PF photons and electrons/positrons. The seed of the strip reconstruction is the electromagnetic particle with the highest p_T within the jet. If another electromagnetic particle is found within a window of $\Delta\eta < 0.05$ and $\Delta\phi < 0.20$ of the strip center, the electromagnetic particle with the highest energy is added to the strip and the strip four-momentum is recalculated. This is repeated until no further particle is found. The HPS algorithm then tries to combine the reconstructed strips with the charged hadrons in the jet by identifying them as belonging to one of the following decay modes:

- **Single charged hadron:** Decays with one charged hadron and no π^0 or a π^0 that did not have enough transverse momentum to be reconstructed.
- **Single charged hadron + one strip:** Decay with one charged hadron and a π^0, where the two photons of the π^0 decay were reconstructed as one strip due to their proximity.
- **Single charged hadron + two strips:** Decay with one charged hadron and a π^0 with two well reconstructed photons from the π^0 decay.
- **Three charged hadrons:** Decay with three charged hadrons. They are required to originate from the same secondary vertex.

Decays where the tau decays into one charged hadron and two π^0s or three charged hadrons and one π^0 are also covered by the precedingly named decay topologies.

After some requirements on the spread of the reconstructed τ_h components the τ_h is reconstructed by assuming that all charged hadrons are pions and requiring that their invariant masses are consistent with the mass of the intermediate resonance of the assumed decay mode. If the τ_h can be reconstructed by more than one decay mode hypothesis, the hypothesis which gives the highest τ_h transverse momentum is chosen.
Electrons are sometimes misidentified as hadronic taus. Electrons that are linked to energy deposits in the calorimeters can be identified as a hadronic tau by the single charged hadron decay hypothesis. If the electron emitted a Bremsstrahlung photon, it can also be reconstructed by the single charged hadron plus one strip hypothesis. To reduce the number of electrons faking a hadronic tau, a boosted decision tree (BDT), which is a multivariate analysis technique (MVA), that uses many of the variables used for electron identification is trained. The very loose working point of the BDT used for the analysis in Chapter 6 has a τ_h selection efficiency of 90% while reducing the amount of misidentified electrons to approximately 2.4%.
Muons are less likely to be reconstructed as a τ_h. To reject misidentified muons, no hits in the two outermost muon station must be present within $\Delta R < 0.5$ around the τ_h direction. Furthermore the calorimeter energy linked to the leading track by the PF algorithm of the τ_h must exceed 20% of the track momentum. These requirements yield a selection efficiency of 95% and a muon fake rate of less than 0.1%.

3.4.6 Invariant mass of di-tau decays

Due to the neutrinos in the tau-decay products, reconstructing the invariant mass of a Higgs or Z boson decaying into two taus is challenging. By combining the visible tau-decay products the visible mass m_{vis} can be reconstructed. However, as the neutrinos are missing from this mass reconstruction, the invariant mass reconstructed by this approach tends to be very broad and shifted towards lower values than the invariant mass of the di-tau system.
The analysis presented in Chapter 6 will make use of the SVfit [70] algorithm. The SVfit algorithm uses the measured missing transverse energy and the visible tau-decay products to reconstruct the invariant mass of the di-tau system by a dynamic likelihood method. The invariant mass m_{SVfit} reconstructed by this algorithm is the mass for which the probability given by a weighted average of all hypothetical event configurations, compatible with the measured visible tau-decay products and missing transverse energy is maximized. For a more detailed description of the algorithm see [70].

3.4.7 Lepton Isolation

To distinguish prompt leptons from leptons produced in jets and to reduce the number of jets misidentified as leptons, an isolation requirement is introduced. The isolation is

a measure for the energy deposited by charged hadrons, neutral hadrons and photons in a cone in η-ϕ of $\Delta R < R_{\text{iso}}$ around the reconstructed lepton. To avoid contributions of particles from PU, only charged hadrons that can be traced to the primary vertex of the event contribute to the isolation. To estimate the contribution of neutral hadrons from PU events, the contribution from charged hadrons is multiplied by a factor of 0.5, which is the approximate ratio of neutral to charged hadrons. It is subsequently deducted. The isolation I is thus defined as:

$$P_{\text{Had}} = \sum p_T \quad \text{for all charged hadrons from the PV within } \Delta R < R_{\text{iso}} \tag{3.10}$$

$$E_{\text{Neut}} = \sum E_T \quad \text{for all neutral hadrons within } \Delta R < R_{\text{iso}} \tag{3.11}$$

$$E_{\text{Phot}} = \sum E_T \quad \text{for all photons within } \Delta R < R_{\text{iso}} \tag{3.12}$$

$$P_{\text{PU}} = \sum p_T \quad \text{for all charged hadrons from PU within } \Delta R < R_{\text{iso}} \tag{3.13}$$

$$I = P_{\text{Had}} + Max(0, E_{\text{Neut}} + E_{\text{Phot}} - 0.5 \cdot P_{\text{PU}}) \tag{3.14}$$

Electrons and muons usually have a requirement on the relative isolation $I_{rel} = \frac{I}{p_T}$ with an isolation cone of $R_{\text{iso}} = 0.3$ or 0.4.
For the isolation requirement of hadronic taus, the charged hadrons and photons used to reconstruct the τ_h are excluded from the isolation. The isolation cone is chosen to be $R_{\text{iso}} = 0.5$. The cone for the neutral hadron subtraction is slightly increased to 0.8 and the neutral to charged hadron factor is decreased to 0.46 as this has been shown to result in a PU independent selection efficiency.

3.4.8 Missing Transverse Energy

The almost completely hermetic design of the CMS detector allows for the detection of all strongly and electromagnetically interacting particles with a high precision. Weakly interacting particles, like neutrinos or other unknown particles, however only interact very rarely with the detector material and therefore leave the CMS detector undetected. To indirectly detect these particles, one can look at the missing energy in the transverse detector plane ($\vec{E}_{T,\text{miss}}$) of an event.
The $\vec{E}_{T,miss}$ is reconstructed by the particle flow algorithm and is defined as the negative vectorial sum of the transverse momenta of all particles in the event.

$$\vec{E}_{T,\text{miss}} = -\sum_{\text{PFparticles}} \vec{p}_T \tag{3.15}$$

The resolution of the $\vec{E}_{T,\text{miss}}$ is sensitive to detector malfunctions and reconstruction effects resulting in mismeasurements of particles. As the resolution of leptons and photons is quite good, the largest effect on the $\vec{E}_{T,miss}$ resolution stems from jet mismeasurements. This effect is increased if more jets are present in the event due to additional PU

interactions.

To improve the $\vec{E}_{T,\text{miss}}$ resolution for events with a large number of PU events, "Pileup per Particle Identification" is applied [71]. The PUPPI algorithm weights the contribution of each particle to the $\vec{E}_{T,miss}$ by a factor between 0 and 1. Particles that can clearly be identified as particles stemming from a PU interaction will receive a weight close to 0 whereas particles that are very likely to be part of the primary interaction receive a weight close to 1. The probability of a particle for being a particle from PU or from the primary interaction is estimated by a local shape variable α. It is a measure for the sum of energy from known primary interaction particles in the vicinity of the particle. The charged hadrons belonging to the primary interaction can be identified by linking their track to the primary interaction vertex. A particle from the primary interaction is likely to be near other particles from the primary interaction process, yielding a higher value for α than for particles from PU processes which do not have shower-like structures and are only close to particles from the primary interaction by chance.

On top of the PUPPI algorithm, an MVA based algorithm trained to give a unity response for the recoil on Drell-Yan $Z \to \mu\mu$ events is applied. The MVA training uses different $\vec{E}_{T,\text{miss}}$ algorithm outputs as an input. The algorithms differ by which particle candidates are included in the $\vec{E}_{T,miss}$ calculation. The algorithms calculate the $\vec{E}_{T,miss}$ by including a combination of tracks connected and not connected to the primary vertex, jets connected and not connected to the primary vertex and unclustered neutral energy depositions. One of the used $\vec{E}_{T,miss}$ algorithms is the aforementioned PUPPI Met, which is the algorithm driving the resolution improvement of the MVA based $\vec{E}_{T,miss}$ with respect to the PF $\vec{E}_{T,\text{miss}}$.

Chapter 4

Test beam Analysis of an irradiated Phase I Pixel ROC

The current pixel detector will be exchanged for an upgraded version during the end-of-year technical stop 2016/2017 to cope with higher instantaneous luminosities and to not rely on the current pixel detector after the large amount of radiation it will have been exposed to. In the following chapter, the features of the new pixel detector, the layout of the sensor, and a test beam analysis to test the radiation hardness of the new readout chip (ROC) will be presented.

4.1 Phase 1 Upgrade

While the current pixel detector has been designed for a peak luminosity of $1 \cdot 10^{34}\,\mathrm{cm}^{-2}\mathrm{s}^{-1}$, luminosities close to $2 \cdot 10^{34}\,\mathrm{cm}^{-2}\mathrm{s}^{-1}$ are expected before the Long Shutdown 2 (LS2) in 2018. During LS2, the injector chain will be improved to deliver bunches with higher intensities and lower emittance, further increasing the luminosity. The current pixel detector will have problems coping with this high luminosity environment, as the buffer sizes and readout speed is not sufficient for the expected data rates. Furthermore, the resolution of the current pixel detector due to radiation damage is expected to worsen by roughly a factor of two, when assuming the radiation fluence expected until the end of phase I of $1.2 \cdot 10^{15}\,\mathrm{n_{eq}cm}^{-2}$.
To maintain a high tracking efficiency in high luminosity scenarios with increased PU and higher pixel occupancies, the current pixel detector will be exchanged by an upgraded version [72]. This exchange will take place during the end-of-year technical stop 2016/2017, before LS2, to maximize the integrated luminosity recorded by the upgraded detector. This will ensure that CMS can take full advantage of the improvements of the LHC performance expected before LS2. Exchanging the detector during a technical stop is made possible by the specific design of the CMS detector, allowing easy access

to the central detectors, so that they can be quickly removed and reinstalled.
The main features of the upgraded pixel detector are:

- Four barrel layers and three forward discs on each end instead of three barrel layers and two forward discs on each end.
- The radius of the beampipe will be decreased to allow the innermost layer to move 1.4 cm closer to the interaction point.
- A digital ROC and an improved readout chain will decrease the dynamic data loss by increasing the readout speed and buffer sizes.
- The digital ROC will allow for smaller pixel charge threshold which will help to maintain a good resolution after sustained radiation damage.
- Reduction of passive material by introducing CO_2 cooling and relocating electronics boards and connections out of the tracking volume.

One half of the modules of the fourth layer of the upgraded detector was built by the University of Hamburg in cooperation with DESY. The studies that will be presented in the following part of the thesis should ensure that an upgrade pixel ROC is radiation hard enough, to still perform well after having collected $500\,\mathrm{fb}^{-1}$ of data in the fourth layer. The sensor material and its layout are not changed with respect to the current CMS pixel design, but as the design is important for some parts of the test beam analysis presented in this chapter, it will be described shortly in the following section.

4.2 Layout of a CMS pixel cell

The size of a single pixel cell within the CMS pixel detector was chosen to be 150x100 μm. The choice of a pixel pitch of 100 μm was motivated by the intention to have optimal charge sharing properties, considering the Lorentz angle induced by the magnetic field after irradiation [73]. Charge sharing is very important for achieving a high resolution, as the shared charge enables the possibility to determine the position of a particle more accurately by applying a center-of-mass algorithm to the collected charges. The thickness of the sensor material is 285 μm.
For the sensor material a so called "n-in-n" design was chosen. The charge of a pixel cell is collected at high dose n-implant embedded in a high resistance n-substrate acting as the active medium. The p-implant on the backside forms the junction. The n-in-n sensor concept has three distinct advantages over a typical p-n diode.

- The n-in-n type design implies the collection of electrons instead of holes. The higher mobility of the electrons make them less prone to trapping after irradiation and increases the Lorentz-angle leading to increased charge sharing.

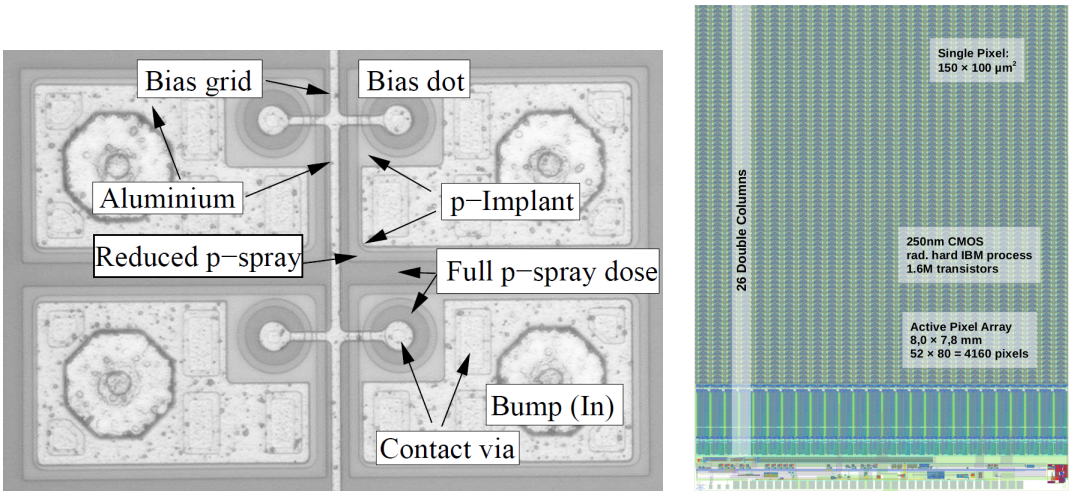

Figure 4.1: Sensor layout of four pixel cells (left) and geometric layout of a phase I upgrade ROC (right) [72] [74].

- The bias voltage needed to deplete a sensor rises with irradiation. After the n-type bulk has undergone charge sign inversion, the highest electric field is at the read out side of the sensor, allowing for under-depleted operation to avoid learge leakage-currents.
- When starting with n-type bulk material, it takes a higher radiation dose to reach acceptor levels at which the sensor can not be depleted anymore. The lifetime increases by the type inversion time.

To prevent conduction between pixels, p^+ dopants are diffused in between pixel cells (moderated p-spray). For quality assurance tests, like IV-measurements, and to prevent a large potential difference between pixels and the ROC in case of a missing bump bond, a punch-through structure (bias-dot) connects the pixels to a bias grid (See Fig. 4.1). Each pixel cell is connected to the ROC by an indium bump bond.

4.3 Layout of the CMS phase I pixel ROC

The phase I upgrade ROC is very similar in its geometric layout to its predecessor. 52x80 pixel cells are bump bonded to one ROC (Fig.4.1). They are organized in 26 double columns which each have their own data and time stamp buffer. Pixels with a charge surpassing a set pixel threshold are read out and a time stamp and the collected charge are stored in their respective buffers. Due to the increased buffer sizes, the new ROC is slightly larger, but as the increase in size is very moderate, the sensor layout and module design of the old detector can be used.

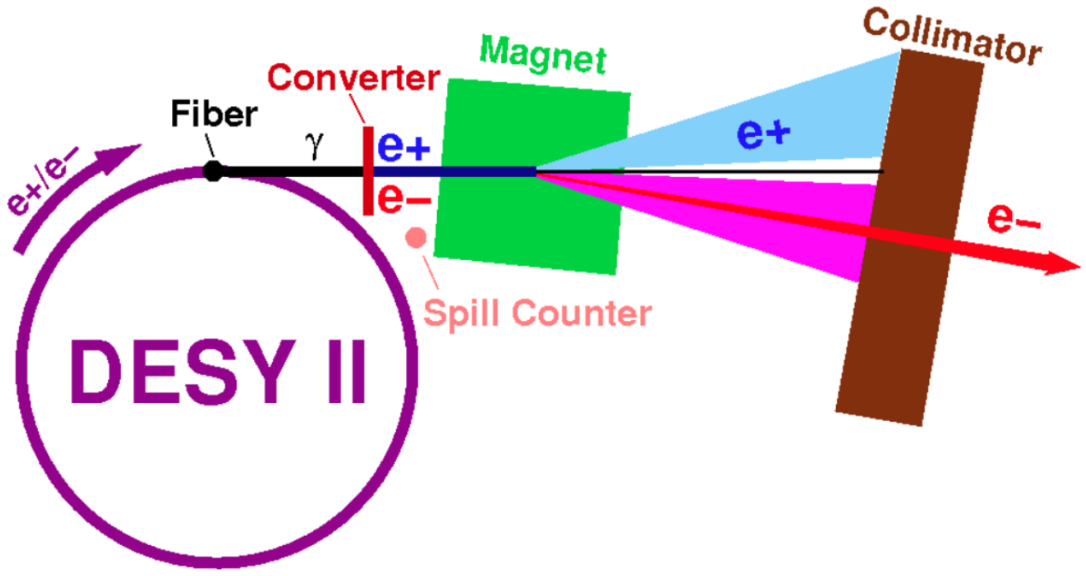

Figure 4.2: Schematic view of the beam generation at DESY. The electrons/positrons in the DESY II synchrotron generate Bremsstrahlung which is then converted to electron/positron pairs at a metal plate (converter).

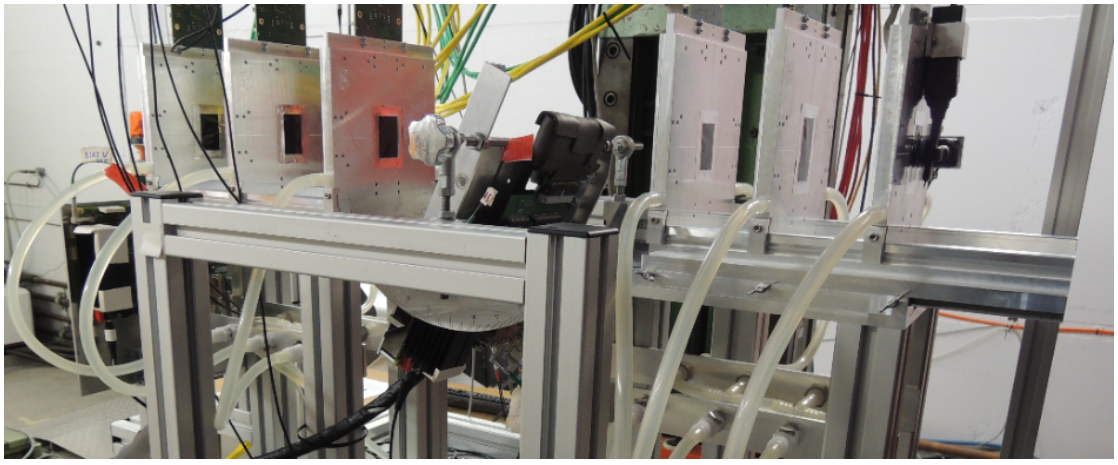

Figure 4.3: Picture of the DUT, wrapped in styrofoam for cooling purposes, between the telescope arms.

4.4 Beam Setup at DESY and Beam Telescope

To evaluate the performance of the ROC for the Phase I pixel detector upgrade, a test beam study has been carried out at DESY. The beam of up to 1000 positrons $\mathrm{cm}^{-2}\ \mathrm{s}^{-1}$ with an energy of 1 - 6 GeV is generated by first creating Bremsstrahlung by placing a carbon fiber in the DESY II synchrotron beam (see Fig. 4.2) [75]. The Bremsstrahlung photons are then converted to electron positron pairs at a copper plate. The electrons and positrons are split up and fanned out by a magnet before a collimator slices out the final beam.

The device under test (DUT) was placed between two arms of an EUDET telescope [76].

The EUDET telescope is a beam telescope based on monolithic active pixel sensors. It was developed by the EUDET consortium, a detector R&D collaboration for the International Linear Collider providing test beam infrastructure for detector R&D groups.

The telescope (Fig. 4.3) consists of six sensor planes with a complementary metal-oxide-semiconductor (CMOS) pixel sensor (Mimosa26) [77]. The sensor features quadratic pixels with a pitch of 18.4 μm.
Three sensor planes form the upstream arm of the telescope. Going along the beam direction they are followed by the DUT and three more sensor planes forming the downstream arm. A reference device is placed behind the downstream arm. Two pairs of scintillation triggers enclosing the telescope are placed at the front and the end of the telescope. The DUT is mounted on a hinge which allows tilting and turning, where tilting means a rotation around a fixed row and turning a rotation around a fixed column. With this setup, the telescope resolution reached at the point of the DUT is 4.8 μm [78].

The analyzed DUT is a single chip module, which has been irradiated with 24 GeV protons at CERN PS. The total delivered dose was 13 ± 1 Mrad, which is the expected lifetime dose for the fourth pixel detector layer. The ROC design is one of the first digital prototypes designed for the phase I upgrade by the Paul Scherrer Institut (psi46dig). To prevent leakage currents due to thermal runaway, the DUT was wrapped in styrofoam and cooled by an ethanol chiller set to $-15°$ C. At the end of the downstream arm, a second, unirradiated CMS pixel ROC is placed as a timing reference for efficiency measurements.

The DUT is tilted to simulate the Lorentz angle induced by the magnetic field within the CMS detector. The angle was chosen to be close to the angle resulting in optimal charge sharing to maximize the resolution. It is the angle at which an incoming particle always grazes exactly two pixel cells and is given by

$$\tan^{-1} \frac{\text{Pitch}}{\text{Depth}} = \tan^{-1} \frac{100\,\mu\text{m}}{285\,\mu\text{m}} \approx 19.3°. \tag{4.1}$$

The telescope data is aquired using the EUDAQ [79] software framework while the DUT data is aquired using the pxarCore library [80]. Telescope tracks are required to have a hit in all of the six telescope sensor planes. First, individual tracks in the upstream and downstream arm of the telescope are created. The track candidates are then fitted by the General Broken Line (GBL) algorithm [81, 82]. For the particle reconstruction the EUTelescope [83] software is used. The DUT clustering algorithm works by starting with a seed pixel and then adding all pixels that share a border with a pixel already in the cluster until no more pixels to be added are found. The cluster position is calculated by the centre-of-gravity algorithm, where the mass is the pixel charge located at the center of each individual pixel.

The data used for the following analysis was recorded in September 2013 by Armin Burgmeier, Somnath Choudhury, Ganna Dolinska, Ievgen Korol, Daniel Pitzl, Valentina Sola, Simon Spannagel and me. The Test Beam Facility at DESY, where the data was recorded, is a member of the Helmholtz Association (HGF).

4.5 Quality of collected data

After taking a first look at the test beam data, it became apparent that a high number of clusters had an uncharacteristically low cluster charge. In Fig. 4.4 the cluster charge collected with a bias voltage of 220 V, a tilt angle of 19.1°, a pixel threshold of 1.8 ke and a chiller temperature of −15° C is shown. A bump is visible for cluster charges between 2 and 10 ke.

To further investigate this feature, data from clusters with a charge of less than 10 ke is compared to data from clusters with higher charges. In Fig. 4.5 the cluster size of low charge clusters is compared to the cluster size of all clusters. While the mean value for all clusters is around two, low charge clusters peak at a cluster size of one. In Fig. 4.6 the position of all hits across the chip is folded on top of 2x2 pixels array for low charge clusters and all clusters (The Layout of the 2x2 pixel array is the same as seen in the left part of Fig. 4.1). No dependence on hit position on a pixel is observed. This rules out the hypothesis, that the bias dot is the cause of this effect.

Looking at the residual plots for the telescope track and cluster column position (Fig. 4.7), it is visible, that for cluster charges below 10 ke two peaks are visible at around $\approx \pm 70\,\mu$m. This, combined with the average cluster size, is a clear indicator that

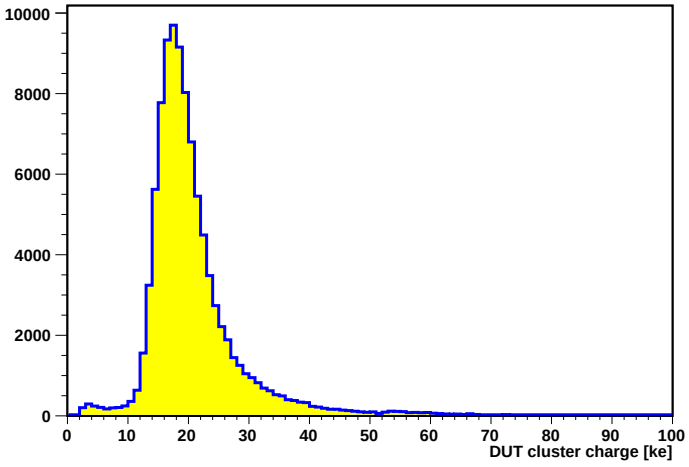

Figure 4.4: Cluster charge collected with a bias voltage of 220 V, a tilt angle of 19.1°, a pixel threshold of 1.8 ke and a chiller temperature of −15° C.

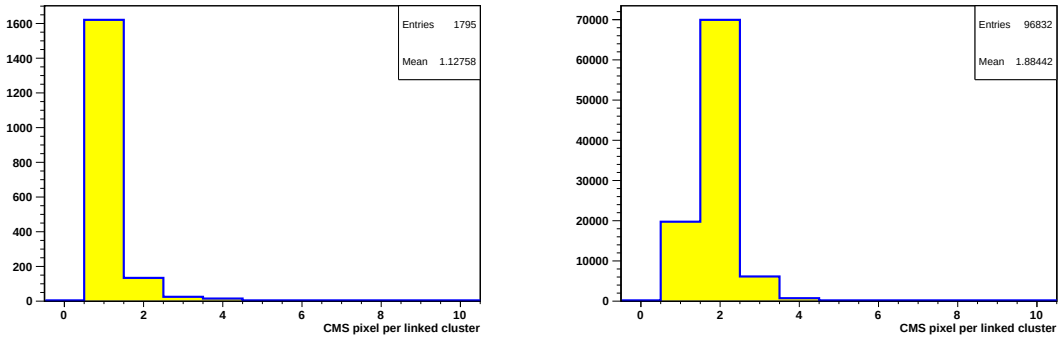

Figure 4.5: Cluster Size for a low charge (left) and all clusters (right).

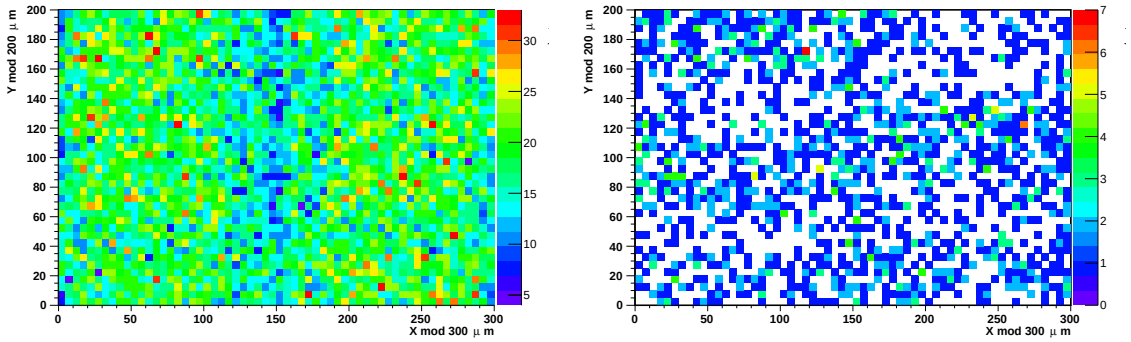

Figure 4.6: Cluster positions across the ROC folded on top of 2x2 pixels for a low charge (left) and all clusters (right). The y-axis gives the position in column direction, while the x-axis gives the position in row direction.

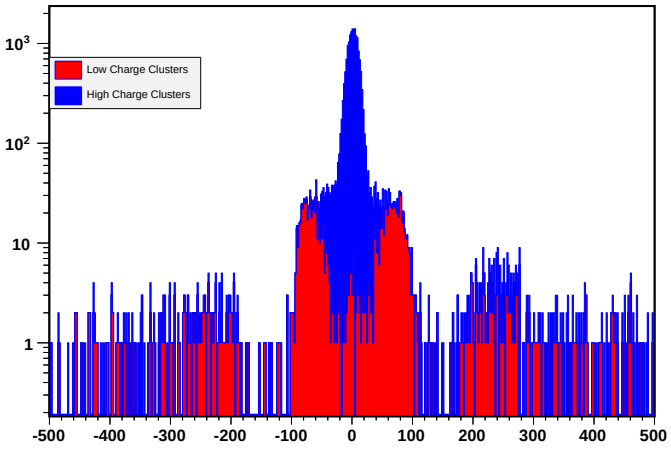

Figure 4.7: Distance between the hit position of a cluster and its associated track for clusters with a charge between 0 and 10 ke (red) and clusters with a charge of more than 10 ke (blue).

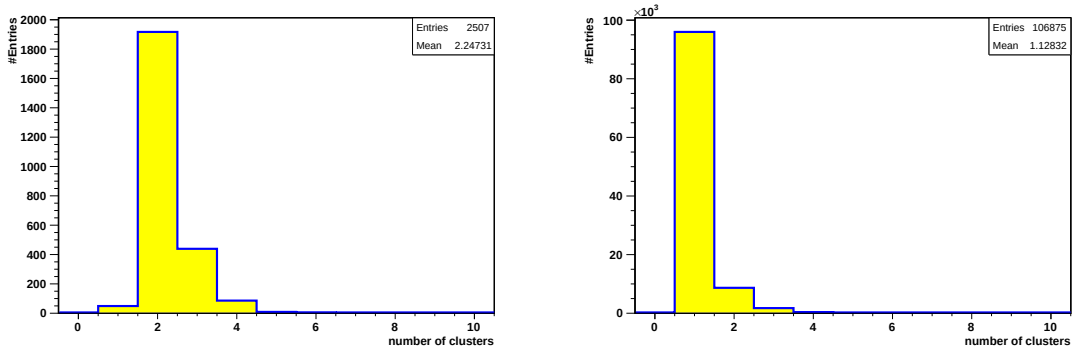

Figure 4.8: Number of clusters per event for events with a Lost Pixel Tag (left) and for events with a cluster linked to a track and no Lost Pixel Tag (right).

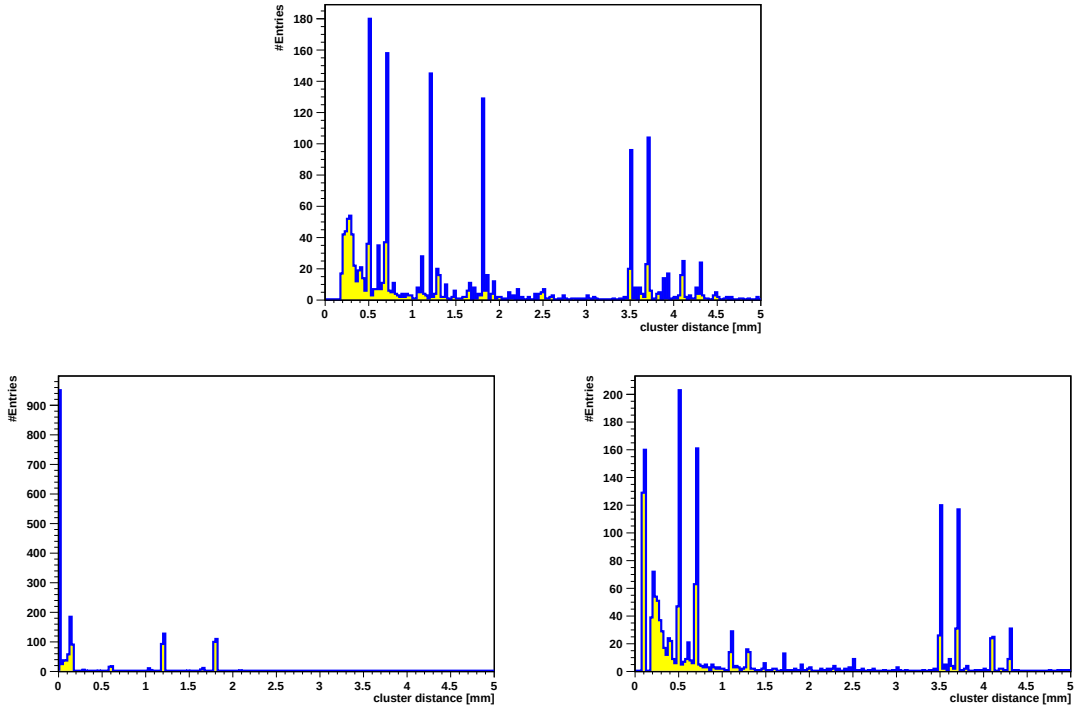

Figure 4.9: Distance (top), column distance (bottom-left) and row distance (bottom-right) between two clusters for events with exactly two clusters and a Lost Pixel Tag.

missing pixels are the cause of the high amount of clusters with a low charge. Events with at least one cluster in the shoulders of the residual distribution ($\Delta Y \geq 40\,\mu$m) that has a cluster size of one are marked with a Lost Pixel Tag. To check if the missing pixel has not been read out or was reconstructed as a separate cluster, the cluster multiplicity is shown for events with and without a Lost Pixel Tag (Fig. 4.8). The mean cluster multiplicity for Events with a Lost Pixel Tag is approximately one higher than for tracks without a Lost Pixel Tag. From this one can conclude that the pixel lost in the cluster reconstruction is read out but is reconstructed as a separate cluster. To better understand the nature of these lost pixel events, the distance, row-distance and

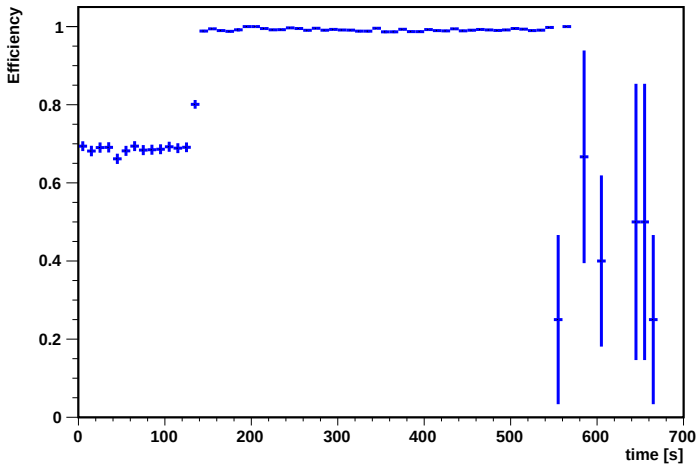

Figure 4.10: Efficiency over time for a telescope run with a bias voltage of 240 V .

column-distance between two clusters is shown for events with exactly two clusters and a Lost Pixel Tag (Fig. 4.9). The very pronounced periodic peaks suggest, that the lost pixel is indeed not missing, but has been read out with an error in the pixel address (bit flip) moving it certain distances away from the neighboring pixel. The row address seems to be the more problematic readout parameter, as the row distance shows peaks that are more pronounced and bigger.
To avoid introducing a bias in the analysis, all events with more than one cluster are excluded instead of excluding events tagged with a lost pixel tag.

Due to difficulties in synchronizing the timing of DUT events and telescope events, the efficiency measurement wasas very difficult. In Fig. 4.10 the development of the measured efficiency over time is shown for a data taking period (telescope run) with a bias voltage of 240 V. Note how the efficiency starts off low at around 70 %, recovers to full efficiency between 120 s- 520 s before falling off to low efficiencies with a very low number of measurements towards the end of the run. The steep falloff at the end of the run can be explained by a phase shift in time between the telescope and DUT events. The telescope clock is strongly coupled to the DESY beam cycle which in turn depends on the power grid frequency. The testboard could not be reconfigured on the fly to shift its clock accordingly. The relatively low efficiency at the beginning of the event however can not be explained by this effect alone, as the events should either be in phase with very high efficiency or not in phase, with no efficiency at all.

In the left plot in Fig.4.11 the efficiency as a function of the telescope track position on the DUT is shown for events in the first 120 seconds of the run. The efficiency is very high in a circular region, mainly located in the lower right quadrant of the chip. The efficiency in the outer regions of the chip is very close to zero. Comparing this to

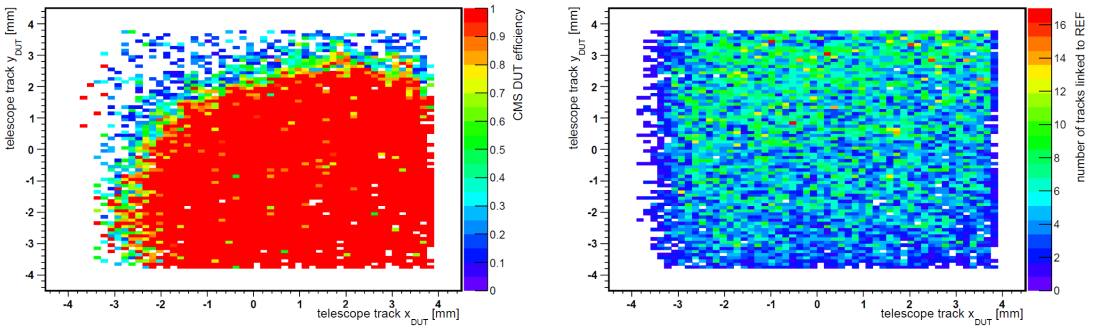

Figure 4.11: Efficiency (left) and number of tracks linked to a cluster in the reference chip (right) as a function of the telescope track position on the DUT for events corresponding to the first 120 seconds of the Efficiency measurement shown in 4.10.

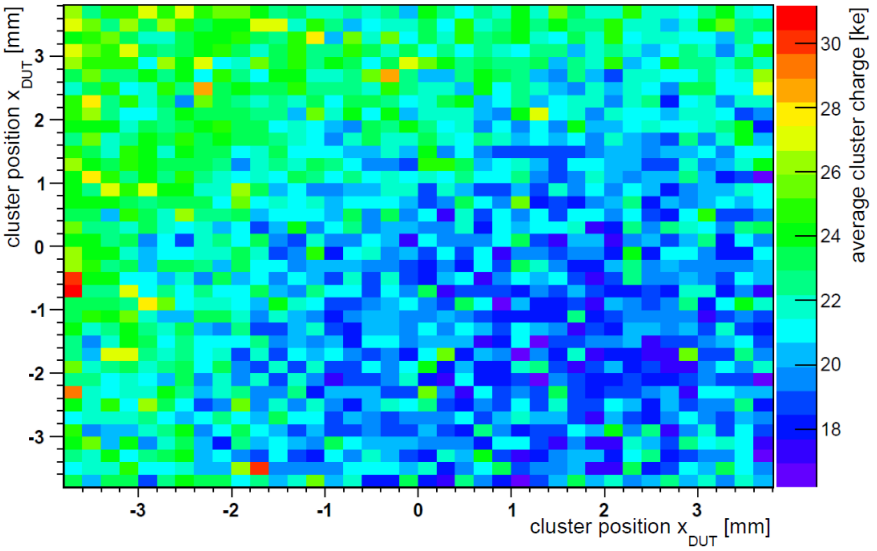

Figure 4.12: Average cluster charge deposition as a function of the cluster position.

the track position on the DUT for tracks with a link to a cluster in the reference chip in the same time period (Fig.4.11, right plot) one can see, that this is not an effect due to the beam profile of the test beam. In Fig.4.12 the average cluster charge deposition is shown as a function of the cluster position on the chip. The region of high efficiency is strongly correlated with a region of lower cluster charges, which is most likely caused by trapping and a non uniform irradiation of the single chip module. This correlation can likely be explained by the time walk effect, which causes pixels with larger amounts of collected charge to pass the pixel threshold sooner than pixels with smaller charge depositions due to different signal rise times. Therefore it is possible, that the different time shift in the region of the chip that received the larger amount of irradiation and collects smaller charges is in phase with the telescope clock, while the remaining part of the DUT is not.

In the following all efficiency numbers were derived by fitting a constant line to the

efficiency within a timing region where no timing synchronization problems were obvious. For this reason all efficiency measurements in this chapter should be understood as a lower limit on the efficiencies that can be reached with the DUT. Furthermore possible time dependent inefficiencies not linked to a problem of synchronization, can not be excluded by the results presented in the following section.

4.6 Analysis of Test beam Data

To test the performance of the irradiated DUT, a bias scan has been analyzed. As the sensor of the DUT is the same sensor that has been used in the pre-phase I CMS pixel detector, the main focus of the studies is not on the sensor itself but on the behavior of the ROC in combination with radiation damage effects. Of special interest are the amount of leakage current the ROC can withstand while still functioning as expected and the read out efficiency for pixels with low charge depositions. The efficiencies shown in the following plots are given by:

$$\text{Efficiency} = \frac{N_{\text{tracksDUT}}}{N_{\text{tracksREF}}}, \tag{4.2}$$

where $N_{\text{tracksREF}}$ is the number of tracks with six telescope hits, passing through the fiducial volume of the DUT with a link to a reference chip cluster and $N_{\text{tracksDUT}}$ is the number of tracks that in addition to all requirements for tracks counted by $N_{\text{tracksREF}}$ have a link to a DUT cluster.
Being able to read out pixels with low collected charges has a significant impact on the resolution of the DUT, which is crucial for reconstructing secondary vertices in the CMS detector. By varying the bias voltage, the depletion depth is varied which makes it possible to observe how the efficiency changes with the amount of charge deposited. During the bias scan, the bias voltage of the single chip module has been varied between 40 and 320 V while the tilt angle was fixed at 19.1°. The pixel threshold was set to 1.8 ke. The electron energy was fixed at 5.6 GeV.

4.7 Bias Scan Results

Fig. 4.13 shows the peak position of a Landau peak fitted to the cluster charge at a bias voltage of 220 V and the Landau peak position as a function of the applied bias voltage. The cluster charge increases with increasing bias voltage until a plateau is reached at around 220 V with a cluster charge of around 18 ke. Until the whole sensor is depleted, the region with charge depletion grows bigger as the applied bias voltage increases. From there on no further increase in cluster charge is observed.
On the left side of Fig. 4.14 the efficiency map across the whole ROC is shown. The right

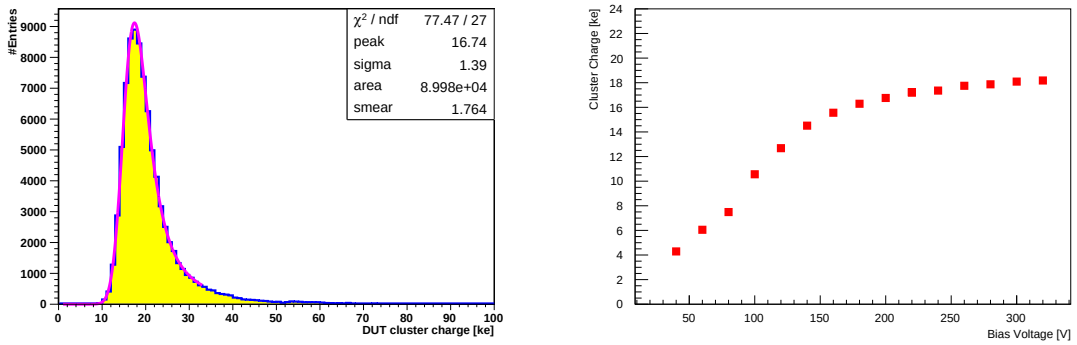

Figure 4.13: Cluster Charge collected with a bias voltage of 220 V with a Landau peak fit (left) and Landau peak position as a function of the applied bias voltage (right).

side of the figure shows the efficiency and the cluster charge divided by the maximum cluster charge reached at full depletion versus the applied bias voltage. As, due to the alignment between the DUT and the REF, there is no overlap with the reference chip on the left side of the efficiency map, the number of entries in that region is low, leading to large statistical errors. No dead pixels and no local effects due to radiation damage are observed on the chip. The efficiency stays above 95% even for bias voltages where only $\approx 25\%$ of the maximum charge at full depletion is collected. This is due to the nature of the electric field in an n-in-n sensor and the n-side readout, as discussed in section 4.2. At full depletion, efficiencies of 99.6% are reached. As the single chip module has been irradiated with the expected lifetime dose of the fourth pixel detector layer, this is a very promising result.

Within the cooling setup, the single chip module was fully operational up to a bias voltage of 320 V, where a leakage current of 50 μA was observed. At higher bias voltages, leakage current made reliable measurements difficult. Note that cooling within the CMS detector might be much better suited to suppress leakage currents, as cooling properties of the setup used for the DUT were not studied and as the DUT chip temperature was not measured during data taking.

The resolution has been measured by fitting a Student's T-function to the residual distribution between the upstream track and the cluster position (Fig. 4.15) and then subtracting the telescope resolution $\sigma_{telescope}$ from the standard deviation σ_{fit} of the fit.

$$\sigma_{measured} = \sqrt{\sigma_{fit}^2 - \sigma_{telescope}^2} \tag{4.3}$$

As expected, the resolution improves with increasing bias voltage until full depletion is reached. The best resolution reached is 7.02 μm, which is slightly worse than the 5μ m reached for an unirradiated chip at a threshold of 1.5 ke [74].

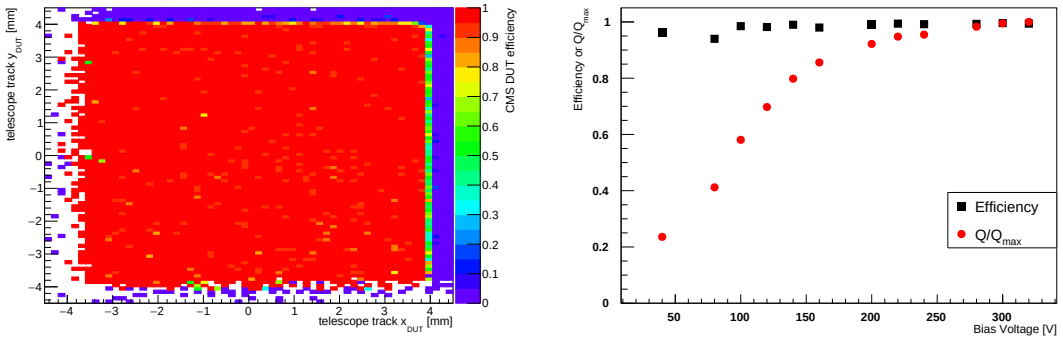

Figure 4.14: Efficiency map across the whole ROC, where one bin corresponds to one pixel (left) and efficiency and fraction of maximum cluster charge as a function of the applied bias voltage (right).

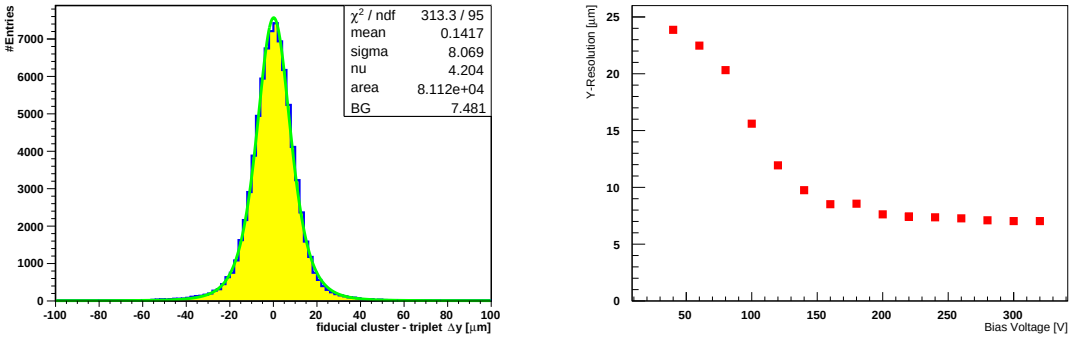

Figure 4.15: Distance between cluster position and a corresponding track at a bias voltage of 320 V (left) and resolution as defined in equation 4.3 as a function of the applied bias voltage (right).

4.8 Summary

After addressing several data quality difficulties that can be attributed to the hardware of the testboard and non-uniform irradiation of the DUT, the results of a bias scan were presented. The chip efficiency stays above 95% for only partially depleted sensors. Due to a synchronization problem, time dependent inefficiencies of the DUT can not be excluded by this test beam analysis. However efficiencies of up to 99.6% were reached for data taking periods at full depletion.

The chip was operational up to bias voltages of 320 V before leakage currents became a problem in our setup where the chip was connected to a chiller set to $-15°$ C.

The resolution at full depletion was measured to be 7.02 μm.

In [84] the results of a test beam measurement of a later and final iteration of the prototype used as a DUT in this chapter is presented. The later iteration of this chip fixed a problem where two neighbouring columns of pixels would sometimes not respond over extended periods of time. For this unirradiated chip a row resolution of 4.8μ m was reached which is only slightly better than the 7.02 μm measured for the irradiated

DUT in this testbeam campaign. This result is promising for the future operation of the new ROC, which will be used in the second to fourth layer of the pixel detector after the phase I upgrade. However, as the ROC used in this analysis differs from the ROC that will finally be implemented during the phase I upgrade, further beam tests of an irradiated module with a final iteration of the ROC will be carried out.

Chapter 5

Kinematic Fitting Tool for Heavy Higgs Boson Decays

In the following chapter a dedicated kinematic fit for H→hh→bb$\tau\tau$ searches (HHKinFit) will be presented. This tool was developed in collaboration with Benedikt Vormwald and Peter Schleper [85]. The analysis shown in this thesis in Chapter 6 will make heavy use of this tool.
After a short general introduction to kinematic fitting, the use of the kinematic fit will be motivated and explained in detail. Finally, results of Monte Carlo studies on the performance and reliability of the fit are presented.

5.1 Principles of kinematic fits

In high energy physics, the reconstruction of promptly decaying particles can be very difficult, as they can only be measured by recombining all of their decay products, each with its own measurement uncertainties. Furthermore, in many decays the presence of neutrinos in the decay products complicate reconstructing the Lorentz vectors of the mother particles further. Especially for decays with well defined kinematic constraints, kinematic fits can help to improve the resolution of directly and indirectly measured observables and help in separating signal from background events.
A kinematic fit varies the observables measured in an event, while simultaneously fulfilling a number of kinematic constraints for the signal topology. In the fitting procedure a χ^2 function is minimized. The χ^2 function is a measure for how much the fitted observables deviate from the measured observables with respect to their uncertainties. For a set of observables $\vec{X}_{\text{observed}}$ with Gaussian uncertainties and correlations described by a covariance matrix COV, the χ^2 contribution of fit parameters $\vec{X}_{\text{fit}}$ is given by

$$\chi^2_X = \left(\vec{X}_{\text{fit}} - \vec{X}_{\text{observed}}\right)^T COV_X^{-1} \left(\vec{X}_{\text{fit}} - \vec{X}_{\text{observed}}\right). \tag{5.1}$$

In the 1-dimensional case with a Gaussian uncertainty of σ_X this simplifies to

$$\chi^2_X = \left(\frac{X_{\text{fit}} - X_{\text{observed}}}{\sigma_X} \right)^2 . \tag{5.2}$$

The number of degrees of freedom of the fit can be reduced by enforcing the kinematic constraints of the event topology. This is usually done by the method of Lagrange multipliers. The χ^2 functions is then minimized with respect to $\vec{X}_{\text{fit}}$. The minimized χ^2 value can be translated into a fit probability

$$P(\chi^2_{\text{observed}}) = \int_{\chi^2_{\text{observed}}}^{\infty} PDF(\chi^2, ndf) d\chi^2 \tag{5.3}$$

where $PDF(\chi^2, ndf)$ is the theoretical χ^2 probability density function for a fit with *ndf* degrees of freedom. For correctly described Gaussian uncertainties the fit probability distribution for signal events should be flat. The fit probability can be used as a variable for separating signal from background events, as the signal should naturally deviate less than background events from the given kinematic constraints and thus feature a smaller minimal χ^2 and larger fit probability. For signal events, the resolution of the fitted observables is improved after the fit.

5.2 Kinematic Fit for Heavy Higgs Boson Events

Using a kinematic fit for H→hh→bb$\tau\tau$ searches is a sound analysis strategy for several reasons. Foremost, the signal topology obeys some kinematic constraints that can be used to simplify the fitting procedure by reducing the number of degrees of freedom of the fit. Furthermore, the constraints are an important handle for the fit to reduce the measurement uncertainties on the observables or to reconstruct unmeasured particles like neutrinos. The neutrinos in the final state due to the tau decays are another good argument for using a kinematic fit, as they make a proper mass reconstruction for the heavy Higgs boson very difficult. Lastly, the background from $t\bar{t}$ processes is the major background process for the heavy Higgs search presented in Chapter 6. The background could be decreased with a cut on the minimized χ^2-values, as $t\bar{t}$ events, in general, do not confirm to the kinematic constraint of the signal topology and should therefore tend to have larger χ^2-values than signal events.

In Fig. 5.1 a sketch of heavy Higgs boson decay in the transversal detector plane is shown. The invariant masses of the tau lepton pair and the b-jet pair are equal to the

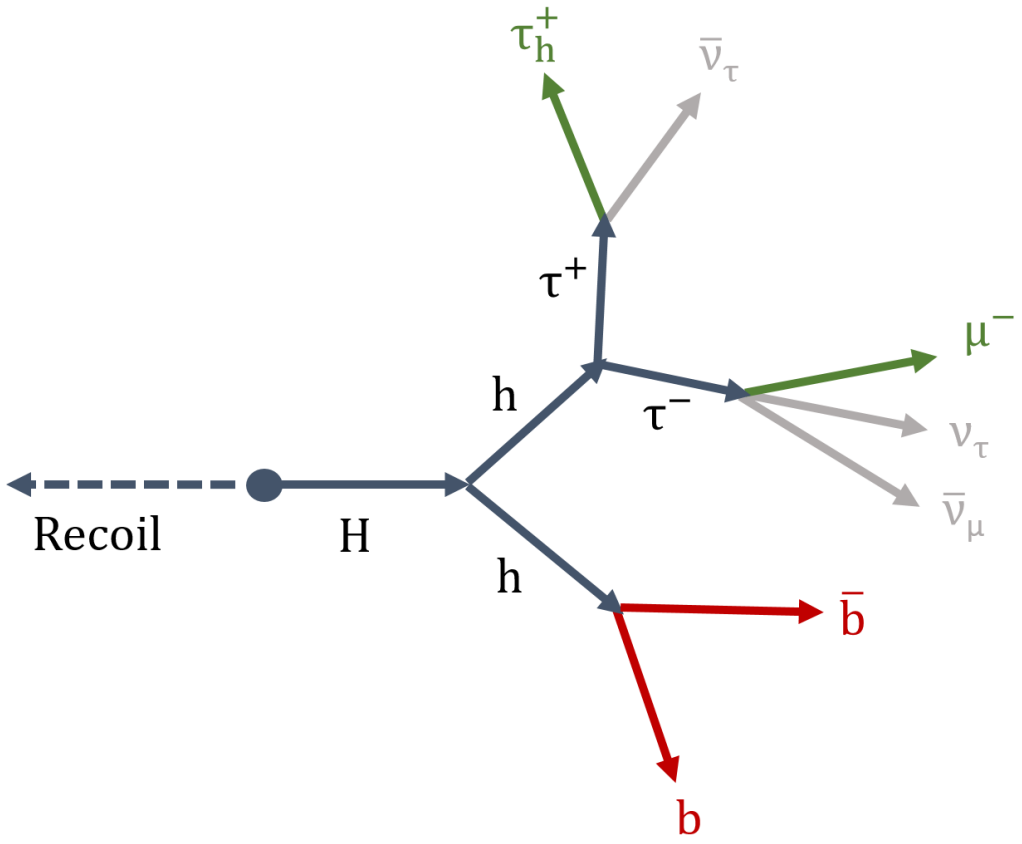

Figure 5.1: Sketch of Heavy Higgs boson decay into two b-jets and two tau leptons in the transversal detector plane.

Higgs boson mass.

$$M(b_1 + b_2) = m_h \tag{5.4}$$

$$M(\tau_1 + \tau_2) = m_h \tag{5.5}$$

As the mass difference between a Higgs boson and a tau is quite large, the taus willin general have a high Lorentz boost. The momentum vector of the visible tau decay products will therefore approximately point in the same direction as the momentum vectors of the original taus (collinear approximation). To a lesser extent, the same should be true for the momentum vectors of the measured b-jets with respect to the true b-partons. How well this collinear approximation is motivated was tested on a MC sample by comparing the minimal distance ΔR between a tau on generator level and the visible decay products for a tau decaying into an electron, a muon or hadronically where the visible decay product of the tau has a transverse momentum of $p_T > 20\,\text{GeV}$. The same was done for b-partons on generator level before any hadronisation or final state irradiation occurs and the reconstructed jets with a transverse momentum of $p_T > 20\,\text{GeV}$ closest in ΔR. As can be seen in Fig. 5.2 the vast majority of taus/b-jets are reconstructed

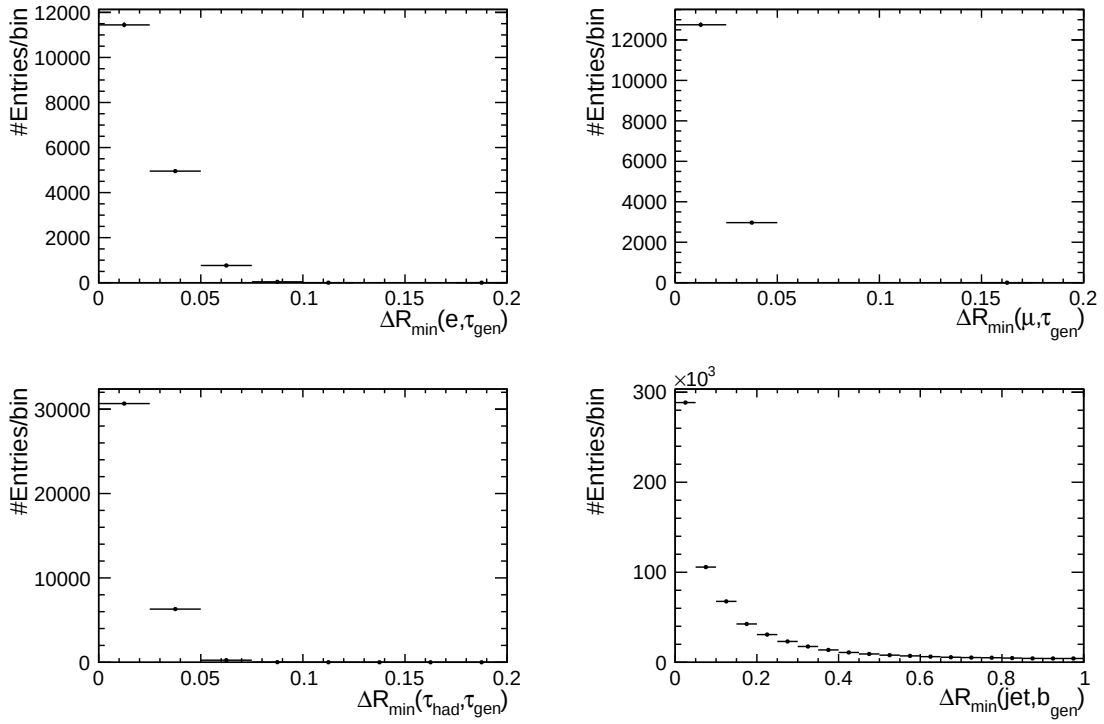

Figure 5.2: Minimal distance ΔR between a tau on generator level and it's visible decay products for a tau decaying into an electron (top-left), a muon (top-right) or hadronically (bottom-left) for a H→hh→bb$\tau\tau$ event with $m_H = 300\,\text{GeV}$. In the plot on the bottom-right the same is shown for b-jets on generator level and a reconstructed jet.

very close to their respective generator particle, justifying the assumption of collinearity for this fit.

Due to the collinear approximation for the tau leptons and the well motivated assumption that the b-parton direction is well measured by the measured jet direction, the directions of the four-vectors of the two taus and the two b-jets are fixed during the fit and only the four energies remain as free fit parameters. Due to the invariant mass constraint of the tau lepton pair and b-jet pair given by Eq. 5.4 and Eq. 5.5, the energies of the two tau leptons/b-jets are strictly related to each other, leaving only two free parameters, namely the energy of one of the tau leptons and the energy of one of the b-jets in the following named E_{τ_1} and E_{b_1}.

To set the energy of the second b-jet during the fitting process, the following approach is used. As any mismeasurement of the jet energy proportionally also affects the measured momentum, the ratio $\frac{\vec{p}}{E} = \vec{\beta}$ can be assumed to be very well measured and thus constant to first approximation and is derived from the pre-fit kinematics:

$$\vec{\beta}_{b1} = \frac{\vec{p}_{b1,\text{observed}}}{E_{b1,\text{observed}}} \tag{5.6}$$

$$\vec{\beta}_{b2} = \frac{\vec{p}_{b2,\text{observed}}}{E_{b2,\text{observed}}} \tag{5.7}$$

The energy of the second b-jet can be calculated from the invariant mass constraint:

$$m_h^2 = p_{b1}^2 + p_{b2}^2 + 2p_{b1}p_{b2} \tag{5.8}$$

$$= (1-\vec{\beta}_{b1}^2)E_{b1}^2 + E_{b2}^2(1-\vec{\beta}_{b2}^2) + 2E_{b1}E_{b2}(1-\vec{\beta}_{b1}\vec{\beta}_{b2}) \tag{5.9}$$

$$\Rightarrow\ E_{b2}(E_{b1}) = -\frac{E_{b1}(1-\vec{\beta}_{b1}\vec{\beta}_{b2})}{1-\vec{\beta}_{b2}^2} + \sqrt{\left(\frac{E_{b1}(1-\vec{\beta}_{b1}\vec{\beta}_{b2})}{1-\vec{\beta}_{b2}^2}\right)^2 + \frac{m_h^2-(1-\vec{\beta}_{b1}^2)E_{b1}^2}{1-\vec{\beta}_{b2}^2}} \tag{5.10}$$

When changing b-jet energies, the magnitude of the jet momentum is scaled proportionally, leaving $\vec{\beta}$ unchanged:

$$\vec{p}_{\mathrm{b,new}} = \vec{\beta}\cdot E_{\mathrm{b,new}}. \tag{5.11}$$

The energy of the second tau is calculated in a similar fashion. As the mass of the tau is known and constant, the invariant mass constraint can be written as

$$m_h^2 = p_{\tau1}^2 + p_{\tau2}^2 + 2p_{\tau1}p_{\tau2} \tag{5.12}$$

$$= 2m_\tau^2 + 2(E_{\tau1}E_{\tau2} - |\vec{p}_{\tau1}||\vec{p}_{\tau2}|\cos\alpha). \tag{5.13}$$

This equation can then be solved for $E_{\tau2}$ using $|\vec{p}_{\tau2}|^2 = E_{\tau2}^2 - m_\tau^2$:

$$|\vec{p}_{\tau2}| = E_{\tau2}\underbrace{\frac{E_{\tau1}}{|\vec{p}_{\tau1}|\cos\alpha}}_{D} - \underbrace{\frac{m_h^2-2m_\tau^2}{2|\vec{p}_{\tau1}|\cos\alpha}}_{F} \tag{5.14}$$

$$0 = E_{\tau2}^2 - E_{\tau2}\frac{2DF}{D^2-1} + \frac{F^2+m_\tau^2}{D^2-1} \tag{5.15}$$

$$E_{\tau2} = \begin{cases} \frac{1}{D^2-1}(DF + \sqrt{m_\tau^2(1-D^2)+F^2}) & \text{if } \cos\alpha > 0 \\ \frac{1}{D^2-1}(DF - \sqrt{m_\tau^2(1-D^2)+F^2}) & \text{if } \cos\alpha < 0 \end{cases} \tag{5.16}$$

The energy of a visible tau decay product is in general smaller than the energy of the tau. This can be used in the fit by introducing a lower limit on the energy of the fitted tau vectors. This limit could slightly improve the resolution of the fitted objects for signal events as it might prevent the fit from finding a minimum for a tau lepton energy below the energy of the visible tau lepton decay product which is physically not well motivated. As the energy of hadronic tau decay products has a Gaussian measurement uncertainty of up to 5%, depending on the decay mode, and visible energy fractions close to unity are possible, the lower limit on the energy of the fitted tau vectors is loosened to 90% of the energy of the measured visible tau decay products. A very soft limit on the energies of the fitted b-jets of $E_\mathrm{b} > 5\,\mathrm{GeV}$ is introduced to avoid numerical fringe cases.

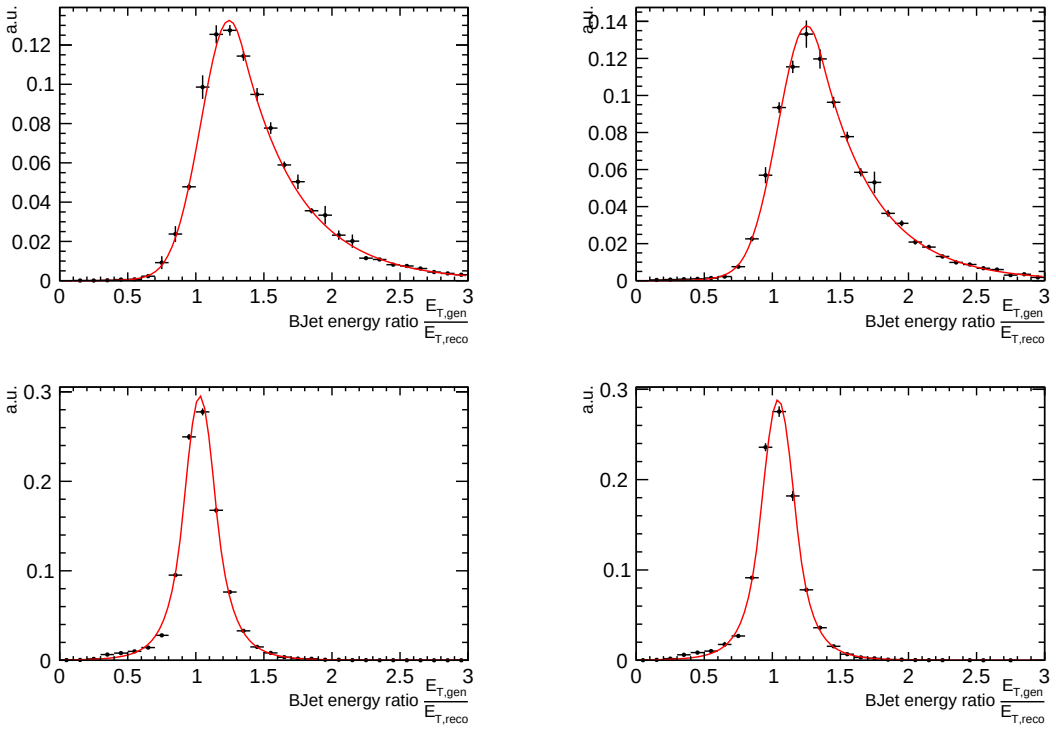

Figure 5.3: Transverse b-jet-energy ratio $\frac{E_{\mathrm{T,gen}}}{E_{\mathrm{T,reco}}}$ fitted by a two-tailed crystal-ball function (Eq. 5.18) shown in red on a signal sample with a heavy Higgs boson mass of 300 GeV for several $E_{\mathrm{T,reco}}$ and $|\eta|$ bins.

- Top-left: $25\,\mathrm{GeV} < E_{\mathrm{T,reco}} < 30\,\mathrm{GeV}$ and $|\eta| < 1.2$
- Top-right: $25\,\mathrm{GeV} < E_{\mathrm{T,reco}} < 30\,\mathrm{GeV}$ and $|\eta| \geq 1.2$
- Bottom-left: $80\,\mathrm{GeV} < E_{\mathrm{T,reco}} < 120\,\mathrm{GeV}$ and $|\eta| < 1.2$
- Bottom-right: $80\,\mathrm{GeV} < E_{\mathrm{T,reco}} < 120\,\mathrm{GeV}$ and $|\eta| \geq 1.2$

5.3 χ^2-Function

The χ^2-function serves as a measure for how far the fitted event deviates from the measured event given the respective uncertainties of the observables. The χ^2 depends on the fitted values of E_{τ_1} and E_{b_1}. It will be minimized during the fitting procedure. The χ^2-function is the sum of three individual contributions from the two b-jets and the balance of the heavy Higgs boson p_T against the recoil.

$$\chi^2 = \chi^2_{\mathrm{b}_1} + \chi^2_{\mathrm{b}_2} + \chi^2_{\mathrm{recoil}}, \tag{5.17}$$

where each of the three contributions is of the form given by Eq. 5.1, when assuming gaussian errors. However, as will be presented in the next section, this assumption is not well motivated for the b-jet contributions and an alternative approach will be introduced.

5.3.1 B-jet χ^2 contribution

Given a Gaussian uncertainty, the χ^2 contributions of an measured observables X can be written as in Eq. 5.2. For the 8 TeV heavy Higgs boson analysis [1], this approach is used by the HHKinFit to calculate the χ^2 contributions of the b-jets. However, as the performance of the fit was studied, a peak at low fit probabilities was observed, which can be attributed to this approximation of the b-jet uncertainties. To alleviate this shortcoming of the fit and to increase the potential separation power of the fit probability from background events, the b-jet uncertainties were studied on a signal MC in dependence of $|\eta|$ and their transverse energy E_T. Fig. 5.3 shows the b-jet-energy ratio $\frac{E_{\mathrm{T,gen}}}{E_{\mathrm{T,reco}}}$ on a signal sample with a heavy Higgs boson mass of 300 GeV for several E_{T} and $|\eta|$ bins. The events are seperate into two $|\eta|$ bins: $|\eta| < 1.2$ and $|\eta \geq 1.2$. The upper bin edges for the binning in $E_{T,reco}$ are chosen to be 25, 30, 40, 50, 60, 80, 120 and 500. The complete set of plots for all E_T and $|\eta|$ bins can be found in Appendix A.1. Note that the generated transverse energy $E_{\mathrm{T,gen}}$ does not refer to the generated jet but to the energy of the b-parton before final state radiation. This is done as the exact invariant mass constraint for the b quarks within the kinematic fit means that the b-parton energy is the target energy the fits tries to reconstruct and, therefore, the uncertainty has to be determined with respect to this value as well.
As can be seen in Fig. 5.3 the uncertainty does indeed not have a Gaussian shape. b-jets can decay to lighter quark flavors via a $W^{\pm}$-boson, leading to neutrinos within the jets. These neutrinos and final state radiation can lead to energy that is not reconstructed within the jet cone, resulting in a long tail and a shift of the peak to values slightly larger than one in the shown distributions. The relative strength of the effect is stronger for smaller values of E_{T}. To obtain the probability density function (PDF) of the distribution, it is normalized to one and approximated by a two-tailed crystal-ball function of the form

$$\mathrm{Cryst}(x) = \begin{cases} e^{-0.5|\alpha|^2} \cdot \left(\frac{\frac{n}{|\alpha|}}{\frac{n}{|\alpha|} - |\alpha| - \frac{x-\bar{x}}{\sigma}}\right)^n & \text{if } \frac{x-\bar{x}}{\sigma} < |\alpha| \\ e^{-0.5(\frac{x-\bar{x}}{\sigma})^2} & \text{if } |\alpha| < \frac{x-\bar{x}}{\sigma} < |\beta| \\ e^{-0.5|\beta|^2} \cdot \left(\frac{\frac{n}{|\beta|}}{\frac{n}{|\beta|} - |\beta| + \frac{x-\bar{x}}{\sigma}}\right)^n & \text{if } |\beta| < \frac{x-\bar{x}}{\sigma} \end{cases} \tag{5.18}$$

with free fit parameters σ, $\bar{x}$, n, α and β. The fitted PDFs are shown in Fig. 5.3 as a red line. This function can be used to calculate the probability for a fitted transverse Energy $E_{T,fit}$ given a measured value $E_{\mathrm{T,reco}}$.
The cumulative distribution function(CDF), is the integral of the derived PDF. To obtain the corresponding χ^2 values, it is mapped to the Gaussian CDF by equating them:

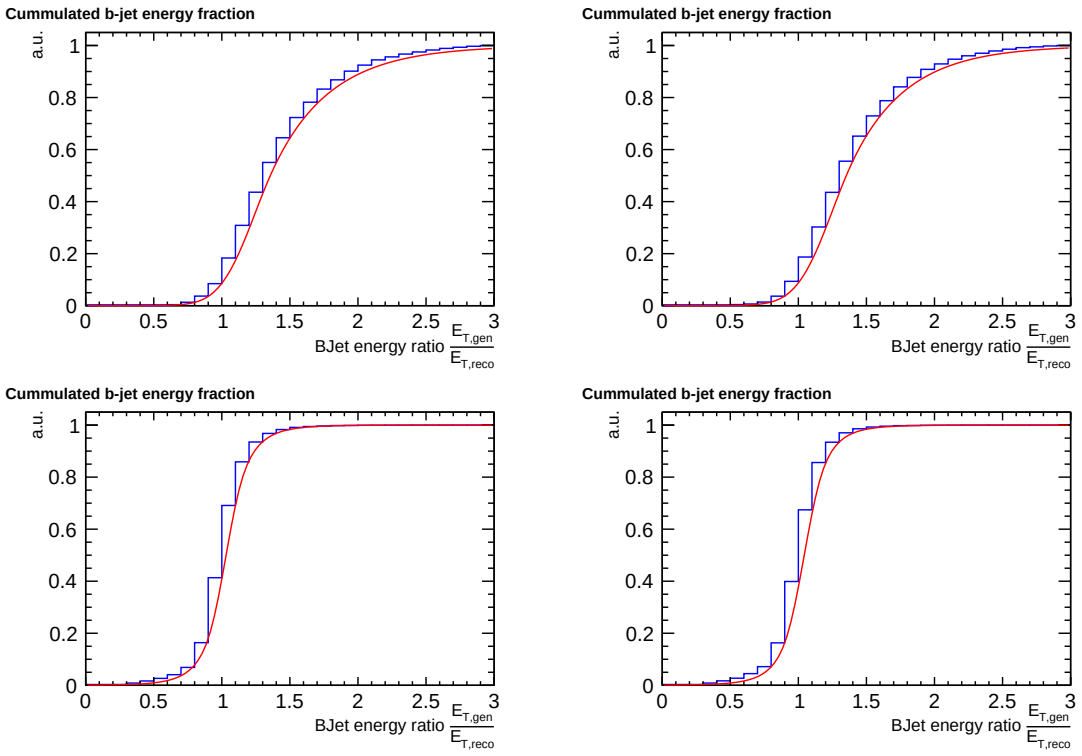

Figure 5.4: Cumulative distribution functions (CDF) corresponding to the probability density functions (PDF) shown in Fig. 5.3. The red line is the integral of the fitted two-tailed crystal-ball function.

- Top-left: $25\,\text{GeV} < E_{\text{T,reco}} < 30\,\text{GeV}$ and $|\eta| < 1.2$
- Top-right: $25\,\text{GeV} < E_{\text{T,reco}} < 30\,\text{GeV}$ and $|\eta| \geq 1.2$
- Bottom-left: $80\,\text{GeV} < E_{\text{T,reco}} < 120\,\text{GeV}$ and $|\eta| < 1.2$
- Bottom-right: $80\,\text{GeV} < E_{\text{T,reco}} < 120\,\text{GeV}$ and $|\eta| \geq 1.2$

$$CDF_{Gauss} = \frac{1}{2}(1 + erf(\frac{\chi}{\sqrt{2}}) = CDF_{Cryst} \tag{5.19}$$

$$\chi^2(\frac{E_{\text{T,fit}}}{E_{\text{T,reco}}}) = 2erf^{-1}(2CDF_{\text{Cryst}}(\frac{E_{\text{T,fit}}}{E_{\text{T,reco}}}) - 1)^2. \tag{5.20}$$

The CDFs and χ^2 functions corresponding to the PDFs shown in Fig. 5.3 are shown in Fig. 5.4 and Fig. 5.5 respectively. Note that especially in regions of low E_T, the minimum of the χ^2-function is at an energy fraction considerably larger than one and the slope towards higher energy ratios is much gentler than towards lower energy ratios. This is in agreement with the observation that reconstructed jet energies are smaller than the true b-parton energies which the kinematic fit aims so reconstruct.

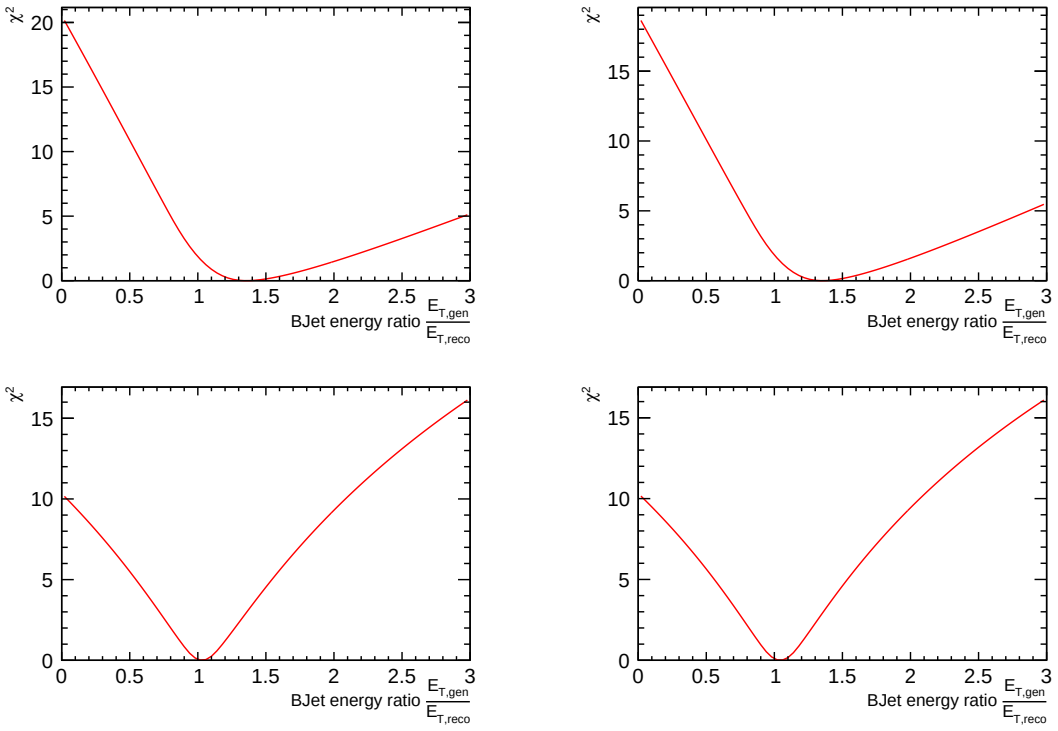

Figure 5.5: χ^2 functions corresponding to the cumulative distribution functions (CDF) shown in Fig. 5.4. The χ^2 functions were calculated according to 5.20.

- Top-left: $25\,\text{GeV} < E_{\text{T,reco}} < 30\,\text{GeV}$ and $|\eta| < 1.2$
- Top-right: $25\,\text{GeV} < E_{\text{T,reco}} < 30\,\text{GeV}$ and $|\eta| \geq 1.2$
- Bottom-left: $80\,\text{GeV} < E_{\text{T,reco}} < 120\,\text{GeV}$ and $|\eta| < 1.2$
- Bottom-right: $80\,\text{GeV} < E_{\text{T,reco}} < 120\,\text{GeV}$ and $|\eta| \geq 1.2$

5.3.2 Balance χ^2 contribution

The transversal momentum of the heavy Higgs boson recoil can be reconstructed by summing the transverse momentum components of all heavy Higgs boson decay products, using the $\vec{E}_{T,miss}$ as an indicator for the transverse neutrino momenta:

$$-\vec{p}_{T,recoil} = \vec{p}_{\text{T,b1}} + \vec{p}_{\text{T,b2}} + \vec{p}_{T,\tau 1_{\text{vis}}} + \vec{p}_{T,\tau 2_{\text{vis}}} + \vec{E}_{\text{T,miss}} \tag{5.21}$$

The χ^2 contribution for the fitted $\vec{p}_{T,recoil}$ is given by the deviation of the fitted from the measured $\vec{p}_{T,recoil}$ with respect to the uncertainty of the $\vec{p}_{T,recoil}$ measurement. As the uncertainties for the x and y component of the $\vec{p}_{T,recoil}$ are correlated, the following matrix equation is used:

$$\chi^2_{recoil} = (\vec{p}^{\,\text{measured}}_{\text{T,recoil}} - \vec{p}^{\,fit}_{T,recoil}) \cdot COV^{-1}_{recoil} \cdot (\vec{p}^{\,measured}_{\text{T},recoil} - \vec{p}^{\,fit}_{\text{T},recoil}) \tag{5.22}$$

For a straightforward $\vec{E}_{T,miss}$ algorithm in which the $\vec{E}_{T,miss}$ is the negative sum

of all measured transverse momenta the recoil covariance matrix would be given by subtracting the covariance matrices of the jets and visible tau-decay products from the $\vec{E}_{T,miss}$ covariance matrix. However, as the $\vec{E}_{T,miss}$ algorithm used during the remainder of this thesis uses an multivariate analysis (MVA) based approach, deriving the $\vec{E}_{T,miss}$ covariance matrix has proven more difficult. As an approximation, the $\vec{E}_{T,miss}$ covariance matrix is used as the recoil covariance matrix

$$COV_{recoil} = COV_{\vec{E}_{T,miss}}. \tag{5.23}$$

This approximation was chosen as it simplifies the algorithm greatly and the uncertainties of the $\vec{E}_{T,miss}$ should be significantly larger than the contributions from the jets and taus. Although this might seem like a rough approximation, the performance study shown in Section 5.5 justifies this approximation.

5.3.3 Minimization of the χ^2 function

The minimization of the $\chi^2(E_{\tau_1}, E_{b_1})$-function is done by alternating between a line search and the Newton Method. Starting with a line search, a minimum is found along a 1-dimensional line in the E_{τ_1}- E_{b_1} parameter space. First the algorithm looks for three points x_1, x_2 and x_3 along the line, which fulfill the properties $x_1 > x_2 > x_3$, $\chi^2(x_1) > \chi^2(x_2)$ and $\chi^2(x_3) > \chi^2(x_2)$. If the properties are fulfilled, the points x_1 and x_3 enclose a local minimum. The minimum can then be found by the golden section search, a particularly effective method of dividing the interval.
After a local minimum was found by the line search, a new search direction is chosen by Newton's method for two dimension. Newton's method assumes that the change of the χ^2-function in the close vicinity of the previously found minimum can be described by a quadratic equation and chooses the next search-direction as the direction in which the minimum of this assumed function would be. The Hesse matrix and gradient of the χ^2-function are approximated by sampling values in the close proximity of the minimum found by the line search. If the Hesse matrix is invertible, the next direction for the line search is given by the direction in which the minimum of the assumedly quadratic χ^2-function can be found. Otherwise, the next line search direction is chosen as the direction of steepest descent, given by the gradient.

5.4 Performance on Toy MC Signal Samples

To test the performance of the kinematic fit, it is tested on a signal MC sample without detector simulation but with uncertainties introduced by hand (toy MC). Before uncertainties are introduced, the two b-partons of the events are required to have a transverse momentum of $p_T > 20\,\text{GeV}$ and both tau leptons are required to decay leptonically with

convergence code	definition	event ratio
-2	no solution for di-jet system within given constraints	0.0%
-1	no solution for di-tau system within given constraints	0.0%
0	no minimum found during the fitting process	0.0%
1	fit converged	96.8%
2	fit converged at a limit of the di-jet system	0.0%
3	fit converged at a limit of the di-tau system	3.2%
4	fit converged at a limit of the di-jet and di-tau system	0.0%

Table 5.1: Definition of convergence codes of the kinematic fit and ratio of events for each code for toy MC events generated from a MC sample with a heavy Higgs boson mass of 300 GeV.

a visible transverse momentum of $p_T > 5\,\text{GeV}$.

For the b-partons an uncertainty is introduced by changing the generated transverse b-parton energy. A random number generator produces random numbers based on the PDF for b-jets with a transverse energy of $25\,\text{GeV} < E_{\text{T,reco}} < 30\,\text{GeV}$ and a pseudorapidity of $|\eta| < 1.2$, shown in 5.3. The random numbers are then used as an inverse scale for the transverse b-parton energy. The transverse momentum of the $\vec{p}_{T,recoil}$ is reconstructed by negating the true heavy Higgs boson transverse momentum. A Gaussian uncertainty is then introduced for the x and y component of the $\vec{p}_{T,recoil}$ in a similar fashion. The Gaussian used for the random number generator has a width of 20 GeV. Accordingly the recoil covariance matrix is given by

$$COV_{\vec{p}_{T,recoil}} = \begin{pmatrix} 400 & 0 \\ 0 & 400 \end{pmatrix} \text{GeV}^2. \tag{5.24}$$

As the energies of the visible tau-decay products are not used in the fit, they are not smeared. For technical reasons, only events with leptonically decaying tau leptons have been used. The heavy Higgs boson mass of the used signal sample is 300 GeV.

The convergence code is a technical observable of the fitting process that indicates if there were any problems or peculiarities during the fitting process. In Table 5.1 the meaning of all convergence codes and the ratio of events for each code for toy MC events generated from a MC sample with a heavy Higgs boson mass of 300 GeV is listed. The vast majority of events converges at a point that is not close to one of the limits (convergence code 1). There are some events where the minimum was found at one of the tau lepton constraints (convergence code 3). This can happen if the energy of the visible tau decay product is close to the tau lepton energy and the jet energies are shifted in such a way, that the jet configuration that gives the smallest $\chi^2_{\text{b}_1/2}$ terms differs significantly in the recoil contribution with respect to the true contribution of the unshifted jets.

Fig. 5.6 shows the Distribution of minimal χ^2 values found by the kinematic fit and

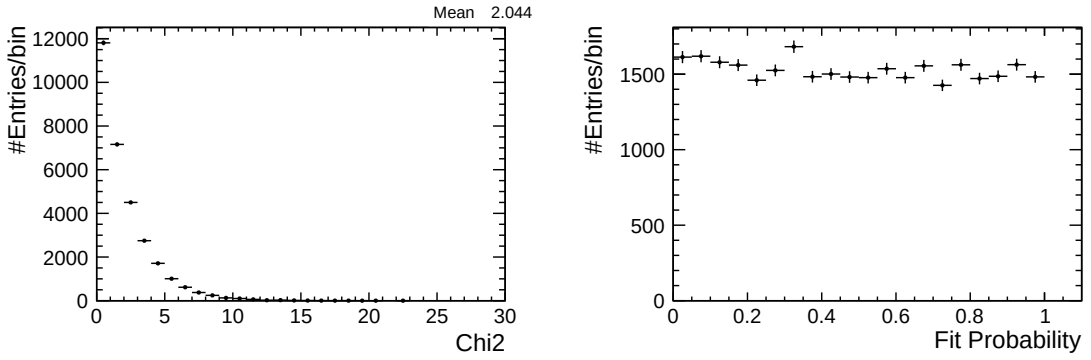

Figure 5.6: Distribution of minimal χ^2 value found by the kinematic fit (left) and fit probability calculated with the theoretical χ^2 probability density function for two degrees of freedom (right). The events are toy MC events generated from a MC sample with a heavy Higgs boson mass of 300 GeV.

the corresponding fit probability distribution. The minimal χ^2 peaks at very low values, falls of quickly and has a mean of approximately 2, as one would expect for a fit with two degrees of freedom. The fit probability was calculated with the theoretical χ^2 probability density function for two degrees of freedom as given by Eq. 5.3.

For correctly described Gaussian uncertainties or, as in the case of the b-jet uncertainty treatment, uncertainties that have been mapped to Gaussian probabilities, this distribution should be flat. As can be seen in the left part of Fig. 5.6 this is very much the case for the uncertainties described within our toy MC. To demonstrate the effect of the kinematic fit on the energies of the fitted objects, the energy of the visible tau-decay products and the b-jet resolution before and the energy resolutions after the fit are shown in Fig. 5.7 for the taus and Fig. 5.8 for the b-jets. In Fig. 5.7 the red lines depict the visible energy fractions $\frac{E_{vis}}{E_{gen}}$ whereas the black line depicts the reconstructed tau energy fraction $\frac{E_{fit}}{E_{gen}}$. The visible energy fraction is always smaller than the energy of the tau lepton. Therefore the red line is shifted towards zero. There are no entries above an energy fraction of 1 as no uncertainty was introduced for the visible tau-decay product energies. After the fit, the fitted tau energy is reconstructed quite precisely. As the distributions are approximately symmetric and peak at an energy fraction of 1, no bias is introduced by the fit.

Fig. 5.8 shows a similar plot for the b-jets. Here the red line shows the jet response $\frac{E_{gen}}{E_{reco}}$ after uncertainties have been introduced while the black line shows the b-jet energy resolution $\frac{E_{fit}}{E_{gen}}$ after the fit. Note that E_{gen} is not the energy of the generator jet but the energy of the generator b-parton before any final state radiation or hadronisation occurs. The red line has the same shape as the derived energy ratio $\frac{E_{gen}}{E_{reco}}$ shown in Chapter 5.3 for jets with $\eta < 1.2$ and $25\,\text{GeV} < E_T < 30\,\text{GeV}$. This is a good cross check to confirm that the uncertainties were introduced as intended. The black line shows the reconstructed b-jet-energy resolution after the fit $\frac{E_{fit}}{E_{gen}}$. It is clearly visible

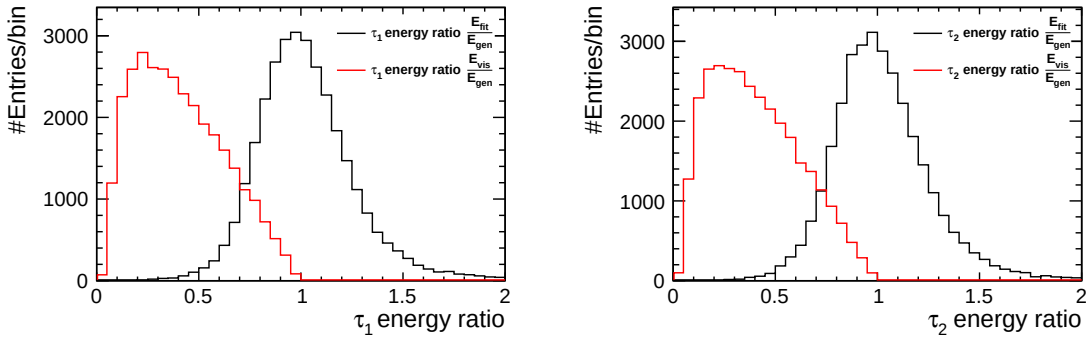

Figure 5.7: Effect of the kinematic fit on the energies of τ_1 (left) and τ_2 (right). Shown in red are the visible energy fractions $\frac{E_{vis}}{E_{gen}}$. In black the reconstructed tau energy fraction $\frac{E_{fit}}{E_{gen}}$ is shown.

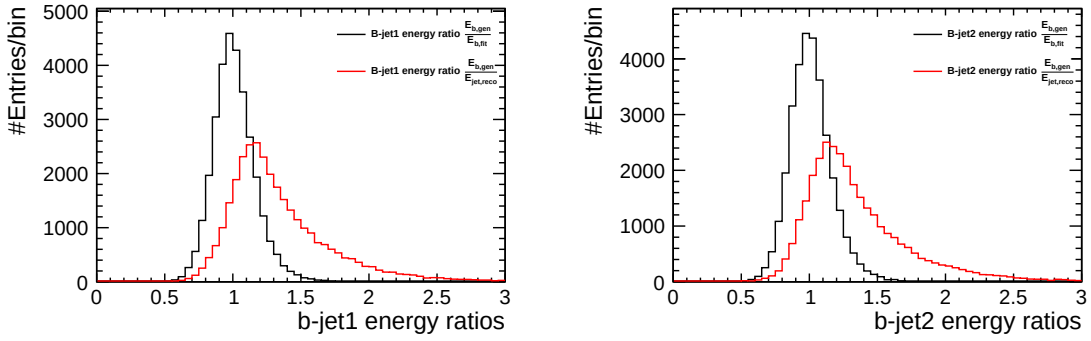

Figure 5.8: Effect of the kinematic fit on the energies of $b-jet_1$ (left) and $b-jet_2$ (right). Shown in red are the b-jet-energy ratio after smearing $\frac{E_{gen}}{E_{reco}}$. In black the reconstructed b-jet-energy ratio after the fit $\frac{E_{fit}}{E_{gen}}$ is shown.

that the resolution of the jet modified by the fit is much improved with respect to the response of the jet before the fit. Furthermore the fit corrects the bias of the measured jets to smaller energies.

The fitted objects can now be used to reconstruct the invariant mass of the heavy Higgs boson, shown in red in Fig. 5.9. The black line shows the invariant Mass reconstructed from all the visible decay products and the missing transverse energy after uncertainties have been introduced but before fitting:

$$m_{four-body-mass} = \sqrt{(p_{\tau_{\mathrm{vis},1}} + p_{\tau_{\mathrm{vis},2}} + p_{\mathrm{b1}} + p_{\mathrm{b2}} + p_{\mathrm{T,miss}})^2}, \tag{5.25}$$

The four vector of the missing transverse energy $p_{\mathrm{T,miss}}$ is given by deducting the four vectors of all visible decay components from the heavy Higgs recoil four vector and projecting it onto the transverse plane. The invariant mass distribution before the fit is very broad and does not peak at the generated heavy Higgs boson mass of 300 GeV. The shift to smaller masses and the breadth is larger than what is expected for events

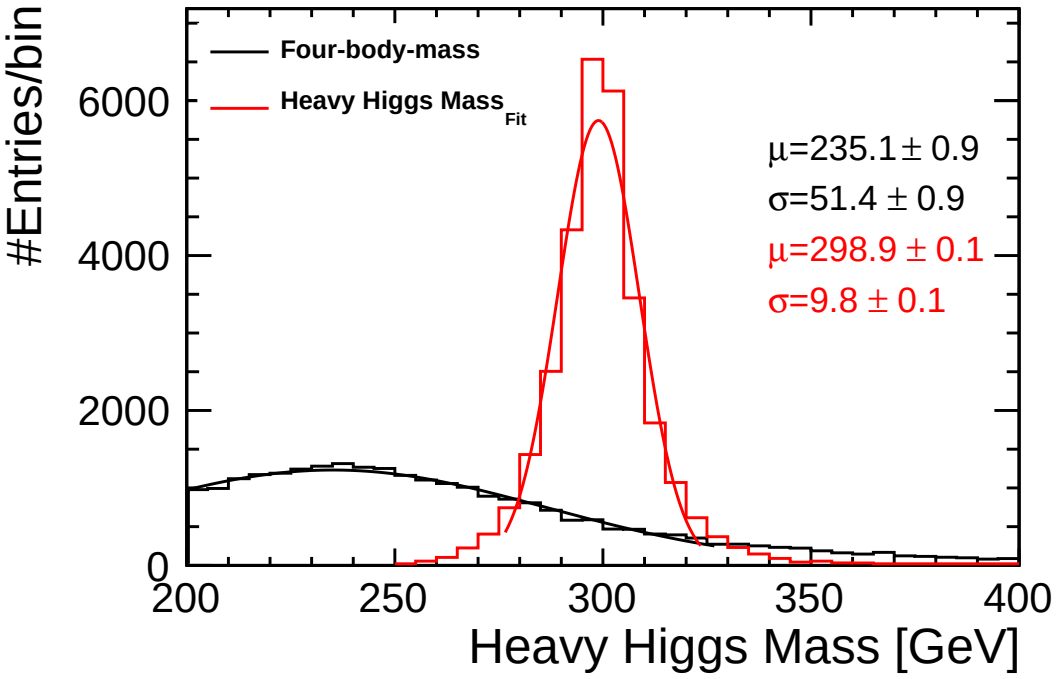

Figure 5.9: Heavy Higgs boson mass reconstructed with fitted tau leptons and *jets* on a toy MC generated from a MC sample with a heavy Higgs boson mass of 300 GeV.

with full CMS detector simulation, as the PDF used to smear the b-parton energies was fixed to the PDF for b-jets with a transverse energy of 25 GeV $< E_{\mathrm{T,reco}} <$ 30 GeV and a pseudorapidity of $|\eta| < 1.2$, which is broader and has a stronger shift than the PDFs for jets with larger transverse energies. The distribution of the reconstructed heavy Higgs mass after fitting peaks at a value around 300 GeV which is the mass used in the generation of the sample. When approximated by a Gaussian distribution the relative mass resolution is 3.3 %. With these satisfying results we move on to study the performance of the HHKinFit on a MC sample with full CMS detector simulation.

5.5 Performance on MC Signal Samples with CMS detector simulation

In this section, the results of the performance checks of the kinematic fit is described for signal events where a full CMS detector simulation has been performed. The structure of the performance tests follow the same outline as the tests on the toy MC presented in the preceding section. For all plots shown in this section, the events are taken from the same MC with a heavy Higgs mass of 300 GeV used to generate the toy MC events in the previous section. The selected events are required to have exactly one hadronic tau and exactly one muon or electron from a decaying tau and two jets matched within

convergence code	definition	event ratio
-2	no solution for di-jet system within given constraints	0.0%
-1	no solution for di-tau system within given constraints	0.0%
0	no minimum found during the fitting process	0.0%
1	fit converged	92.0%
2	fit converged at a limit of the di-jet system	0.0%
3	fit converged at a limit of the di-tau system	8.0%
4	fit converged at a limit of the di-jet and di-tau system	0.0%

Table 5.2: Convergence codes of the kinematic fit and ratio of events for each code for MC events with full detector simulation from a sample with a heavy Higgs boson mass of 300 GeV.

a cone of $\Delta R < 0.1$ to a generated b-parton. An MVA based missing transverse energy reconstruction algorithm has been used.

In Table 5.2 the distribution of convergence codes of the kinematic fit is listed. The distribution is very similar to the distribution of convergence codes on a toy MC listed in Table 5.1. The vast majority of events converges at a point not close to one of the object limits (convergence code 1). Some of the events converge close to the limit of the tau leptons. As explained before, this can happen if the energy of the visible tau decay product is close to the tau lepton energy and the jet energies are mismeasured in such a way, that the jet configuration that gives the smallest $\chi^2_{\mathrm{b}_{1/2}}$ terms differs significantly in the recoil contribution with respect to the true contribution of the jets. The minimal χ^2 values found by the kinematic fit and the corresponding fit probability distribution are shown in 5.10. Again, the minimal χ^2 distribution shows the characteristic peaks at low values and a rapid decline towards larger values. The fit probability was calculated with the theoretical χ^2 probability density function for two degrees of freedom (See 5.3). Despite the used approximation for the COV_{recoil} as described in Section 5.3 the fit probability has a rather flat distribution demonstrating the correctness of the uncertainty description. The mild upwards slope towards higher probability values is likely to be a result of approximating the COV_{recoil} by the covariance matrix of the missing transverse energy $COV_{\vec{E}_{T,miss}}$ as this will result in an overestimation of the uncertainties leading to slightly higher fit probabilities. In Fig. 5.11 and Fig. 5.12, the energy of the visible tau-decay products and the b-jet response before and the energy resolutions after the fit for MC events using a full CMS detector simulation are shown. In Fig. 5.11 the left plot shows the energy fractions for hadronic tau while the right plot shows the same distributions for the leptonically decaying tau. The red lines depict the visible energy fractions $\frac{E_{vis}}{E_{gen}}$ whereas the black line depicts the reconstructed tau energy fraction $\frac{E_{fit}}{E_{gen}}$. It is noteworthy, that the hadronic tau tends to have a higher visible energy fraction than the leptonically decaying tau, including some events in which the visible energy fraction of the hadronic tau exceeds one, justifying the loosening of the tau fit object limit from $E_{\tau_{fit}} > E_{\tau_{vis}}$ to $E_{\tau_{fit}} > 0.9 \cdot E_{\tau_{vis}}$ as explained in Section 5.2.

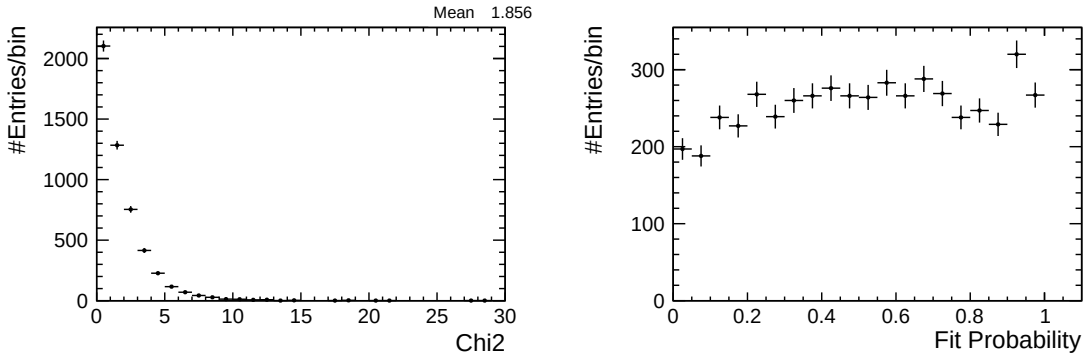

Figure 5.10: Minimal χ^2 value found by the kinematic fit (left) and fit probability calculated with the theoretical χ^2 probability density function for two degrees of freedom (right). The events are taken from a MC with full CMS detector simulation with a heavy Higgs boson mass of 300 GeV.

The fitted tau energy reconstructs the true tau energy quite precisely. The resolution is slightly improved with respect to the tau energy resolution in the toy MC study as the uncertainty of 20 GeV used for smearing the recoil vector for the toy MC is higher than the actual uncertainty observed with the full detector simulation MC. As the distribution is approximately symmetric and peaks at an energy fraction of 1, no bias is introduced by the fit.

Fig. 5.12 shows a similar plot for the b-jets. Here, the red line shows the jet energy fraction of the reconstructed jet $\frac{E_{gen}}{E_{reco}}$ while the black line shows the reconstructed b-jet-energy ratio $\frac{E_{fit}}{E_{gen}}$. As in the plots shown for the toy MC study in Section 5.4, E_{gen} is not the energy of the generator jet but the energy of the generated b-parton before any final state radiation or hadronisation occurs. Again the same tendency demonstrated in the toy MC study holds up for events using a full CMS detector simulation. The resolution of the jet modified by the fit is improved with respect to the resolution of the measured jet and the fit corrects the bias of the measured jets to smaller energies introduced by final state radiation, hadronisation and neutrinos.

The invariant heavy Higgs boson mass reconstructed from the fitted taus and b-jets is shown as the red line in Fig. 5.13. The black line shows the invariant Mass reconstructed from all the visible decay products before the fit and the missing transverse energy as given by Eq. 5.25, where the $p_{\mathrm{T,miss}}$ is the four-vector of the missing transverse energy given by:

$$p_{\mathrm{T,miss}} = \begin{pmatrix} E_{\mathrm{T,miss}} \\ p_{\mathrm{x,miss}} \\ p_{\mathrm{y,miss}} \\ 0 \end{pmatrix}. \tag{5.26}$$

Before the fit, the invariant mass distribution is very broad and does not peak at the generated heavy Higgs boson mass of 300 GeV, mostly due to the unmeasured neutrinos

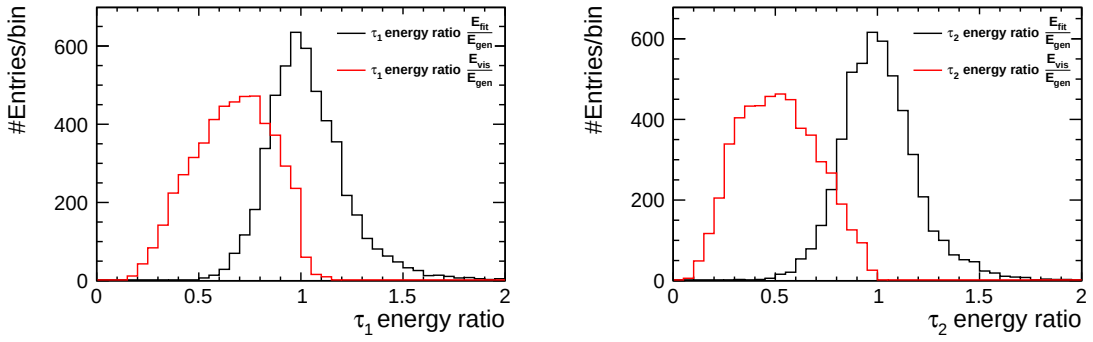

Figure 5.11: Effect of the kinematic fit on the energies of the hadronically decaying tau (left) and the leptonically decaying tau (right). Shown in red are the visible energy fractions $\frac{E_{vis}}{E_{gen}}$. In black the reconstructed tau energy fraction $\frac{E_{fit}}{E_{gen}}$ is shown.

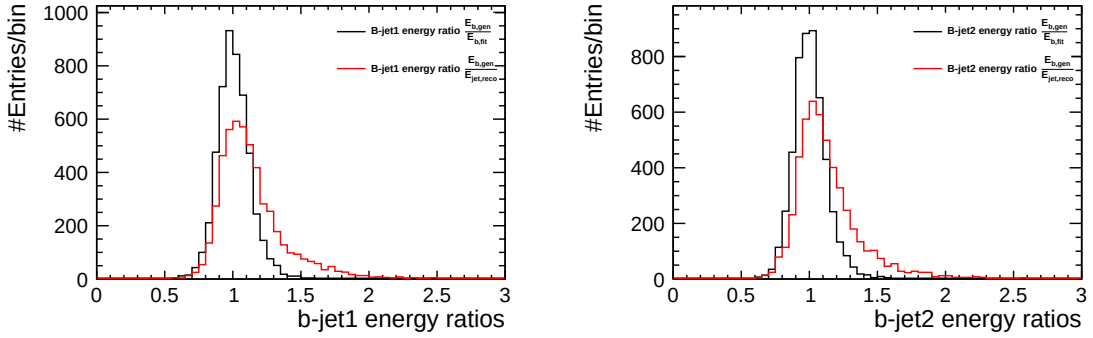

Figure 5.12: Effect of the kinematic fit on the energies of $b - jet_1$ (left) and $b - jet_2$ (right). Shown in red are the b-jet-energy ratios before the fit $\frac{E_{gen}}{E_{reco}}$. In black the reconstructed b-jet-energy ratio after the fit $\frac{E_{fit}}{E_{gen}}$ is shown.

in the event. The mass reconstructed by the kinematic fit peaks around 300 GeV and has a much better relative mass resolution of approximately 2.8%.

In summary, it was shown that the HHKinFit is a powerful and reliable tool. The flat fit probabilities demonstrate that the uncertainties used in the fit are well described and the invariant mass of the heavy Higgs object has a much improved resolution with respect to the four-body-mass reconstructed as described by Eq. 5.25. In the following chapter an analysis is presented that will make heavy use of this fit demonstrating its power for analysis.

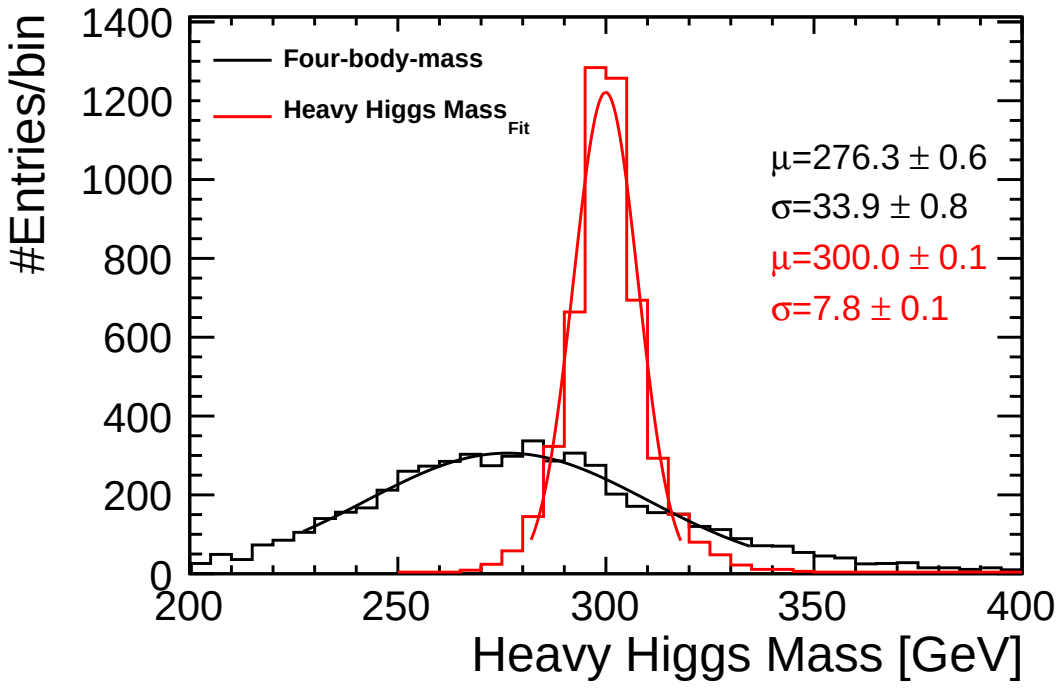

Figure 5.13: Heavy Higgs boson mass reconstructed with fitted taus and jets on a MC sample with full CMS detector simulation together with the Four-body-mass as given by Eq. 5.25. The generated heavy Higgs boson has a mass of 300 GeV.

Chapter 6

Search for a heavy Higgs boson

In the following chapter, a search for a heavy Higgs boson decaying to two light Higgs bosons which then decay to two tau leptons and two b-jets is presented. The search was performed at a center-of-mass energy of 13 TeV. The data with an integrated luminosity of $2.30\,\mathrm{fb}^{-1}$ was collected by the CMS experiment in 2015. A similar analysis to which I contributided by providing a former version of the kinematic fitting tool presented in Chapter 5 [85], has been performed on data amounting to an integrated luminosity of $19.7\,\mathrm{fb}^{-1}$ collected during the 8 TeV running period of the LHC in 2012 [1]. No signs of a heavy uncharged Higgs boson H were found and exclusion limits were set.

The aforementioned decay channel is of interest as within the MSSM, a theoretically well motivated heavy Higgs boson of a mass between 250 and 350 GeV would predominantly decay into two light Higgs Bosons for low values of $\tan\beta$(see Sec. 2.4.1). Also, more general 2HDMs exist in which the decacy of a heavy Higgs boson to two light Higgs bosons could be sizeable up to higher masses (Sec. 2.4.2).

Furthermore the decay channel where one light Higgs decays into two tau leptons and the other decays into two b-jets is a good compromise between a high branching ratio and a good selection efficiency. The branching ratio is reasonably high, as the Higgs decay to two b quarks has the highest branching ratio of all possible Higgs decays and as the branching ratio for a Higgs boson to decay into two tau leptons is still reasonably large, as it is the heaviest of the leptons. A good selection efficiency is given due to the comparably good reconstruction and identification efficiency of the leptonic tau decay products.

This analysis is confined to the channel where one tau decays to a muon while the other decays hadronically as this is the channel that yielded the best limits in the 8 TeV analysis due to the good muon reconstruction efficiency and the enhanced branching ratio for a tau to decay hadronically.

6.1 Object Definitions

The CMS software together with the particle flow algorithm translates energy deposits and hits measured by the tracker, the calorimeters and the muon chambers into easier to interpret physics objects with tracks, energy deposits and resulting four-momentum vectors. To identify these physic objects as certain particles and jets, object specific cuts defined by the respective physics object group (POG) of CMS are applied to maximize the selection efficiency while minimizing the missidentification rate. In the following the cuts applied to identify the particles in this analysis are presented.

6.1.1 General acceptance criteria

Every object has to pass some basic kinematic selection criteria on the transverse momentum and the pseudorapidity. The criteria common to many objects are listed in Table 6.1. Besides the transverse momentum, the pseudorapidity and the relative isolation as defined by Eq. 3.14, most objects have to pass a requirement on the distance of their track to the primary vertex in the x-y-plane (d_{xy}) and in the longitudinal plane (d_z). Additionally, some object specific selection criteria described in the following, are applied.

	p_T [GeV]	$\lvert\eta\rvert$	d_{xy} [cm]	d_z [cm]	I_{rel}
Muon	> 20	< 2.1	< 0.045	< 0.2	< 0.15
Di-muon-veto Muon	> 15	< 2.4	< 0.045	< 0.2	< 0.3
Third-lepton-veto Muon	> 10	< 2.4	< 0.045	< 0.2	< 0.3
Third-lepton-veto Electron	> 10	< 2.5	< 0.045	< 0.2	< 0.3
Hadronic Tau	> 20	< 2.3		< 0.2	
Jets	> 20	< 2.4			

Table 6.1: Requirements on identification criteria common to many objects.

6.1.2 Muons

The basis for the muon reconstruction are the PF muon, tracker muon and global muon algorithms described in Section 3.4.2. Muons are required to pass the medium muon ID as defined by the muon POG. Besides some additional cuts mostly related to the quality of the track fit, the medium working point of the muon ID requires that the object was reconstructed as a muon by the particle flow algorithm and was additionally reconstructed as either a global muon or a tracker muon. Two further muon IDs are defined by the CMS Higgs to Tau Tau working group, which will be used later to exclude events with more than one muon. A di-muon-veto muon is required to be reconstructed as a global muon, a PF muon and a tracker muon. A third-lepton-veto muon has to

pass the medium muon ID.

6.1.3 Hadronic Taus

Hadronic taus (τ_h) are reconstructed by the HPS algorithm introduced in Section 3.4.5. For an object to be considered as a hadronic tau, it has to be identified as a hadronic tau by the HPS decay mode finder. Additionally it has to be identified as a hadronic tau by the BDT trained to distinguish hadronic taus from electrons at the very loose working point and by the BDT trained to distinguish hadronic taus from muons at the tight working point. The object must pass the medium isolation working point, which requires the isolation to be below 1 GeV. The isolation for the hadronic tau is calculated as described in Sec. 3.4.7.

6.1.4 Jets

The jets used in the analysis are reconstructed with the $anti-k_t$ algorithm with a cone size of 0.4. Charged hadron subtraction was applied to exclude charged hadrons not originating from the primary vertex from the jet reconstruction. After reconstruction, the following cuts are applied:

- **Neutral hadronic energy fraction** < 0.99**:** The energy fraction deposited by neutral particles in the hadronic calorimeter has to be below 0.99.
- **Neutral electromagnetic energy fraction** < 0.99**:** The energy fraction deposited by neutral particles in the electromagnetic calorimeter has to be below 0.99.
- **Muon energy fraction** < 0.8**:** The energy fraction deposited by muons has to be below 0.8.
- **Number of constituents** > 1**:** The jet must consist of more than one component (PF particle).
- **Charged hadron energy fraction** > 0**:** The fraction of energy deposited by charged particles in the hadronic calorimeter has to be above 0.
- **Charged Multiplicity** > 0**:** The jet must have at least one charged constituent.
- **Charged electromagnetic energy fraction** < 0.99**:** The fraction of energy deposited by charged particles in the electromagnetic calorimeter has to be below 0.99.

Jets passing the medium CSV working point of CSV value > 0.814 are categorized as b-jets.

6.1.5 Further Objects

Electrons are not used directly in this analysis. A rough electron ID still has to be defined, as events with electrons will be excluded from the analysis to exclude any events that might otherwise also be selected by this search in the e-τ_{had} channel. The third-lepton-veto electron ID, as defined by the CMS Higgs to Tau Tau working group, requires that the object is not identified as a conversion electron by checking for missing hits in the first layers of the tracker and has at most one missing hit in the inner tracker. Additionally, the object is required to pass the 90% efficiency working point of an MVA ID defined by the electron POG.

6.2 Preselection

Before studying the backgrounds and optimizing selection criteria, some preselection cuts are applied that almost all signal events of the signal process should pass.
First, a set of all possible τ_h-μ pairs with opposite charge are created. For this, only muons that can be matched to a trigger object that triggered the HLT_IsoMu_18 trigger within $\Delta R < 0.5$ are considered. The pair that contains the hadronic tau with the highest transverse momentum is chosen as the primary pair. In case of a tie between multiple pairs, the pair that contains the most isolated hadronic tau is chosen. If there still is a tie, most likely because the pairs contain the same hadronic tau, the pair with the highest transverse momentum muon, or in a case of a tie, the most isolated muon is chosen. If an event contains no opposite sign τ_h-μ pair it is discarded.
Next, all jets within a distance of $\Delta R < 0.5$ of a hadronic tau or muon belonging to the selected primary pair are removed from the event to ensure that the hadronic tau/muon is not additionally reconstructed as a jet. After this jet cleaning, events are required to have at least two jets. Otherwise they are discarded. Lastly, the event must not have more then one di-muon-veto muon or third-lepton-veto muon and no third-lepton-veto electron. To select the two jets that will be used as an input for the HHKinFit, the jets are ordered in descending order of their CSV value and the two jets with the highest CSV value are selected.
Three event categories are defined depending on the number of b-jets in the event:

- $n_{b-jets} = 0$**:** This event category is expected to be far less sensitive to a possible signal than the $n_{b-jets} \geq 2$ event category. However, it is still included as a cross-check for the background estimation.

- $n_{b-jets} = 1$**:** The $n_{b-jets} = 1$ event category also lacked sensitivity in past analysis efforts. However, as a new approach to the final event selection will be performed within this analysis, it is still included to study the sensitivity of the channel.

- $n_{b-jets} \geq 2$**:** This event category was the most sensitive in the past as it strongly suppresses all backgrounds except for the background arising from $t\bar{t}$ processes.

6.3 Datasets and MC samples

A total of $3.81\,\text{fb}^{-1}$ of 13 TeV proton-proton collisions were recorded by the CMS experiment in 2016. Mainly due to difficulties with the cooling system of the magnet, the luminosity for data with good running conditions is lower ($2.63\,\text{fb}^{-1}$). Additionally, during some runs the hadronic forward calorimeter was not operational. These runs are excluded from the data used for this analysis as to not introduce systematic errors due to the MVA-based missing transverse energy calculation, which was trained assuming the full coverage of the hadronic calorimeter. In total, data with an integrated luminosity of $2.30\,\text{fb}^{-1}$ is analyzed.[1] The Run2015C dataset is not used, as the required trigger was not yet operational while the data was collected. The amount of data lost by excluding this dataset is $0.02\,\text{fb}^{-1}$ and therefore negligible.

The data was collected with the HLT_IsoMu_18 trigger. The trigger requires an isolated muon with a p_T of at least 18 GeV. Using this trigger with its loose p_T requirement was possible because the instantaneous luminosity was lower than what was initially expected. Future analysis efforts might have to switch to a trigger with a higher muon p_T threshold. The analyzed dataset, that was collected with a level 1 trigger requiring a muon, is listed in Tab. 6.2.

Dataset name	**Luminosity**
`/SingleMuon/Run2015D-16Dec2015-v1/`	$2.30\,\text{fb}^{-1}$

Table 6.2: Analyzed dataset and JSON file name.

The MC samples used for background estimation and the signal samples are listed in Tab. 6.4 and Tab. 6.3 respectively. The MC samples for the W+Jets background are stitched together by excluding all events with 1 to 4 jets from the matrix element in the `WJetsToLNu_TuneCUETP8M1_13TeV-madgraphMLM-pythia8/` sample and adding the respective samples with 1, 2, 3 or 4 jets from the matrix element. This is done to increase the

[1] This corresponds to the golden JSON file `Cert_13TeV_16Dec2015ReReco_Collisions15_25ns_JSON_v2.txt` released on the 3rd of march by the CMS Data Quality Monitoring (DQM) group constrained to runs in the Run2015D dataset.

Process	Sample name	Simulated Events	Cross section [pb]
Single Boson			
W+Jets $\rightarrow \ell\nu$+Jets	WJetsToLNu_TuneCUETP8M1_13TeV-madgraphMLM-pythia8/	47160742	61526.7
W+Jets $\rightarrow \ell\nu$+1 Jet	W1JetsToLNu_TuneCUETP8M1_13TeV-madgraphMLM-pythia8/	45397616	11777.9
W+Jets $\rightarrow \ell\nu$+2 Jets	W2JetsToLNu_TuneCUETP8M1_13TeV-madgraphMLM-pythia8/	30190071	3840.1
W+Jets $\rightarrow \ell\nu$+3 Jets	W3JetsToLNu_TuneCUETP8M1_13TeV-madgraphMLM-pythia8/	18975292	1166.0
W+Jets $\rightarrow \ell\nu$+4 Jets	W4JetsToLNu_TuneCUETP8M1_13TeV-madgraphMLM-pythia8/	8947153	560.04
Z/γ+Jets $\rightarrow \ell\ell$+Jets	DYJetsToLL_M-50_TuneCUETP8M1_13TeV-madgraphMLM-pythia8/	8947153	6025
Top			
$t\bar{t} \rightarrow W^+W^-q\bar{q}$ (q=b,s,d)	TT_TuneCUETP8M1_13TeV-powheg-pythia8/	97994304	831.76
$\bar{t} \rightarrow W^-\bar{q}$ (q=b,s,d)	ST_tW_antitop_5f_inclusiveDecays_13TeV-powheg-pythia8_TuneCUETP8M1/	999399	35.6
$t \rightarrow W^+q$ (q=b,s,d)	ST_tW_top_5f_inclusiveDecays_13TeV-powheg-pythia8_TuneCUETP8M1/	999999	35.6
Di boson			
VV $\rightarrow 2\ell 2\nu$ (V=W,Z)	VVTo2L2Nu_13TeV_amcatnloFXFX_madspin_pythia8/	1729812	11.95
ZZ $\rightarrow 2\ell q\bar{q}$	ZZTo2L2Q_13TeV_amcatnloFXFX_madspin_pythia8/	9660516	3.22
ZZ $\rightarrow 4\ell$	ZZTo4L_13TeV-amcatnloFXFX-pythia8/	7416561	1.212
WW $\rightarrow \ell\nu q\bar{q}$	WWTo1L1Nu2Q_13TeV_amcatnloFXFX_madspin_pythia8/	3239272	49.997
WZ $\rightarrow 2\ell q\bar{q}$	WZTo2L2Q_13TeV_amcatnloFXFX_madspin_pythia8/	15393467	5.595
WZ $\rightarrow 3\ell\nu$	WZJToLLLNu_TuneCUETP8M1_13TeV-amcnlo-pythia8/	1201538	4.708
WZ $\rightarrow \ell 3\nu$	WZTo1L3Nu_13TeV_amcatnloFXFX_madspin_pythia8/	942041	3.05
WZ $\rightarrow \ell\nu q\bar{q}$	WZTo1L1Nu2Q_13TeV_amcatnloFXFX_madspin_pythia8/	11466064	10.71

Table 6.4: MC samples used for background estimations together with the associated process, the cross section and the generated number of events.

number of simulated events with 1 or more jets from the matrix element, as these are the events most likely to pass the signal selection. This drastically reduces the statistic uncertainty for the final estimation of the W+jets background estimation.
All events are generated using Pythia 8 as the parton shower event generator. The matrix elements for the Top processes are generated using Powheg. All other events are generated with MadGraph5 as the matrix element generator. The single boson events are generated with leading order accuracy while all other events are generated with next-to-leading order accuracy.

Sample name	m_H **[GeV]**	**#Events**
/GluGluToRadionToHHTo2B2Tau_M-250_narrow_13TeV-madgraph/	250	299200
/GluGluToRadionToHHTo2B2Tau_M-260_narrow_13TeV-madgraph/	260	299999
/GluGluToRadionToHHTo2B2Tau_M-270_narrow_13TeV-madgraph/	270	300000
/GluGluToRadionToHHTo2B2Tau_M-280_narrow_13TeV-madgraph/	280	286000
/GluGluToRadionToHHTo2B2Tau_M-300_narrow_13TeV-madgraph/	300	500000
/GluGluToRadionToHHTo2B2Tau_M-320_narrow_13TeV-madgraph/	320	300000
/GluGluToRadionToHHTo2B2Tau_M-340_narrow_13TeV-madgraph/	340	293600
/GluGluToRadionToHHTo2B2Tau_M-350_narrow_13TeV-madgraph/	350	300000
/GluGluToRadionToHHTo2B2Tau_M-400_narrow_13TeV-madgraph/	400	294400
/GluGluToRadionToHHTo2B2Tau_M-450_narrow_13TeV-madgraph/	450	99600
/GluGluToRadionToHHTo2B2Tau_M-500_narrow_13TeV-madgraph/	500	98400
/GluGluToRadionToHHTo2B2Tau_M-550_narrow_13TeV-madgraph/	550	100000
/GluGluToRadionToHHTo2B2Tau_M-600_narrow_13TeV-madgraph/	600	100000
/GluGluToRadionToHHTo2B2Tau_M-650_narrow_13TeV-madgraph/	650	100000
/GluGluToRadionToHHTo2B2Tau_M-700_narrow_13TeV-madgraph/	700	99000
/GluGluToRadionToHHTo2B2Tau_M-800_narrow_13TeV-madgraph/	800	100000
/GluGluToRadionToHHTo2B2Tau_M-900_narrow_13TeV-madgraph/	900	100000

Table 6.3: List of signal samples for various heavy Higgs masses.

6.4 MC to Data scale factors

To account for differences between the collected Data and the samples from MC simulation, several scale factors are applied.

6.4.1 Pile-up

First, PU reweighting is applied. The number of additional interactions per bunch crossing differs slightly between data and simulation. It is important to correct for this difference, as particle isolations and the resolution of the missing transverse energy depend on the number of PU interactions. A histogram for the number of interactions per event on data is derived by calculation, taking into account the running conditions and the total proton-proton inelastic cross section. The same histogram can be created

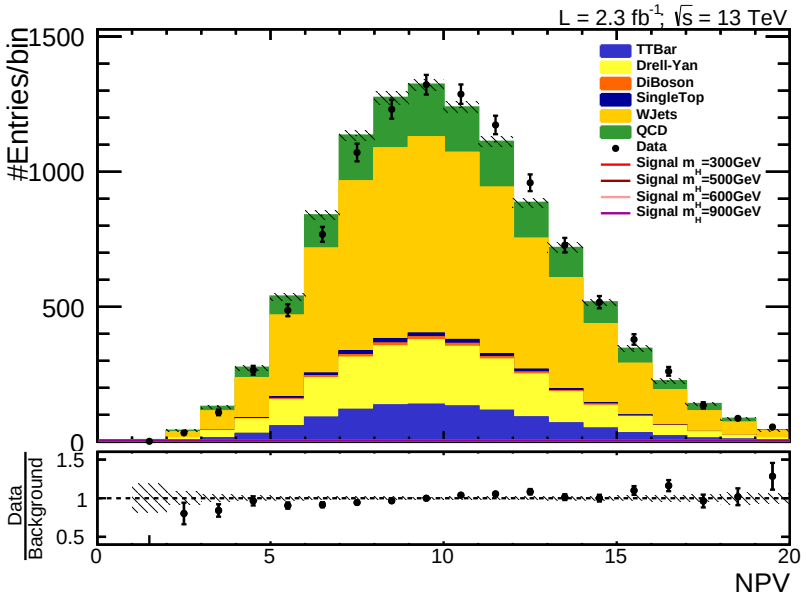

Figure 6.1: Number of reconstructed vertices in data and for all backgrounds after PU reweighting.

for simulation, by using the generator information. Dividing each bin of the histogram derived from data by the corresponding bin in the histogram derived from simulation yields the scale factors that are applied to simulation depending on the true number of interactions. As a cross check, the number of reconstructed vertices in an event in data and simulation after PU reweighting is shown in Fig. 6.1. The background prediction agrees well with the events from data. Minor differences can be observed, as the number of reconstructed vertices is sensitive to differences in the underlying event in data and MC.

6.4.2 Muons

Differences between the efficiency of the muon identification and isolation between simulation and data have been spotted by the muon POG. The muon POG derived scale factors to be applied to simulation by a tag and probe method on Z$\rightarrow \mu\mu$ events similar to the method described in the next paragraph. The scale factors depend on the p_T and $|\eta|$ values of the muons in the event.

6.4.3 Trigger

The trigger used for collecting the dataset used in this analysis was simulated for the MC samples. However differences between the data and MC trigger efficiency were spotted in a tag-and-probe study in Z$\rightarrow \mu\mu$ events. After applying all previously described scale

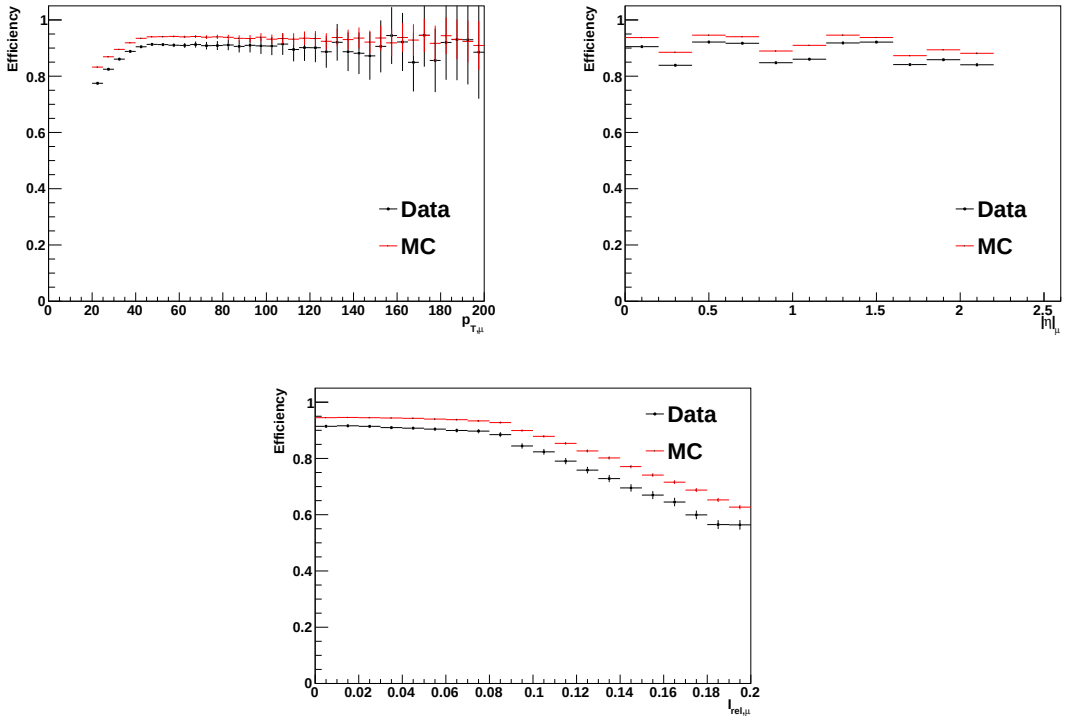

Figure 6.2: Trigger efficiencies for data (black) and simulation (red) in dependence of the probe muons p_T (top left), $|\eta|$ (top right) and relative isolation (bottom) values.

factors, events with two opposite sign muons that pass the same ID criteria as muons used in the analysis except the isolation requirement are selected on data and on a Drell-Yan MC sample. Events with af distance between the muons of $\Delta R < 0.5$ or an invariant di-muon mass deviating more than 20 GeV from the Z-boson mass of 91 GeV are discarded. One of the two muons is selected at random. If it can be matched to a trigger object that triggered the HLT_IsoMu_18 trigger, it is designated as the tag muon while the other muon is designated as the probe muon. The fraction of probe muons that can be matched to another trigger object then give the trigger efficiency that can be derived as a function of several probe muon observables.

In Fig. 6.2 the trigger efficiencies are shown for data (black) and simulation (red) in dependence of the probe muons p_T, $|\eta|$ and relative isolation values. The difference between simulation and data varies with η and p_T. As the dependence of the scale factor on p_T only changes significantly when stepping from the $p_T < 30$ GeV region to higher transverse momenta, the scale factors are derived in dependence of $|\eta|$ for muons with $p_T < 30$ GeV and for muons with $p_T \geq 30$ GeV. The derived scale factors are shown in Fig. 6.3.

Trigger efficiencies after applying scale factors are shown in Fig. 6.4. The trigger efficiencies are in good agreement over the whole p_T and $|\eta|$ range. A difference is observed for muons with high relative isolation values $I_{rel} > 0.1$. However, as approximately 90% percent of all background and 87% of all signal events only feature muon isolation

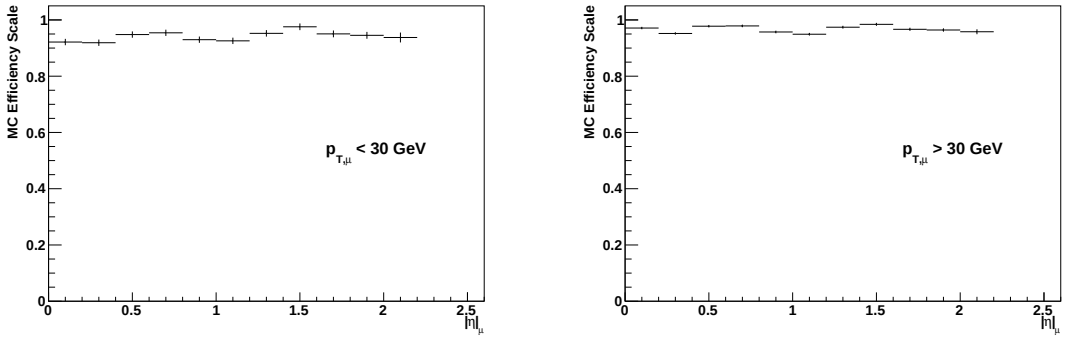

Figure 6.3: MC to data scale factors to correct for differences in trigger efficiencies for muons with $p_T < 30\,\text{GeV}$ (left) and $p_T \geq 30\,\text{GeV}$ (right).

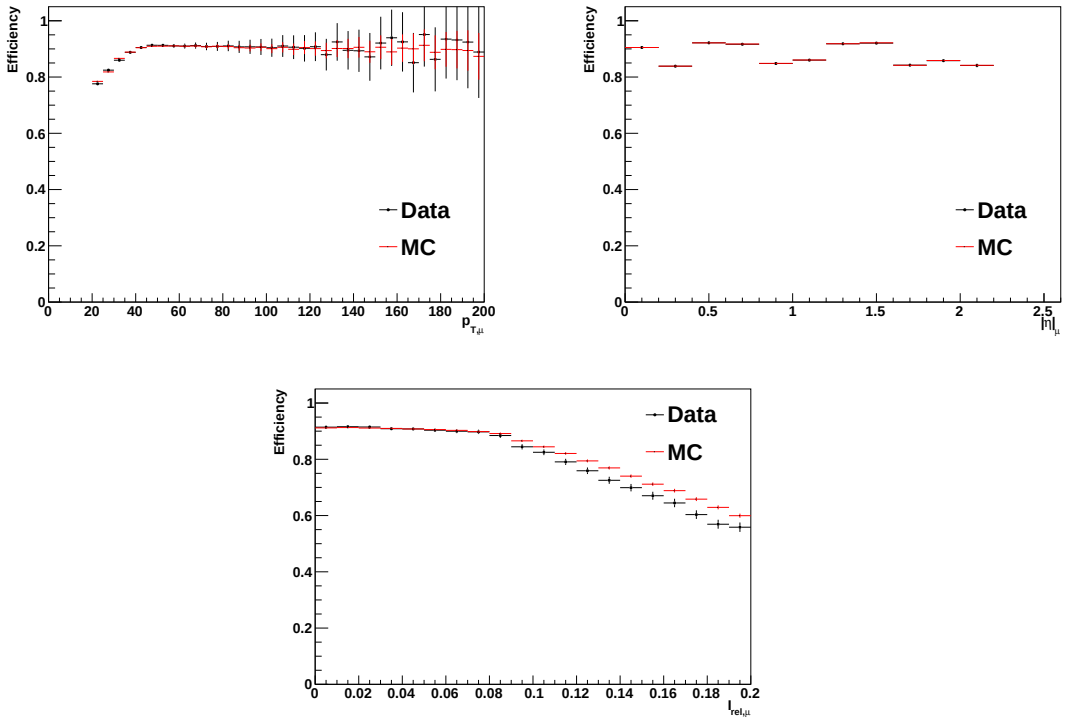

Figure 6.4: Trigger efficiencies for data (black) and simulation (red) in dependence of the probe muons p_T (top left), $|\eta|$ (top right) and relative isolation (bottom) values after applying the MC to data scale factors shown in Fig. 6.3.

values smaller than 0.1, this effect is assumed to be negligible and well covered by other uncertainties.

6.4.4 B tagging

The jet CSV discriminator value distribution is differently shaped in data and simulation. The b-jet POG performed a tag-and-probe study on a $t\bar{t}$ enriched sample to derive scale factors for heavy-flavor jets (b-jets). To derive the scale factors for light flavor jets (u, d

and s jets), a Z+jets enriched sample was used. The scale factors are applied to events from simulation in dependence of the p_T, $|\eta|$ and CSV-values of the jets in the event. Due to the complexity of the method by which these scale factors are derived, a total of 9 different uncorrelated sources of uncertainties have to be considered. The uncertainties will be listed in more detail in Section 6.7.

6.5 Background Estimations

The vast majority of events passing the event selection will not be events from a possible signal, but background events. To be able to make sense of the data passing the event selection, it is crucial to have an excellent understanding of all background processes. To avoid introducing systematic uncertainties from theory predictions, some of the backgrounds are estimated by a data-driven technique. Most of the background estimation methods are unchanged with respect to the analysis using 8 TeV data, presented in [1].

6.5.1 Background from Top-quark pair production

The background from $t\bar{t}$ processes is the major background in the most sensitive $n_{b-jets} \geq 2$ event category. The shape and scale of this background are taken directly from simulation. The transverse mass of the event is defined as the invariant mass of the muon and the missing transverse energy constrained to the transverse plane:

$$m_T = \sqrt{2E_{T,\mu}E_{T,miss} \cdot (1 - \cos\alpha)}, \tag{6.1}$$

with α being the angle between the muon and the missing transverse energy in the transverse plane. The transverse mass can be used to define a control region with a high $t\bar{t}$ purity.

The agreement with data is checked in a control region with $n_{b-jets} \geq 2$ and $m_T > 100\,\text{GeV}$. The $t\bar{t}$ purity in this region is 95.5%. Fig. 6.5 shows the m_T distribution in this region. As can be seen the data and the estimated contribution from $t\bar{t}$ are in agreement within their uncertainties. The total background to data scale is 1.055 ± 0.058 and therefore compatible with 1. Any scale uncertainties of the background are assumed to be covered by the $t\bar{t}$ cross section (5.1%) and luminosity uncertainties (2.6%).

6.5.2 Drell-Yan $Z \to \tau\tau$ Background

In past analysis efforts, this background was estimated by a so called embedding technique, in which a $Z \to \mu\mu$ sample is selected in data and the muons are exchanged with taus from simulation. Unfortunately no embedded samples are available for the 13 TeV data-taking period at the time of this writing. Therefore, a pure MC sample will be used to estimate the Drell-Yan background. A cross section uncertainty of 3.7% will be

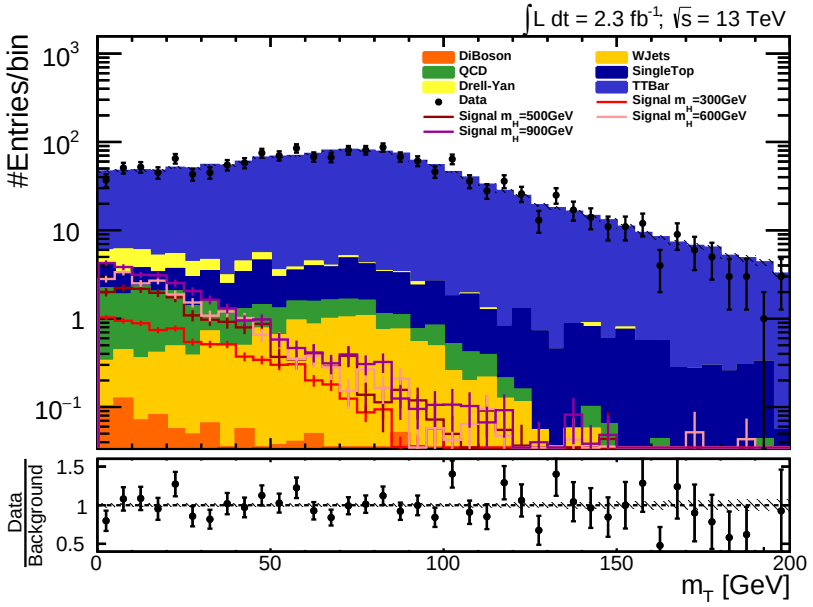

Figure 6.5: m_T distribution for events with $n_{b-jets} \geq 2$. The $t\bar{t}$ purity for events with $m_T > 100\,\text{GeV}$ is 95.5%.

applied.

Luckily, the $Z \to \tau\tau$ background is already a minor background (6.1% of events) in the most sensitive $n_{b-jets} \geq 2$ event category, meaning that systematic uncertainties introduced by relying on the completely simulation based estimation of the background should not significantly influence the final results.

6.5.3 W+Jets Background

W-boson events with jets in the final state can pass the event selection if the W-boson decays to a muon and one of the jets is misreconstructed as a hadronic tau. The scale of the background is estimated by a data-driven technique while the shape of the background is taken from simulation.

The transverse mass distribution for a W+jets and a signal MC sample is shown in Fig. 6.6 for the $n_{b-jets} = 0$ and $n_{b-jets} \geq 2$ event categories. For W boson decays, the transverse mass tends to high values, close to the W boson mass of 80 GeV while signal events tend towards lower transverse mass values. To estimate the scale of the W+jets background, a high-to-low m_T factor is derived from a W+jets MC sample by counting all events passing the event selection for a specific event category with $m_T < 60\,\text{GeV}$ and dividing it by the number of events in a signal depleted control region. For the zero and one b-jet categories, the control region is defined as the events passing the event selection with a transverse mass of $m_T > 70\,\text{GeV}$. In the two b-jet category the $t\bar{t}$ background dominates the very high m_T region and the transverse mass requirement of the control region is changed to $60\,\text{GeV} < m_T < 120\,\text{GeV}$. The scale of the background is then estimated from data by measuring the number of events in the control region in data. The

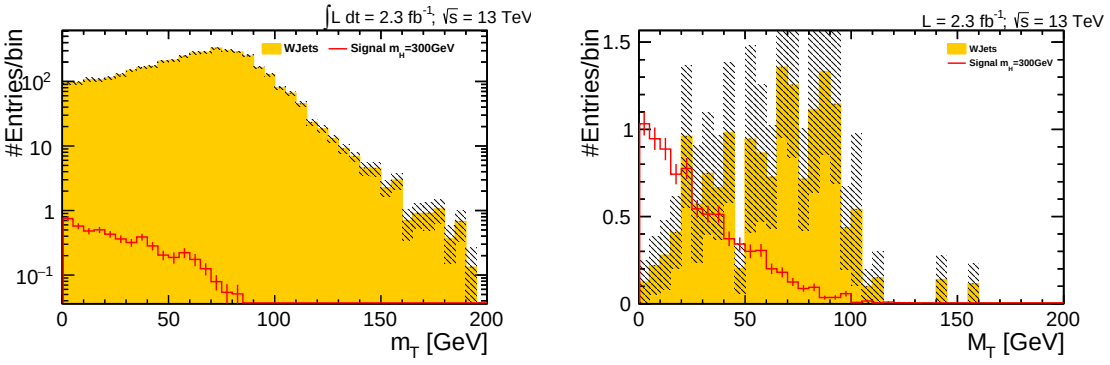

Figure 6.6: Transverse mass distribution for events from a W+jets and signal MC sample in the $n_{b-jets} = 0$ (left) and $n_{b-jets} \geq 2$ (right) event category. The signal is scaled to $\sigma \cdot BR = 1\,\text{pb}$

number of events stemming from any other background than the yet-to-be-determined QCD background is deducted from that number with the assumption that the remainder stems from W+jets events. The number of remaining events is scaled by the high-to-low m_T factor to obtain the estimated number of W+jets events in the low transverse mass region. The W+jets MC sample is then used to estimate the background contribution after it was scaled to match the yield estimated from data.

As the statistics for the W+jets MC sample in the one and two b-tag categories is quite limited, the category selection criteria for the number of required medium b-jets is loosened to the loose b-jet working point for the shape selection applied to events of the W+jets MC. To check for systematic shape uncertainties introduced by loosening the b-jet working point requirement, Fig. 6.7 shows the shapes of the W+jet background estimates when requiring the shape selection to include two b-jets passing the medium CSV working point (red) or the loose CSV working point (green). The shape is compared as a function of the fit probability, the transverse mass and the invariant mass of the di-jet system. As the medium CSV WP sample is a subset of the loose CSV WP sample, their uncertainties are correlated and are depicted independently in the ratio Plot. The error band in the ratio plot depicts the uncertainty of the medium CSV WP sample, while the error bars of the points depict the uncertainty of the loose CSV WP sample. Large statistic uncertainties for the events requiring two medium working point b-jets make a definitive statement difficult, but within the uncertainties, the shapes are in agreement.

As some signal events in the $n_{b-jets} \geq 2$ event category are in the control region of $60\,\text{GeV} < m_T < 120\,\text{GeV}$, a possible signal could slightly increase the yield of the background estimation. As the m_T distribution of the signal does not change significantly for different heavy Higgs masses, the effect of this increase in yield is tested with a signal MC with a generated heavy Higgs mass of 300 GeV. Taking into account the fraction of signal events in the control region (10.5%), the high-to-low m_T scale factor of 0.786

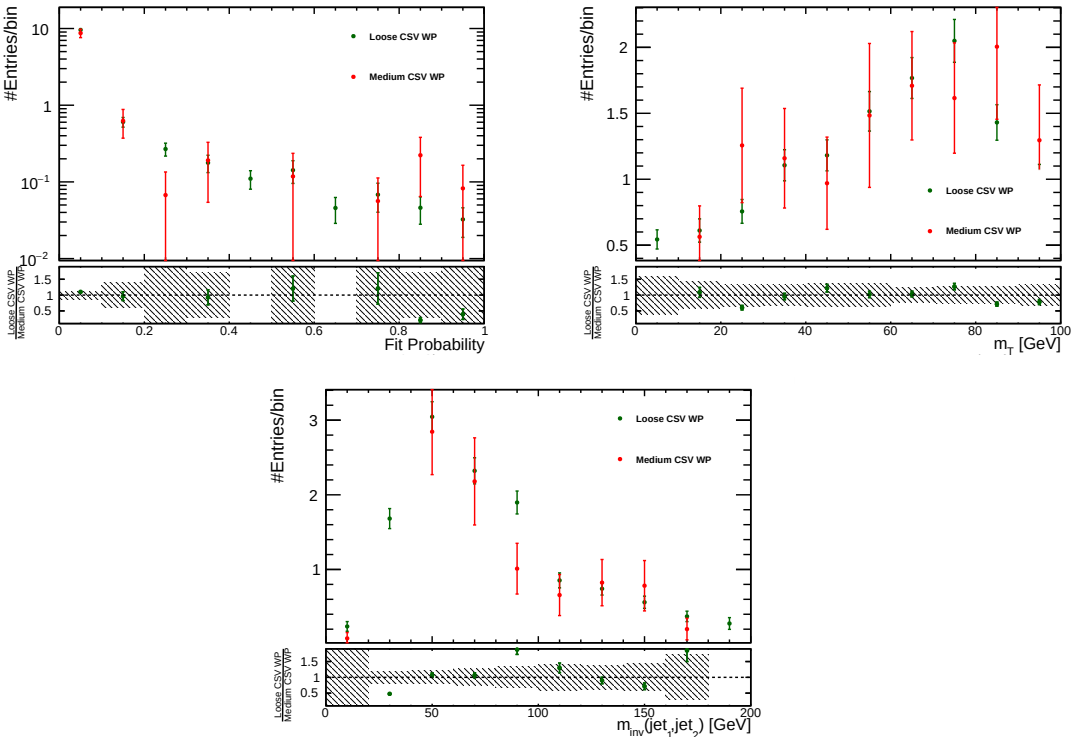

Figure 6.7: Shapes of the W+jet background estimates when requiring the shape selection to include two b-jets passing the medium CSV working point (WP) (red) or loose working point (green). The shape is compared as a function of the fit probability (top-left), the transverse mass (top-right) and the invariant mass of the di-jet system (bottom). The error band in the ratio plot depicts the uncertainty of the medium CSV WP sample, while the error bars of the points depict the uncertainty of the loose CSV WP sample.

and the signal and W+jets background selection efficiency of the final event selection of 73.2% and 17.2% respectively, the yield of the W+jets background in the final result plot in the $n_{b-jets} \geq 2$ event category will be increased by 1.94% of the signal yield. For any signal close to the already excluded $\sigma \cdot BR$ of around $1\,\mathrm{pb}^{-1}$, this increase in events is much smaller than the systematic uncertainty of 182% assigned to the W+jets background, as will be described in Section 6.7. Additionally, signal events in the final result plot are located in a narrow region around the generated heavy Higgs mass while events from the W+jets background follow a much broader distribution further decreasing the relevance of this systematic increase in yield. Therefore, the increase in yield through signal contamination is assumed to be negligible and will be neglected in the following.

6.5.4 QCD Background

QCD events can pass the event selection when the muon and the τ_h in the event are a result of misreconstructed jets.

The QCD background is estimated by an ABCD-Method. In the following, the general principle of the method will be introduced. In this purely data-driven method four

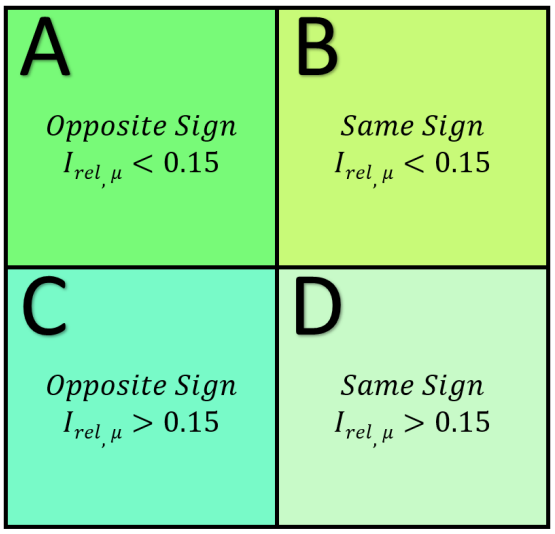

Figure 6.8: Schematic view of event categories used for the ABCD QCD background estimation.

regions A, B, C and D are defined. Region A is the signal region in which the background should be estimated. Regions B, C and D are derived by introducing two cut values along two variables so that all regions are orthogonal to each other. Most often these cut values are defined by inverting one of the original event selection criteria. In region B are all events that pass one of the inverted cut requirement but not the other. Events in region C only pass the other inverted cut requirement and events in region D pass both inverted cut requirements. As the two observables are uncorrelated, the scale of the background can then be estimated by measuring the ratio between the number of events in region C n_C to the number of events in region D n_D and multiplying it by the number of events in region B n_B:

$$n_{\mathrm{A}} = n_{\mathrm{B}} \cdot \frac{n_{\mathrm{D}}}{n_{\mathrm{C}}} \tag{6.2}$$

Regions B, C and D should contain as few signal events as possible, so that the background prediction does not change if signal events are present in data.

For this analysis the regions are defined by inverting the opposite sign requirement of the τ_h-μ pair and muon isolation requirements. A schematic view of the different regions is shown in Fig. 6.8. Events in region B pass the event selection defined in Section 6.2, except that the events are required to have a same-sign instead of an opposite-sign τ_h-μ pair. Events in region C pass the event preselection with muons having an inverted isolation requirement of $I_{rel} > 0.15$ (anti-isolated muon). Region D incorporates all events that have a same-sign μ/τ_h-pair with an anti-isolated muon.

After the number of events from all other known backgrounds have been subtracted from each region in data, the same-to-opposite sign scale is determined from region C and D. This is done once for all event categories combined. To estimate the scale of the QCD

contribution the events from region B for each specific event category are then weighted by the same-to-opposite sign scale.
For the $n_{b-jets} \geq 2$ event category, the number of events in region B is very low, leading to large statistical errors for the scale of the QCD background estimation. To alleviate this problem, the scale for the $n_{b-jets} \geq 2$ QCD background estimation is taken from events without a requirement on the number of b-jets by applying an additional weight to account for the probability $p_{2\mathrm{b}}$ of a QCD event to pass the $n_{b-jets} \geq 2$ requirement. This probability is measured in region D as the ratio of the number of all events n_{D} to the number of events with at least two b-jets $n_{\mathrm{D},2b}$.

$$p_{2\mathrm{b}} = \frac{n_{\mathrm{D},2b}}{n_{\mathrm{D}}} \tag{6.3}$$

For both cases the number of backround events with the given b-jet configuration was subtracted.
The shape for the background is taken from region C. As for the W+jets background before, in order to increase the statistics the b-jet requirement is loosened to include jets passing the loose CSV working point. The shape differences between events selected with b-jets passing the loose CSV working point and jets passing the medium working point are shown in Fig. 6.9. As already explained for the corresponding plots of the W+jet background, the medium CSV WP sample is a subset of the loose CSV WP sample meaning that their uncertainties are correlated. The error band in the ratio plot depicts the uncertainty of the medium CSV WP sample, while the error bars of the points depict the uncertainty of the loose CSV WP sample. As the shapes are in agreement, using the looser CSV working point requirement for the b-jets is well justified.
A possible signal could influence the yield of the QCD background. The effect of signals of different masses on the total increase in yield of the QCD background prediction is studied for a signal with a cross section times branching ratio $\sigma \cdot BR$ of 1 pb. For all masses, the impact on the same-to-opposite sign scale, the probability of an event to pass the $n_{b-jets} \geq 2$ requirement and on the increase of events in region B combines to a total increase in yield of less than 0.5%, which is dwarfed by the uncertainty of 64% assigned to the scale uncertainty of the QCD background, as described in Section 6.7.

6.5.5 Other minor Backgrounds

Other minor backgrounds are taken directly from MC simulation. These include events that feature a combination of two W or Z bosons (Di-boson background) and single-top events. Combined they make up approximately 3% of the total predicted background yield.

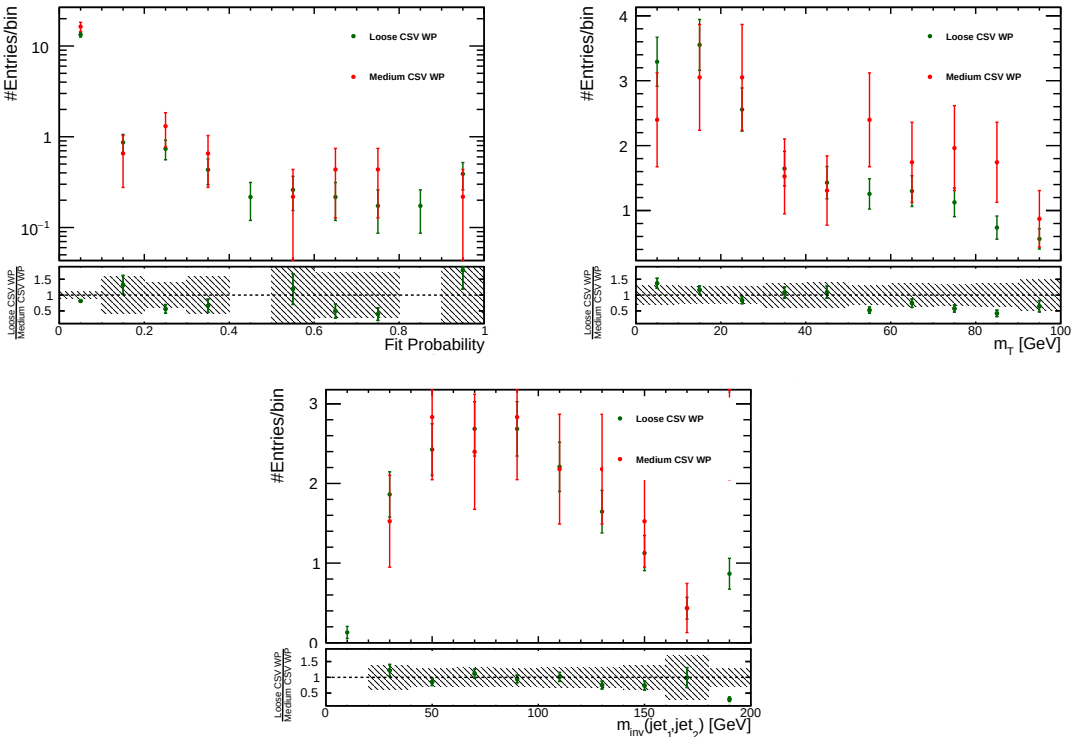

Figure 6.9: Shape differences between QCD estimates when requiring the shape selection (events from region C) to include two b-jets passing the medium CSV working point (WP) (red) or loose working point (green). The shape is compared as a function of the fit probability (top-left), the transverse mass (top-right) and the invariant mass of the di-jet system (bottom). The error band in the ratio plot depicts the uncertainty of the medium CSV WP sample, while the error bars of the points depict the uncertainty of the loose CSV WP sample.

6.5.6 Combined Background

The combined background estimation is checked in several control plots to study the reliability of the estimation methods. Fig. 6.10 and Fig. 6.11 show several distribution of object kinematics and event properties for the $n_{b-jets} \geq 2$ event category. The signal is scaled to $\sigma \cdot BR = 10\,\text{pb}$ in these figures. For all plots presented in the remainder of this chapter, the error bands depict the statistical uncertaintiy for the background predictions of all backgrounds combined.

Some plots for the $n_{b-jets} = 0$ category are shown to check that the data-driven QCD and W+jets background estimations work as expected, while the $n_{b-jets} \geq 2$ category is included to check the reliability of the $t\bar{t}$ simulation and to get a first look at the behavior of the signal in comparison to the backgrounds. The statistical uncertainties of the data in the $n_{b-jets} \geq 2$ event category is quite large, but within the uncertainties all distributions seem to agree well with the background predictions.

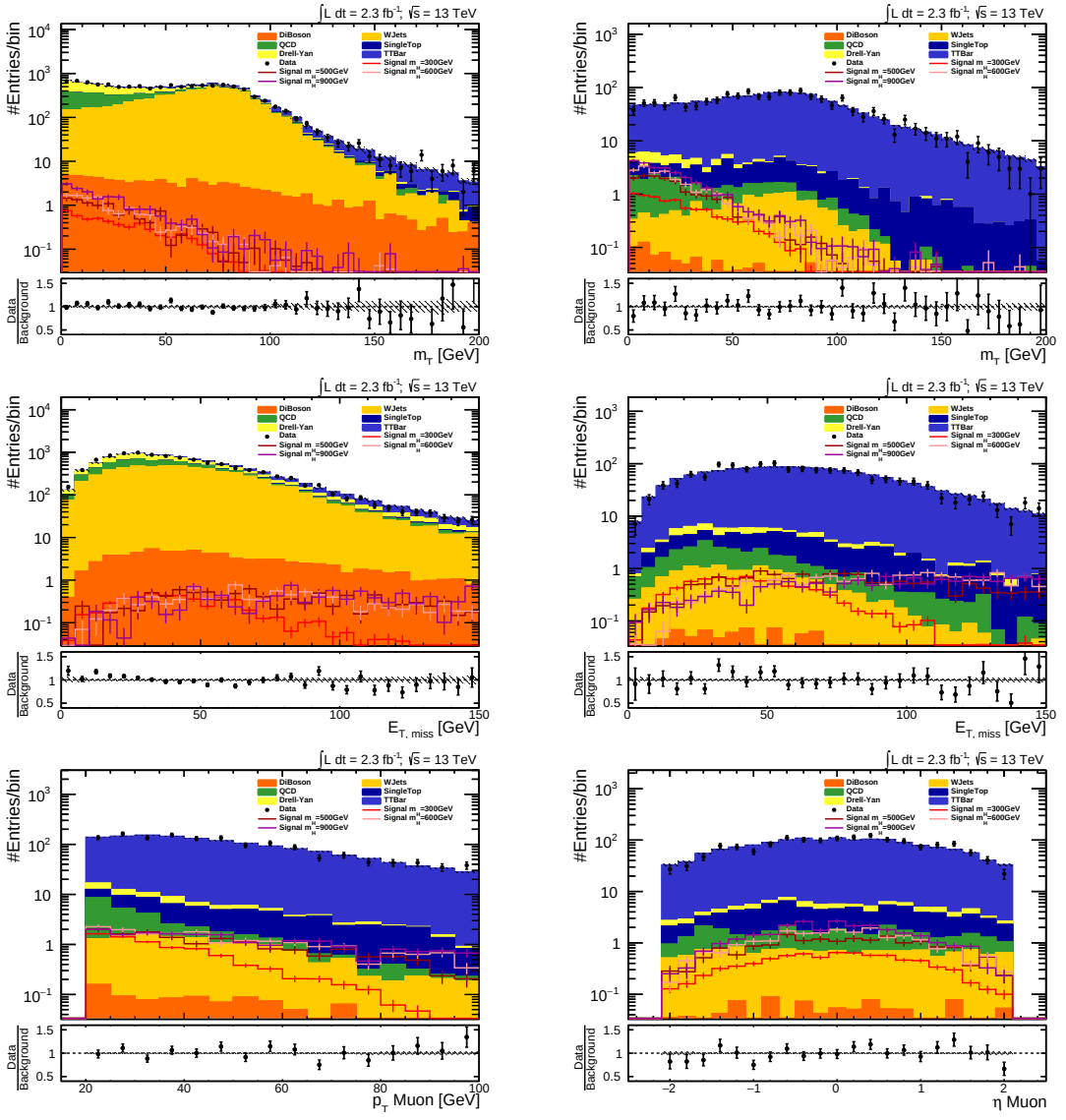

Figure 6.10: Control plots after preselection for data and background estimation. All signals are scaled to $\sigma \cdot BR = 10\,\text{pb}$. The transverse mass (top) and missing transverse energy (middle) are shown for the $n_{b-jets} = 0$ (left) and $n_{b-jets} \geq 2$ (right) events category. In the bottom row, the transverse momentum (left) and pseudorapidity (right) of the muon is shown for events in the $n_{b-jets} \geq 2$ events category.

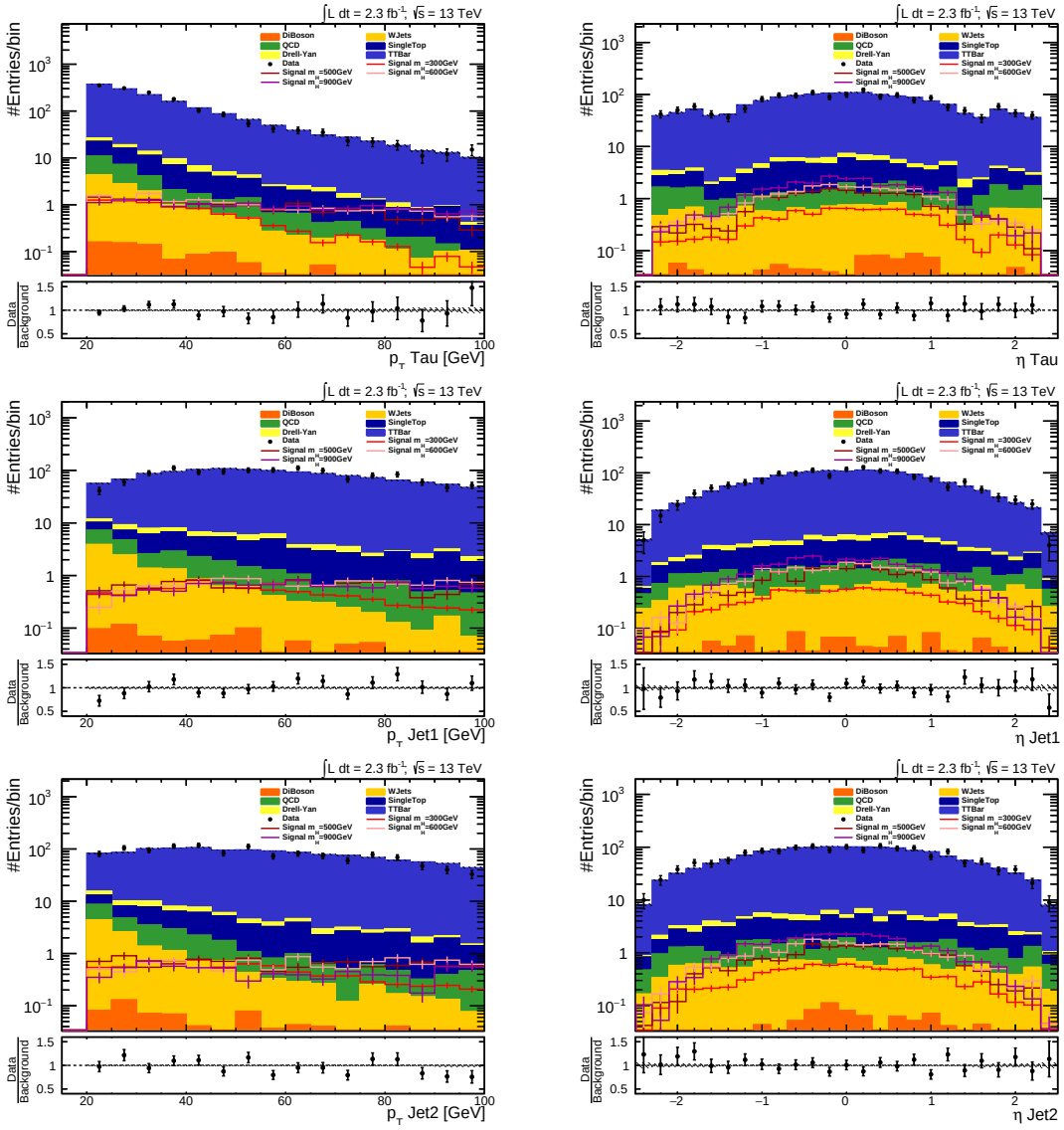

Figure 6.11: Control plots after preselection for data and background estimation. All signals are scaled to $\sigma \cdot BR = 10\,\text{pb}$. The plots show the transverse momentum (left) and the pseudorapidity (right) for the hadronic tau (top), the jet with the highest CSV value (middle) and the jet with the second highest CSV value (bottom) for events in the $n_{b-jets} \geq 2$ events category.

6.6 Cut Optimization Study

The analysis presented in [1], to which I contributided by providing a former version of the kinematic fitting tool presented in Chapter 5 [85], had a similar preselection than what is presented in Section 6.2 but included an $m_T < 30\,\text{GeV}$ requirement that was a remnant of the SM h$\rightarrow \tau\tau$ analysis meant to suppress the W+jets background. As the W+jets background is of lesser importance in the most sensitive $n_{b-jets} \geq 2$ event category, the sensitivity of this analysis might increase with a loosened cut on this observable. Besides the cut on the transverse mass, the 8 TeV analysis featured a mass-window cut on the invariant mass of the di-jet system and the SVfit mass. No cut on the fit probability of the HHKinFit was applied.

To maximize the sensitivity of this analysis, a cut optimization study has been performed by looking at possible cuts and the effect of the cuts on the significance of a signal assuming a specific heavy Higgs mass. The observables studied are the fit probability of the HHKinFit, the transverse mass, the invariant masses of the di-jet system and the SVFit mass. Other observables, like angular distributions and invariant masses of several combinations of b-jets, missing transverse energy and visible tau decay products in the event, were tested as well, but as the above named observables were found to be the most promising, no further studies on them are presented here.

Correlations between all observables considered during the cut optimization study were analyzed. Differences in the correlations between signal and background events are of special interest for the cut optimization as these could be used to further improve the sensitivity by applying non-orthogonal cutc. While some observables, like for example the fit probability and the invariant mass of the di-jet system, were correlated, no differences in correlation between background and signal events were observed. Correlations between some chosen observables at specific stages of the cut optimization can be found in Appendix A.2.

Before studying other observables a requirement on the convergence code of the kinematic fit, as defined by Tab. 5.1, is applied. The convergence codes for events in the $n_{b-jets} \geq 2$ category are shown in Fig. 6.12. The requirement of convergence code > 0 discards all event that did either not converge or have no solution for the di-tau system within the limits set for the tau energies. This cut discards less than 1% of events for each signal sample (0% for a signal sample with a generated heavy Higgs mass of 300 GeV and $\approx 0.7\%$ for a signal with a generated heavy Higgs mass of 900 GeV). Approximately 17% of all background events, predominantely $t\bar{t}$ events, are discared. Non-convergence only happens for one event of the $t\bar{t}$ simulation. After applying the cut, the fit probability for all remaining events is well defined. The significances of cuts on other observables is studied and compared to find the observable on which a cut yields the highest increase

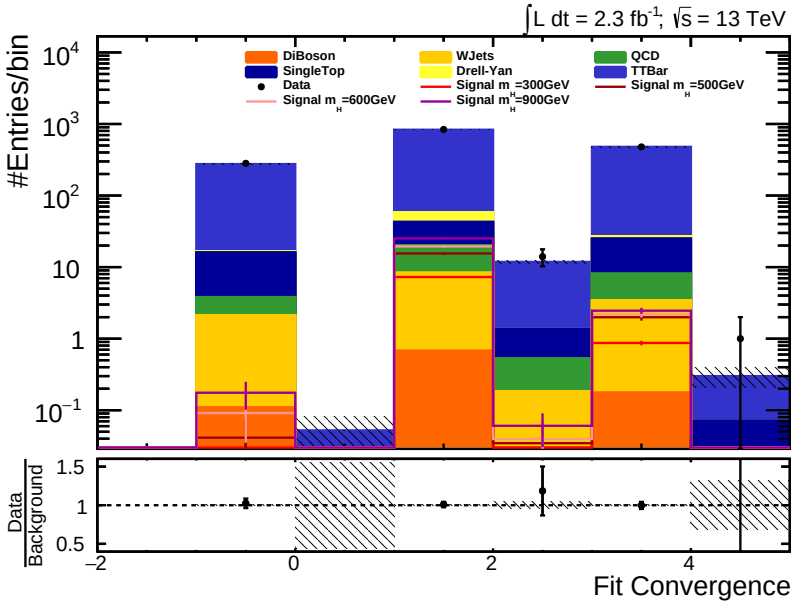

Figure 6.12: Convergence codes of the HHKinFit for events in the $n_{b-jets} \geq 2$ category. All signals are scaled to $\sigma \cdot BR = 10\,\text{pb}$.

in significance. To estimate the significance a likelihood ratio based estimator given by

$$m = \sqrt{2N \ln\left(\frac{S}{B} + 1\right) - 2S}, \tag{6.4}$$

where S is the number of signal events, B is the number of background events and $N = S + B$ is the number of events observed given that a signal is present. This significance estimator has been shown [86] to be closer to the true significance than the more commonly used estimator $m = \frac{S}{\sqrt{S+B}}$ if the number of background events is small.

Fig. 6.13 shows the heavy Higgs masses reconstructed by the kinematic fit for events with at least two b-jets. This observable will be used as the final observable to search for a possible signal and to set exclusion limits if no excess in data is observed. As the background composition and the ratio of background to signal events changes with the heavy Higgs mass reconstructed by the fit, the significance optimization is done for four individual signal masses of 300, 500, 600 and 900 GeV. Before optimizing the significance of a given signal mass, a requirement on the heavy Higgs mass reconstructed by the kinematic fit is applied. The requirement on the heavy Higgs mass roughly corresponds to a $\pm 2\sigma$ window around the given signal mass with σ being the resolution of the reconstructed mass for the respective signal:

- $290\,\text{GeV} < m_H < 310\,\text{GeV}$ for $m_{H,signal} = 300\,\text{GeV}$.
- $470\,\text{GeV} < m_H < 530\,\text{GeV}$ for $m_{H,signal} = 500\,\text{GeV}$.
- $560\,\text{GeV} < m_H < 640\,\text{GeV}$ for $m_{H,signal} = 600\,\text{GeV}$.

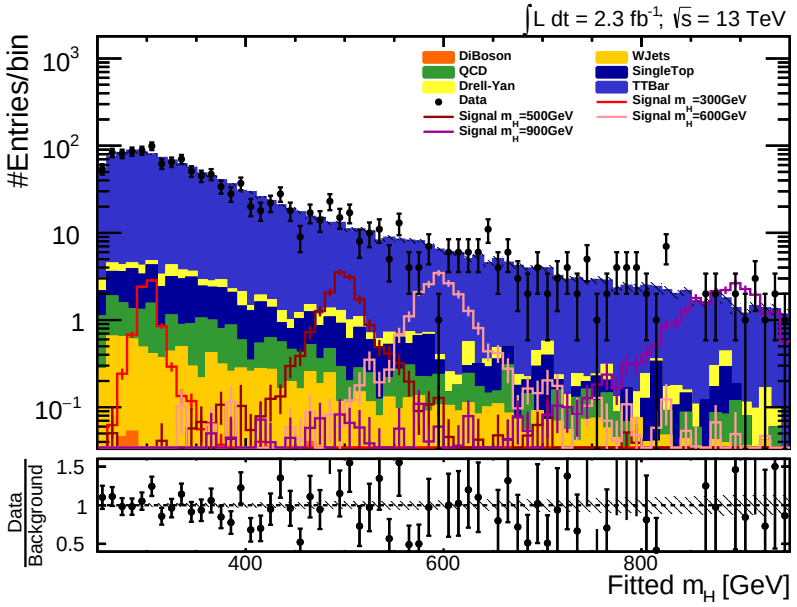

Figure 6.13: Heavy Higgs masses reconstructed by the kinematic fit for events with at least two b-jets. All signals are scaled to $\sigma \cdot BR = 10\,\text{pb}$.

- $840\,\text{GeV} < m_H < 960\,\text{GeV}$ for $m_{H,signal} = 900\,\text{GeV}$.

Figure 6.14 shows the significance that can be gained by applying a cut on the transverse mass, the fit probability, the invariant di-jet mass or the SVfit mass. All signals are scaled to $\sigma \cdot BR = 1\,\text{pb}$. For the fit probability, events with a fit probability lower than a given value are discarded. For the transverse mass, events in which the transverse mass exceeds a given value are discarded. For the invariant mass of the di-jet system $m_{\text{inv}}(\text{jet}_1, \text{jet}_2)$ and the SVfit mass m_{SVfit} the significance for a cut on a mass window is shown, where the lower and upper cut value are given by the x- and y-axis respectively.

The highest significance gain can be achieved by a cut on the fit probability. The fit probability for a simulated heavy Higgs mass of 300 GeV is shown in Fig. 6.15, while the corresponding significance after applying a cut on the fit probability can be seen in the top right plot of Fig. 6.14. For reasons of visibility, the signal in Fig. 6.15 is scaled up by a factor of 50. The cut value has been chosen as the loosest value after the significance reaches a plateau.

A cut on the fit probability gives the highest increase in significance for all studied signal masses, however, the optimal cut value shifts with the heavy Higgs mass of the signal. As the ratio of background to signal processes becomes smaller with increasing heavy Higgs mass, the optimal cut value shifts to smaller values to retain more signal events.

For a simulated heavy Higgs mass of 300 and 500 GeV the optimal cut value remains constant at fit probability greater than 0.2. For higher simulated heavy Higgs mass values of 600 and 900 GeV the optimal cut values falls to fit probability greater than 0.1 and fit probability greater than 0.025 respectively. As a consequence of this behavior, a shifting cut value depending on the reconstructed heavy Higgs mass of the event is

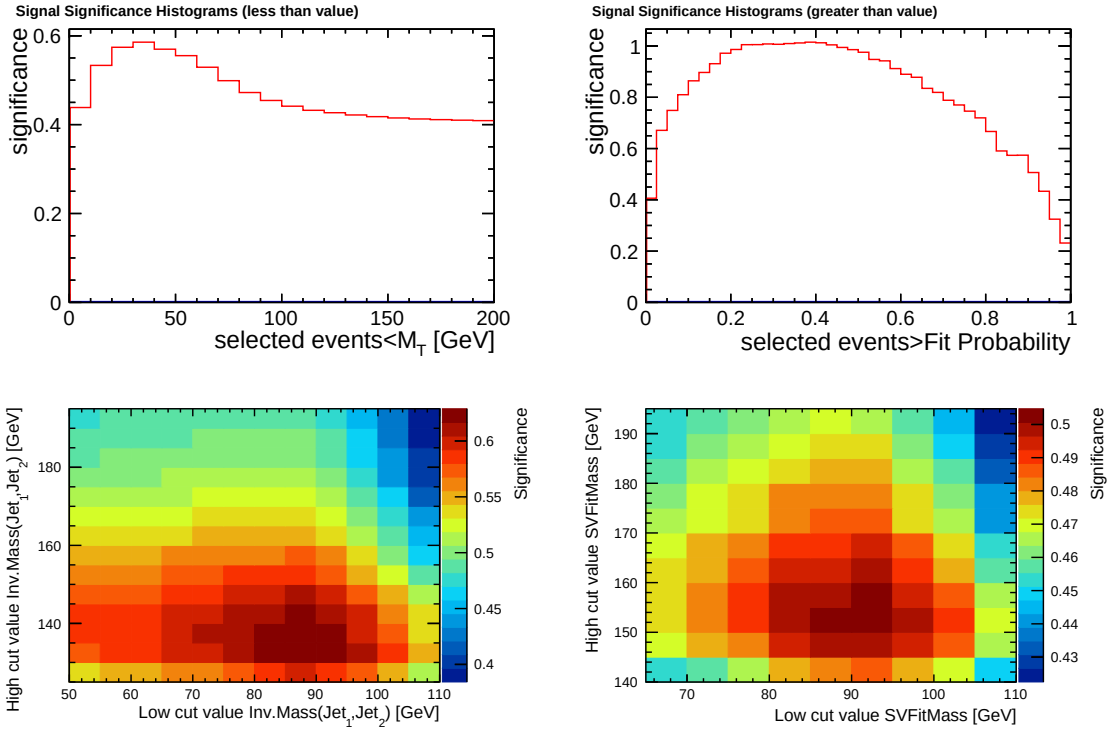

Figure 6.14: Significance that can be achieved by applying a cut on the transverse mass (top left), the fit probability (top right), the invariant di-jet mass (bottom left) or the SVfit mass (bottom right). All signals are scaled to $\sigma \cdot BR = 1\,\text{pb}$. For the fit probability, events with a fit probability lower than a given value are discarded. For the transverse mass, events in which the transverse mass exceed a given value are discarded. For the invariant mass of the di-jet system and the SVfit mass the significance for a cut on a mass window is shown, where the lower and upper cut value are given by the x- and y-axis respectively.

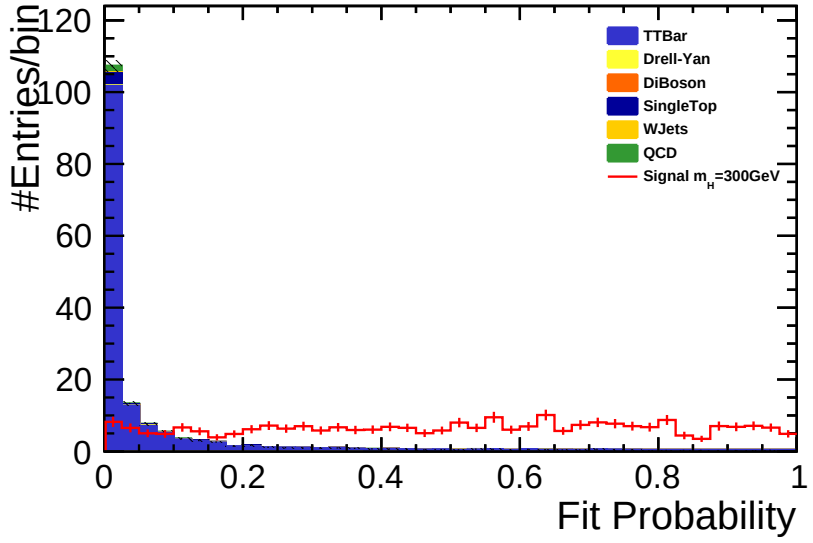

Figure 6.15: Fit probability for a simulated heavy Higgs mass of 300 GeV. For reasons of visibility, the signal is scaled up by a factor of 50.

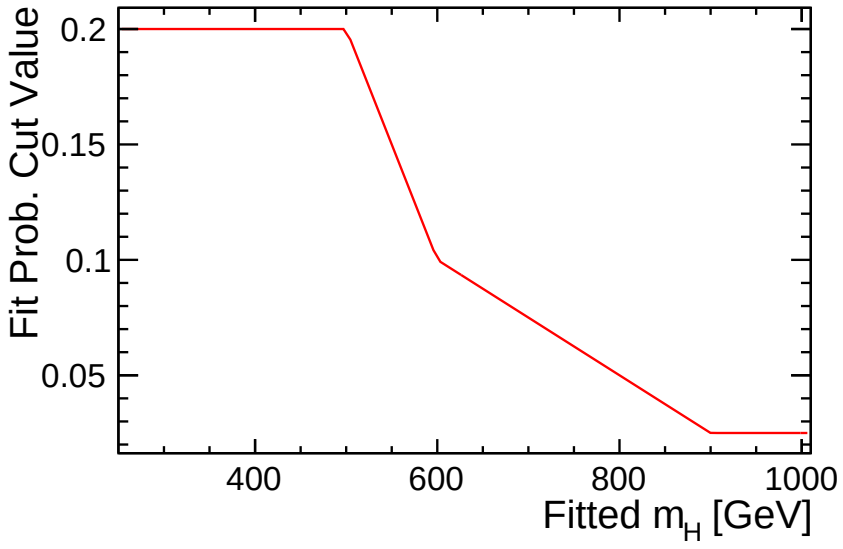

Figure 6.16: Fit probability cut value as a function of the heavy Higgs mass reconstructed by the kinematic fit.

applied. Events for which the kinematic fit reconstructed the heavy Higgs mass at one of the analyzed signal masses of $300, 500, 600$ or $900\,\text{GeV}$, will use the optimal cut value found for that signal mass. The cut values between the found optimal values are approximated by linear functions between each pair of mass points. The resulting cut value function is depicted in Fig. 6.16.

Fig. 6.17 shows the invariant di-jet mass for events in the $300\,\text{GeV}$ (left) and $900\,\text{GeV}$ (right) heavy Higgs mass window after a cut on the fit probability is applied. For background events with a fitted heavy Higgs mass within the $900\,\text{GeV}$ mass window, the invariant di-jet mass tends to values far lower than for any signal event generated with a heavy Higgs mass of $m_H = 900\,\text{GeV}$. Backgrounds events with a low invariant di-jet mass are more likely to have a high heavy Higgs mass as the kinematic fit adds a relatively large amount of artificial energy to the event to fulfill the Higgs-boson mass requirement on the invariant di-jet mass. A loose cut of $m_{\text{inv}}(\text{jet}_1, \text{jet}_2) > 70\,\text{GeV}$, which discards almost no signal events for any of the simulated signal masses, is applied.

The next best cut to maximize the sensitivity of the analysis is a cut on the transverse mass. In Fig. 6.18 the transverse mass for events in the $300\,\text{GeV}$ (left) and $900\,\text{GeV}$ (right) heavy Higgs mass window (after all above mentioned cuts) are shown. For all simulated signal masses the cut value that maximizes the significance is at $m_T < 60\,\text{GeV}$. However, as for high heavy Higgs masses almost no background events are left, even before applying a cut on the transverse mass, expected limits will be compared for a selection with and without a requirement on the transverse mass to test which cut variant will yield the best limit. For low signal masses, the significance can be improved further by applying additional cuts on the SVfit mass and the invariant di-jet mass. The

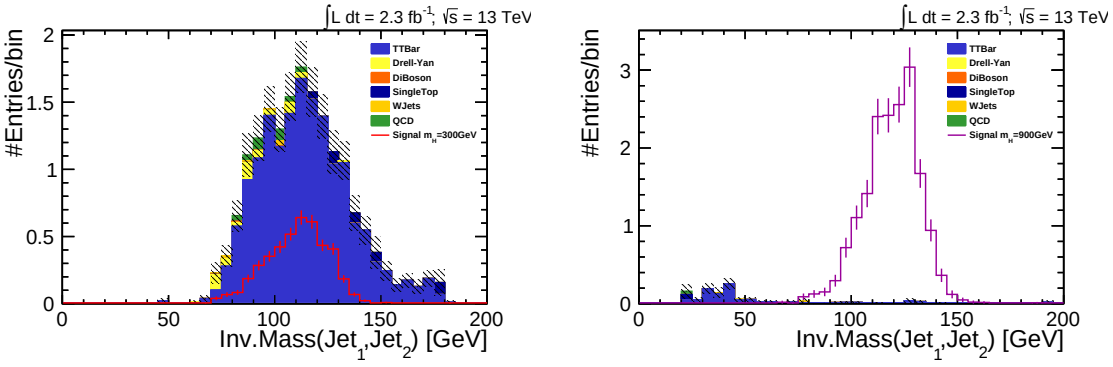

Figure 6.17: Invariant di-jet mass for events in the 300 GeV (left) and 900 GeV (right) heavy Higgs mass window after a cut on the fit probability is applied. All signals are scaled to $\sigma \cdot BR = 10\,\text{pb}$.

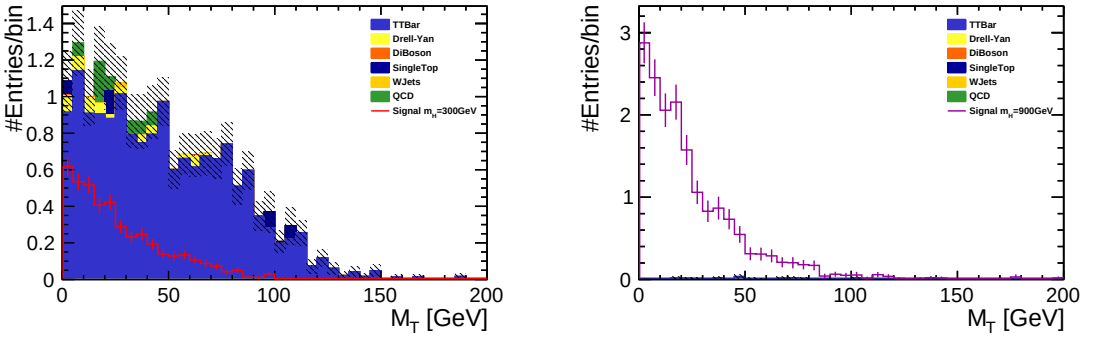

Figure 6.18: Transverse mass for events in the 300 GeV (left) and 900 GeV (right) heavy Higgs mass window after a cut on the fit probability and a lower cut on the invariant di-jet mass have been applied. All signals are scaled to $\sigma \cdot BR = 10\,\text{pb}$.

di-jet mass and SVfit mass for events in the 300 GeV heavy Higgs mass window after all aforementioned cuts have been applied are shown in Fig. 6.19. For the 300 GeV signal sample, the optimal mass windows are 70 GeV $< m_{\text{inv}}(\text{jet}_1, \text{jet}_2) <$ 145 GeV and 70 GeV $< m_{\text{SVfit}} <$ 160 GeV. Again, expected limits will be compared with and without the two aforementioned mass window cuts, to study for which simulated heavy Higgs masses these cuts will result in an actual improvement of the limit.

Fig. 6.20 shows the heavy Higgs mass distribution after all cuts have been applied. Comparing this to Fig. 6.13, it is obvious that a large increase in sensitivity was obtained by applying the cuts. The same cut optimization study was conducted for events in the $n_{b-jets} = 1$ event category. As the siginificance values that are reached in this events category are 50% smaller in the low heavy Higgs mass range around 300 GeV and 25% smaller in the very high mass region at 900 GeV, no further evaluation of events in the $n_{b-jets} = 1$ category is pursued.

To identify the optimal cut scenario for each signal mass and to quantify the gain in sensitivity with respect to former analysis approaches, limits on the $\sigma \cdot BR$ of the H $\rightarrow$

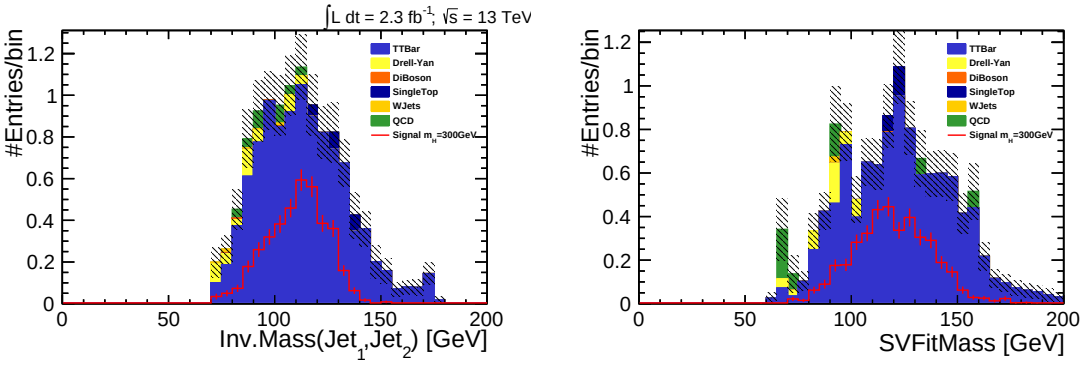

Figure 6.19: The di-jet mass (left) and SVfit mass (right) for events in the 300 GeV heavy Higgs mass window after cuts on the fit probability, the transverse mass and a lower cut on the invariant di-jet mass have been applied. All signals are scaled to $\sigma \cdot BR = 10\,\text{pb}$.

$hh \to b\bar{b}\tau^+\tau^-$ process will be calculated and compared in Section 6.8. The scenarios for which the expected limits will be compared are defined as follows: Events with a

Cut Scenario	$m_{\text{inv}}(\text{jet}_1, \text{jet}_2)$ [GeV]	m_{SVfit} [GeV]	m_T [GeV]	Fit Prob.
Scenario A:	> 70			See Fig. 6.16
Scenario B:	> 70		< 60	See Fig. 6.16
Scenario C:	$> 70 \wedge < 145$	$> 70 \wedge < 160$	< 60	See Fig. 6.16
8 **TeV Analysis:**	$> 70 \wedge < 150$	$> 90 \wedge < 150$	< 30	

Table 6.5: Different cut scenarios for the final event selection.

HHKinFit convergenve code of convergence ≤ 0 are excluded in all scenarios.
With this the cut optimization study is concluded with the decision on the exact cuts to apply postponed until the expected limits of all cut configurations are compared.

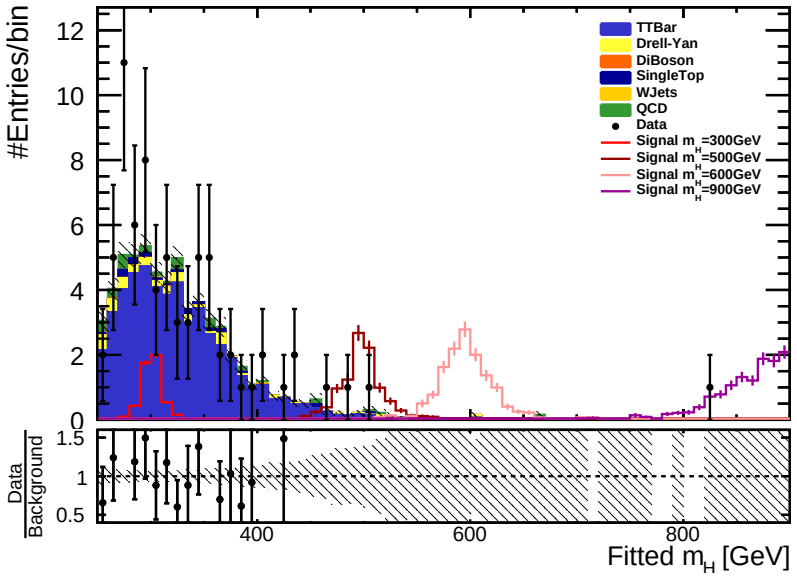

Figure 6.20: Heavy Higgs masses reconstructed by the kinematic fit for events with at least two b-jets. All signals are scaled to $\sigma \cdot BR = 10\,\text{pb}$.

6.7 Uncertainties

Before limits can be set, uncertainties on the predicted background in shape and scale have to be quantified. In the following, all considered uncertainties are listed.

6.7.1 Scale Uncertainties

- **Luminosity:** The instantaneous luminosity can be measured by measuring the activity recorded in the hadronic forward calorimeter. For this to be possible, the hadronic forward calorimeter measurement is calibrated with a known luminosity. This luminosity is derived by calculating it from the beam parameters, where the size of the beams at the collision point is measured via a Van-der-Meer scan. This procedure has an uncertainty of 2.6% which is propagated as a scale uncertainty to the $t\bar{t}$, Drell-Yan, single top and di-boson backgrounds. The W+jets and QCD background are not affected by this uncertainty as there scales are derived directly from data.

- **$t\bar{t}$ cross section:** The $t\bar{t}$ cross section is derived from NNLO calculations for a top mass of 172.5 GeV. It was found to be $(831.76^{+40.25}_{-45.63})$pb. The uncertainty of the cross section is applied as a scale uncertainty to the $t\bar{t}$ background.

- **Further cross section uncertainties:** Cross section uncertainties for other backgrounds are of lesser importance, but are also considered. All cross sections are taken from NNLO theory calculations. The cross section uncertainties for the

single top and Drell-Yan background are 4.8% and 3.7% respectively. For reasons of simplification, all di-boson backgrounds are combined and a conservative combined cross section uncertainty of 5% is assigned.

- **Muon Efficiency:** The uncertainties of the Monte Carlo-to-data scale factors of the muon isolation, identification and trigger efficiency are combined in quadrature to give a scale uncertainty of 2%. The uncertainty is applied to all backgrounds with a scale not derived from data.

- **Hadronic Tau Efficiency:** The hadronic tau efficiency was measured during the 8 TeV data-taking period and was found to be 6%. The value recommended by the tau POG for 13 TeV analyses sticks to this value of 6% and it is therefore applied as a scale uncertainty to all backgrounds with a scale not derived from data.

- **QCD Yield:** The uncertainty on the normalisation of the QCD background is derived by propagating the statistical errors of all samples used to estimate the normalisation (See Section 6.5.4). In the event category requiring at least two b-jets, this uncertainty was found to be 64%.

- **W+Jets Yield:** Like in the case of the QCD yield, the uncertainty on the scale of the W+jets background is derived by propagating the statistical errors of all samples used. In the event category requiring at least two b-jets, this uncertainty was found to be 182%. The driving contribution to this high uncertainty is the proportionally high statistical uncertainty on the small number of W+jets event in data, obtained by deducting the known backgrounds in the control region. Note however, that the W+jets background amounts to only 0.9% of the total background.

6.7.2 Shape Uncertainties

- **Jet Energy Scale:** The jet energy scale correction, that should correct the jet response towards unity, has an uncertainty. To account for this uncertainty the analysis is performed once for all jets shifted up by the jet energy scale uncertainty propagated to the jet energy, and once after shifting all jets down. The change in jet energy is also propagated to the missing transverse energy

$$\vec{E}_{T,miss,JES-shifted} = \vec{E}_{T,miss} + \sum_{alljets} \vec{p}_T - \sum_{alljets} \vec{p}_{T,shifted}. \tag{6.5}$$

  As the missing transverse energy is derived by a multivariate approach in which jets contribute with differing weights to the total missing transverse energy, this is only a conservative approximation of the propagated JES uncertainty. The approximation is assumed to be conservative, as jets will not contribute with weights

larger than 1 to the missing transverse energy derived by the multivariate algorithm. This means that on average the true shift to the missing transverse energy will be smaller than the shift propagated by Eq. 6.5. The JES uncertainty is also propagated to the CSV-shape reweighting factors by applying reweighting factors that have been derived on JES shifted samples by the b-jet POG.

- **CSV Shape Reweighting:** The CSV-shape reweighting method introduced in Section 6.4 has multiple sources of uncertainties. In total 8 uncertainties derived by the b-jet POG are propagated as a shape uncertainty. The uncertainties include a light flavor contamination and heavy flavor contamination uncertainty plus several statistical uncertainties from the samples used to derive the correction factors.

6.8 Results

As no excess in the final distribution of the reconstructed heavy Higgs mass, shown in Fig. 6.20, is observed, limits on the $\sigma \cdot BR$ of the $H \to hh \to b\bar{b}\tau^+\tau^-$ process will be set. The method used to calculate the limits is presented in [87]. It is a common method used by both, the CMS and ATLAS experiment. It was developed by the LHC Higgs Combination group.
The method is based on a modified frequentist approach [88] and is often referred to as CL_s. The binned distribution of the heavy Higgs mass as reconstructed by the kinematic fit is used to assess the compatibility of the data with the background-only and the background-plus-signal hypotheses. The compatibility can be quantified by the likelihood given by:

$$\mathcal{L} = \text{Poisson}(data|\mu \cdot s(\theta) + b(\theta)) \cdot \prod_j p(\tilde{\theta_j}|\theta_j). \tag{6.6}$$

$s(\theta)$ and $b(\theta)$ are the number of expected background events given a set of nuisance parameters θ. The nuisance parameters are the parameters that have an assigned systematic uncertainty described in Section 6.7. The parameter μ is known as the signal strength modifier. In the following interpretation μ will be defined as the branching ratio times cross section of the signal. For the likelihood of the background hypothesis, μ is set to zero.
$\text{Poisson}(data|\mu \cdot s(\theta) + b(\theta))$ is given by:

$$\text{Poisson}(data|\mu \cdot s(\theta) + b(\theta)) = \prod_i \frac{(\mu s_i + b_i)^{n_i}}{n_i!} e^{-\mu s_i - b_i}, \tag{6.7}$$

where i is the number of bins and b_i, s_i and n_i are the number of background events, signal events and observed events, respectively.

$p(\tilde{\theta_j}|\theta_j)$ in Eq. 6.6 is the PDF for a nuisance parameter values $\tilde{\theta_j}$ as it was determined by an external measurements under the assumption of a true value of the nuisance parameter θ_j. If the nuisance parameter results in a scale uncertainty, the PDF is given by a log-normal distribution to prevent negative yields. In the case of a shape uncertainty, two templates are formed that represent the shape of an affected background or signal if the nuisance parameter is varied by $\pm 1\sigma$. The variation of the background is then given by smoothly interpolating between the nominal and the $\pm 1\sigma$ templates. A Gaussian PDF is assigned to the shape-nuisance parameters.
To compare the background-only and background-plus-signal hypotheses, a test statistic is defined based on the profile likelihood ratio:

$$\tilde{q}_\mu = -2 \ln \frac{\mathcal{L}(data|\mu, \hat{\theta}_\mu)}{\mathcal{L}(data|\hat{\mu}, \hat{\theta})}, \text{where } 0 \leq \hat{\mu} \leq \mu \tag{6.8}$$

Here $\hat{\theta}_\mu$ is the set of nuisance parameters, that maximizes the likelihood given a signal strength μ and the observed data. The parameters $\hat{\mu}$ and $\hat{\theta}$ are the parameters under which the likelihood reaches its global maximum. The constraints on $\hat{\mu}$ are introduced to prevent negative signal strengths ($0 \leq \hat{\mu}$) and to ensure that no signal smaller than a signal with a signal strength $\hat{\mu}$ is excluded ($\hat{\mu} \leq \mu$). As a result, the second constraint also guarantees a one-sided confidence interval. The PDFs for $\tilde{q}_\mu$ is denoted as $f(\tilde{q}_\mu|\mu, \hat{\theta}_\mu^{obs})$ for a possible signal with signal strength μ and as $f(\tilde{q}_\mu|0, \hat{\theta}_0^{obs})$ for the background-only hypotheses. To find the PDFs for $\tilde{q}_\mu$, sets of pseudo data (toys) are generated with the nuisance parameters fixed to $\hat{\theta}_\mu^{obs}$ for the background-plus-signal hypothesis and to $\hat{\theta}_0^{obs}$ for the background-only hypothesis. Each toy is sampled several times with the test statistic $\tilde{q}_\mu$ being evaluated while the nuisance parameters are randomly varied according to their respective PDFs.
The confidence level for the signal-plus-background hypothesis can then be defined as:

$$CL_{s+b} = \int_{q_\mu^{obs}}^{\infty} f(\tilde{q}_\mu|\mu, \hat{\theta}_\mu^{obs}) d\tilde{q}_\mu. \tag{6.9}$$

The confidence level for the background C_b is given by the same equation by setting $\mu = 0$. The confidence level for the signal is then given by

$$CL_s = \frac{CL_{s+b}}{CL_b} \tag{6.10}$$

To find the 95% confidence level upper limit, μ is varied until CL_s reaches a value of 0.05. Expected limits depending on the background-only hypothesis can be determined by the distribution of limits that can be set with the toys generated with the background-only hypothesis.
The generation of a large set of toys would need a lot of computational resources. For

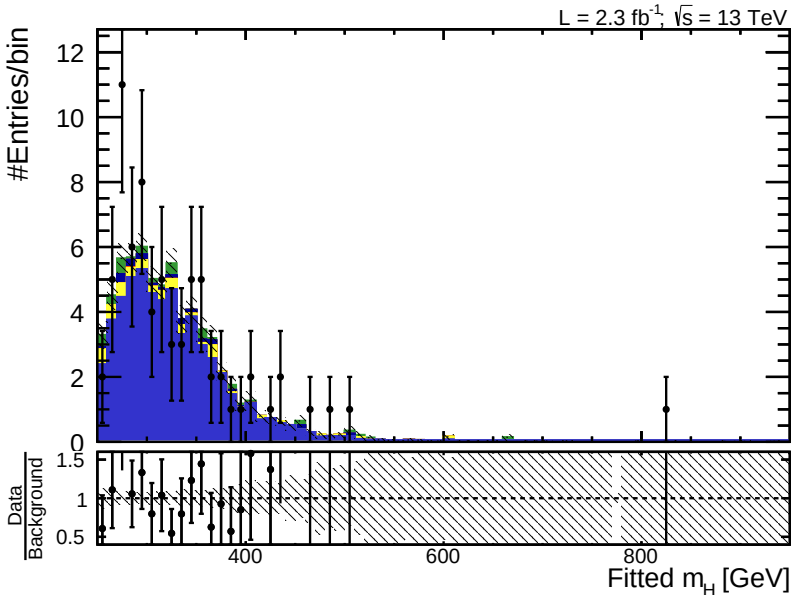

Figure 6.21: Heavy Higgs masses reconstructed by the kinematic fit after nuisance parameters are fitted to maximize the likelihood as given by Eq. 6.6 for the background-only hypothesis.

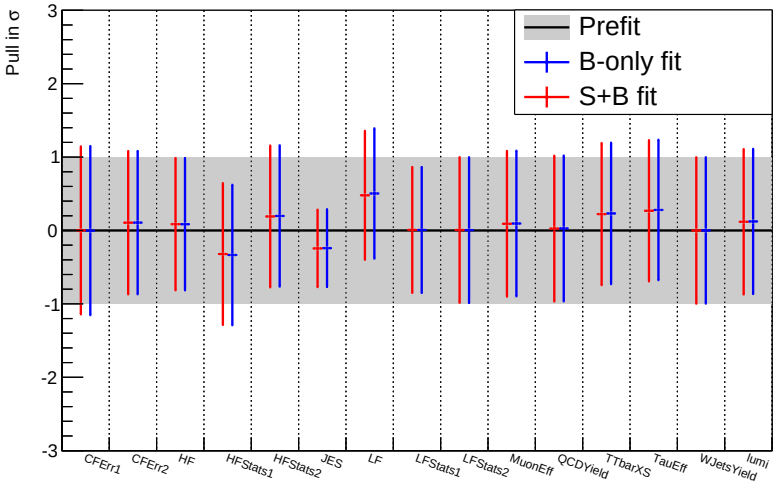

Figure 6.22: Pulls on the nuisance parameters after fitting with the background-only hypothesis (blue) and after fitting with the signal-plus-background hypothesis for a signal with a generated heavy Higgs mass of 300 GeV (red). JES denoted the nuisance parameter of the jet energy scale. The shape nuisance parameters CFErr1, CFErr2, HF, HFStats1, HFStats2, LF, LFStats1 and LFStats2 are the independent nuisance parameters of the CSV reshaping method.

large datasets the test statistic PDFs can be derived analytically. This is known as the asymptotic approximation [89]. By the same method, the median expected limit and its uncertainties can be derived so that no toys have to be generated.

Fig. 6.21 shows the distribution of the heavy Higgs mass reconstructed by the fit after the nuisance parameters are fitted to maximize the likelihood as given by Eq. 6.6 for the

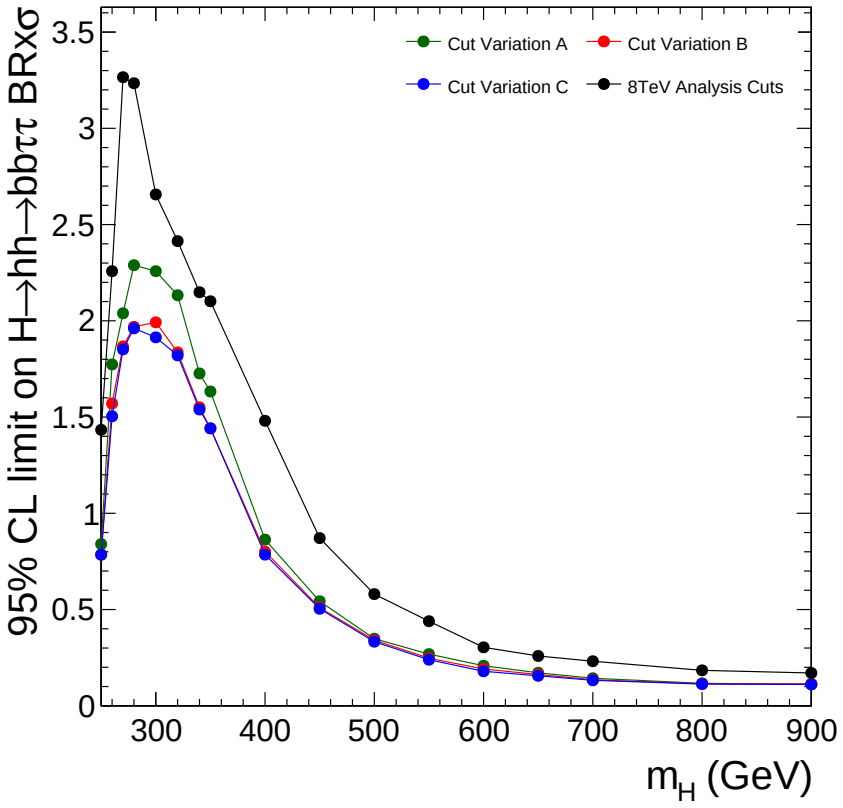

Figure 6.23: Expected limits for several cut scenarios considered after the cut optimization study and for using the same cuts as used in the analysis presented in [1]. The scenarios are defined in Tab. 6.5.

background-only hypothesis.

In Fig. 6.22 the pulls on the nuisance parameters is shown. All pulls are within one standard deviation of their value determined by an external measurement, confirming that indeed a rather conservative approximation was used. Note that especially the post-fit uncertainty for the JES is strongly reduced after the fit. This indicates, that the propagation of the JES-uncertainty to the missing transverse energy derived by the MVA algorithm as given by Eq. 6.5 was conservative, as expected.

In Fig. 6.23 the expected limits for several cut scenarios as defined in Tab. 6.5 are shown. The limit is given on the $\sigma \cdot BR$ of the process $H \to hh \to b\bar{b}\tau^+\tau^-$. Assuming a SM-like behavior for the light Higgs boson, the limit can be translated to a limit on the $\sigma \cdot BR$ of $H \to hh$ by multiplying it by a factor of roughly 13.7.

As can be seen in Fig. 6.23, the differences between all cut scenarios becomes very small at high masses due to the drastically reduced backgrounds. Depending on the signal mass, the cut optimization improved the limit significantly by approximately 40% to 30% with respect to the 8 TeV analysis cut variant. Cut scenario C yields the best limit for all signal masses. Scenario B gives very similar results, the differene beeing the

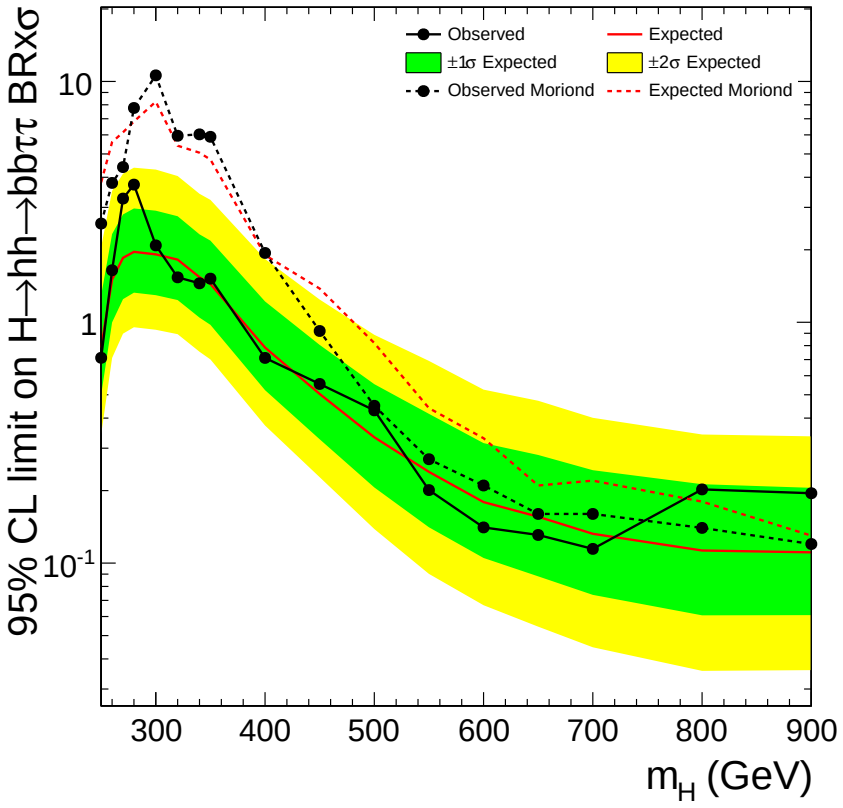

Figure 6.24: Observed limits together with the expected limit and its uncertainty bands after applying cut variant C. The dashed black and red line labeled Moriond show the expected and observed limits for a comparable analysis presented in [2] in the $\mu - \tau_h$ channel.

usage of SVFit. Therefore no additional cut variation for higher masses is applied. The final observed limits together with the expected limit and its uncertainty bands is shown in Fig. 6.24. The observed limit is in agreement with the expected limit. The deviation of almost two sigma for heavy Higgs mass of 270 and 280 GeV can be attributed to the excess in one of the bins in that mass range, visible in Fig. 6.21. The dashed black and red line depicted in Fig. 6.24 show the expected and observed limit for a comparable analysis presented in [2] in the $\mu-\tau_h$ channel. The analysis used a slightly larger dataset of 2.7 fb^{-1} of 13 TeV data recorded by the CMS experiment, by including events from a running period in which the forward hadronic calorimeter was not operational. The heavy Higgs mass as reconstructed by HHKinFit was used to set limits. However, no cut on the transverse mass or the fit probability was applied. The limit given by the analysis presented in this thesis improves the limit by a factor of 2 to 4 with respect to the limit in the $\mu - \tau_h$ channel presented in [2].

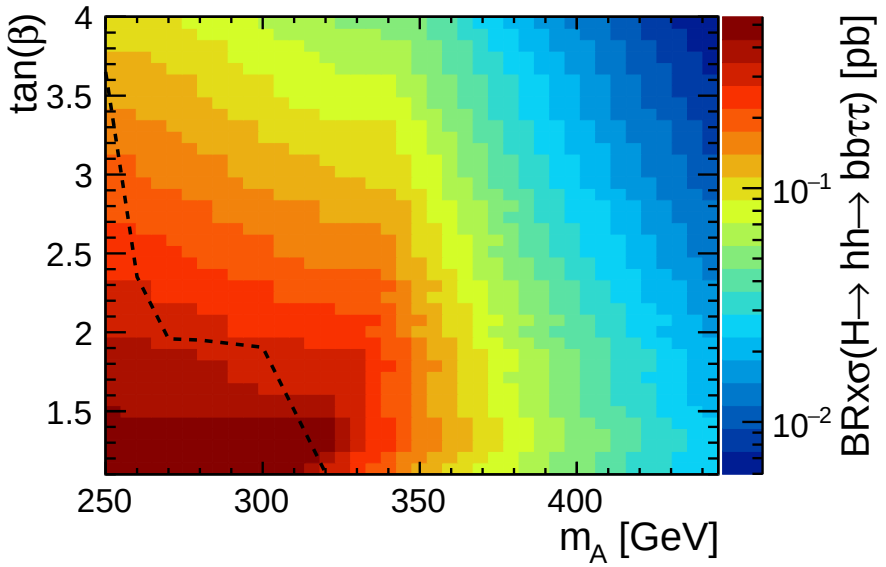

Figure 6.25: Projected exclusion limit within the $\tan\beta - m_A$ parameter space of the hMSSM for a projection of the results to an integrated luminosity of $100\,\text{fb}^{-1}$ at a center-of-mass energy of $\sqrt{s} = 13\,\text{TeV}$. The cross sections and branching ratios provided by the LHC cross section working group [29] were calculated using HDECAY [30, 31]. The region below the dashed line can be excluded at 95% CL.

6.9 Interpretation

The results of the analysis are interpreted in the hMSSM and the non-alignment 2HDM for $\cos(\beta - \alpha)$ values of 0.02 and 0.05 as introduced in Sec. 2.4.1 and Sec. 2.4.2, respectively. As the amount of data collected in 2015 is very limited and therefore the limits in the decay channel with one muon and one hadronic tau are too weak to exclude parts of the given parameter spaces, the excluded areas for a projected expected limit at $100\,\text{fb}^{-1}$ will be shown. The relative systematic uncertainties are not changed. While the uncertainties for the backgrounds taken directly from MC simulation do not necessarily decrease for the next running periods, as the uncertainties only depend on the number of generated events, the uncertainties for the data-driven QCD and W+Jets backgrounds will go down as more data is analyzed. The projection presented in the following does not account for this effect, however as the QCD and W+Jets background are minor backgrounds compared to the background resulting from top-quark pair production, the effect is assumed to be small. Not accounting for this effect will however mean that the projection is a conservative result. Furthermore, several other systematic uncertainties might decrease with time and the amount of data collected as the understanding of the behavior of the experiment becomes even better, which again renders the presented projections conservative. The Cut optimisation was not repeated after scaling to an integrated luminosity of $100\,\text{fb}^{-1}$.

Fig. 6.25 shows the projected exclusion limit within the $\tan\beta - m_A$ parameter space of

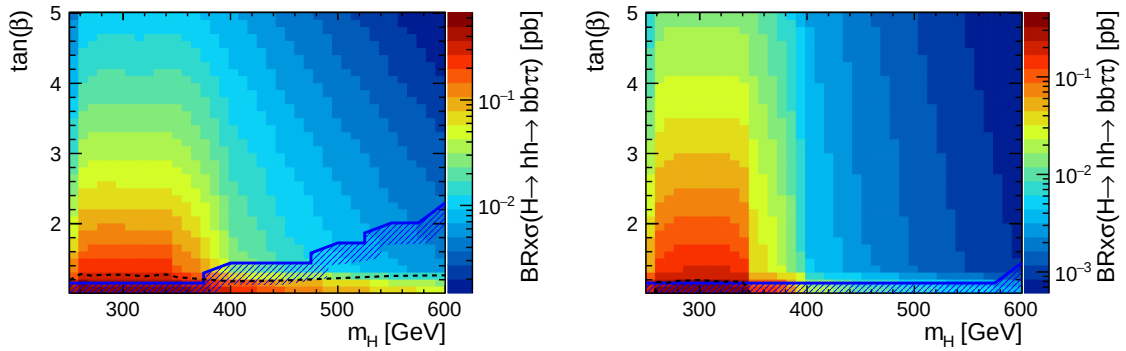

Figure 6.26: Projected exclusion limits within the $\tan\beta - m_H$ parameter space of the non-alignment 2HDM model with $\cos(\beta - \alpha)$ set to 0.05 (left) and 0.02 (right). The expected limits are a projection of the results to an integrated luminosity of $100\,\text{fb}^{-1}$ at a center-of-mass energy of $\sqrt{s} = 13\,\text{TeV}$. The area enclosed by the blue line is excluded due to stability constraints of the Higgs potential at the input scale. The cross sections and BRs have been calculated using SusHi and 2HDMC [38–46].

the hMSSM for a projection of the results to an integrated luminosity of $100\,\text{fb}^{-1}$ at a center-of-mass energy of $\sqrt{s} = 13\,\text{TeV}$. The cross sections and branching ratios provided by the LHC cross section working group [29] were calculated using HDECAY [30, 31]. For m_A values close to $m_A = 250\,\text{GeV}$, $\tan\beta$ values of up to 3.5 are excluded due to the stronger limit at these mass values. For higher values of m_A, as the background from top-quark pair production reaches its peak, the limit becomes weaker and reaches a plateau at values of $\tan\beta \approx 2$ before falling off to zero as the decay of the heavy Higgs boson to top-quarks becomes kinematically available and the branching ratio H→hh falls off.

In Fig. 6.26 the projected exclusion limits within the $\tan\beta - m_H$ parameter space of the non-alignment 2HDM model with $\cos(\beta - \alpha)$ set to 0.05 (left) and 0.02 (right) is shown. The expected limits are a projection of the results to an integrated luminosity of $100\,\text{fb}^{-1}$ at a center-of-mass energy of $\sqrt{s} = 13\,\text{TeV}$. The area enclosed by the blue line is excluded due to stability constraints of the Higgs potential at the input scale. The cross sections and BRs have been calculated using SusHi and 2HDMC [38–46]. The area of phase space that is excluded by the projected limit that is not already excluded due to the stability constraints is rather small. As in the case of the hMSSM, the excluded area is mostly constraint to the parts of the parameter space, where the decay of the heavy Higgs boson to top-quark pairs is kinematically not available.

The model-independent cross section limits are the most important result of this analysis as this allows to test any arbitrary model against data. The applied analysis technique led to an improvement of the limits of roughly a factor of 2-4 with respect to a parrallel analysis carried out on the 13 TeV data collected in 2015 presented in [2]. Furthermore, an improvement with respect to applying the analysis strategy used for the 8 TeV analysis [1] to the 13 TeV data could be demonstrated. The limit falls short of the limit that

was achieved in the $\mu - \tau_h$ channel by the analysis presented in [1] as the integrated luminosity collected was smaller by a factor of 8.6. In addition as the ratio of the signal to background cross sections did not improve with the increased center-of-mass energy, as the cross section of the most dominant background from top-quark pair production went up by a relatively large factor of 3.2. The cross section for a heavy Higgs signal in the hMSSM with a mass of $m_H = 300\,\text{GeV}$ at $\tan\beta = 2.0$ only went up by a factor of 2.9.

Chapter 7

Conclusion

In this thesis, a search for a heavy Higgs boson decaying into two light Higgs bosons and the further into two b quarks and two tau leptons was presented. The analysis was originally developed as a search on 8 TeV data [1]. The emphasis in this thesis however is on proton-proton collision data with an integrated luminosity of $2.30\,\mathrm{fb}^{-1}$ and a center-of-mass energy of $\sqrt{s} = 13\,\mathrm{TeV}$ collected by the CMS experiment was analyzed.
A kinematic fitting tool for heavy Higgs bosons decaying to two light Higgs bosons (HHKinFit) was developed. HHKinFit makes use of the smal tau lepton mass and the by now well known mass of a Higgs boson at 125 GeV to constrain the tau lepton and b-jet momenta. The systematic studies presented in Chapter 5 have shown that the kinematic fit provides a well defined fit probability and that the fit is able to reconstruct the mass of the heavy Higgs boson with high precision.
The analysis presented in Chapter 5 searched for decays $\mathrm{H} \to \mathrm{hh} \to \mathrm{b\bar{b}}\tau^+\tau^-$ in which one of the tau leptons decays hadronically and the other into a muon. After a preselection requiring two jets and a τ_h/μ-pair with opposite charge is applied, a cut optimization study on several observables is performed to increase the sensitivity of the analysis. A cut on the fit probability is applied, where the cut value changes with the mass reconstructed by the kinematic fit. Further cuts are applied on the transverse mass, the invariant mass of the di-jet system and mass of the di-tau system obtained with the SVfit tool. The mass of the heavy Higgs boson reconstructed by the kinematic fit is used to search for an excess in data relative to the background from SM processes which has been deduced partially from NNLO calculations and partially from data.
As no excess was observed, model independent limits on the $\sigma \cdot BR$ of the $\mathrm{H} \to \mathrm{hh} \to \mathrm{b\bar{b}}\tau^{\pm}\tau^{\mp}$ process are set and interpreted within the hMSSM and two 2HDM non-alignment scenarios. The developed analysis technique was able to improve the sensitivity with respect to the analysis techniques applied in [2] for 13 TeV data and [1] for 8 TeV data significantly, however, mainly due to the limited amount of data collected in 2015 the limit falls short of the limit reached by the analysis presented in [1].

By extrapolating the expected limits to an integrated luminosity of $100\,\mathrm{fb}^{-1}$ is is shown, that the future reach of the analysis in the two models used for interpretation in this thesis is quite limited. However, other already known or not yet thought of models still might leave room for a heavy Higgs state coupling to the recently discovered Higgs boson, that is not yet excluded but in reach of future LHC analysis. Furthermore, getting a first grasp on triple Higgs self couplings by measuring the coupling properties after a possible discovery is a very appealing idea.
Going forward, still some options remain that could improve the sensitivity of the presented analysis. Two possibilities are the application of MVA techniques to further improve upon the cut optimization presented in Sec. 6.6 and the application of a kinematic fit dedicated to reconstructing top quark in top-quark pair production processes to further suppress the corresponding background.

Appendix A

Appendix

A.1 B-jet energy ratio PDFs and CDFs used for the HHKinFit

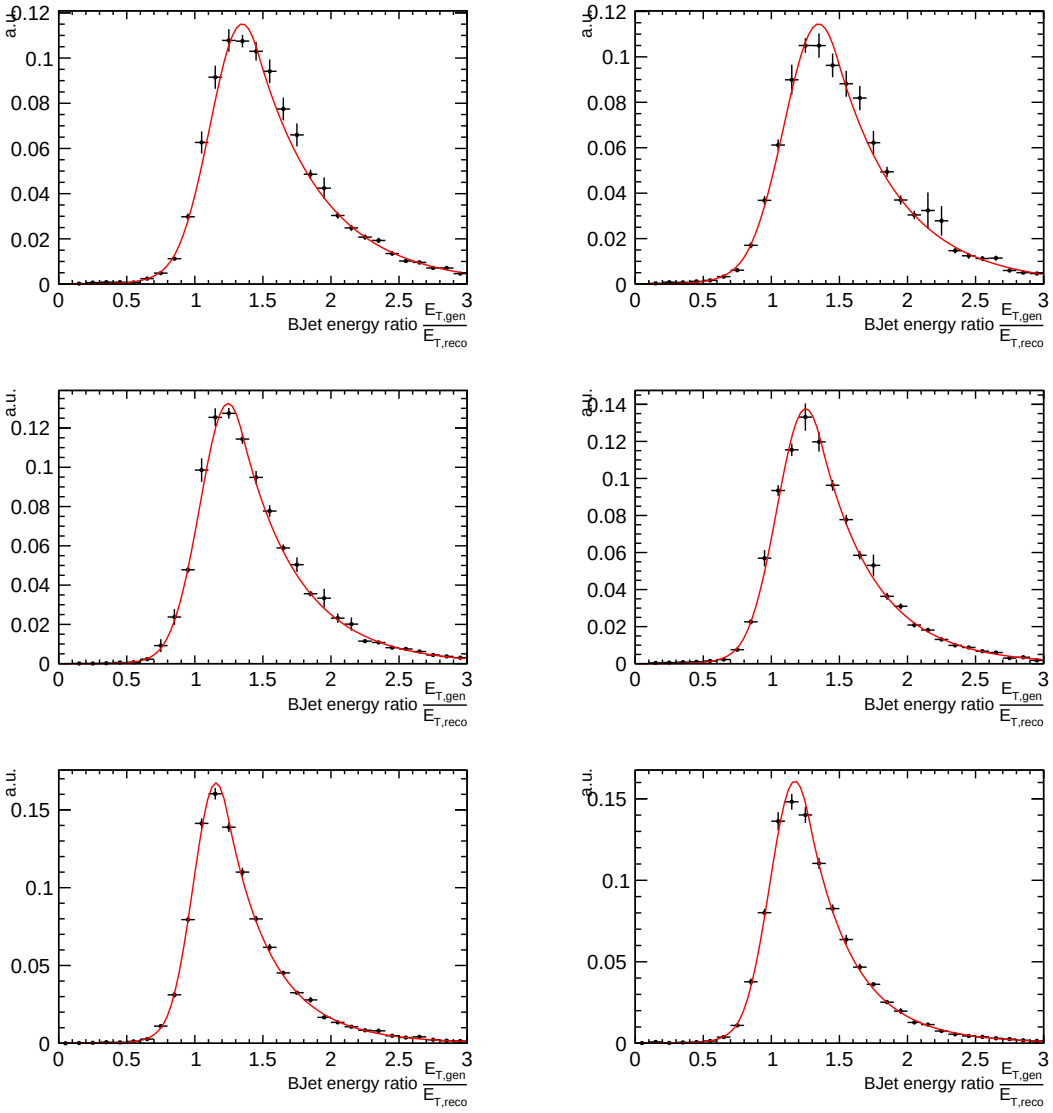

Figure A.1: Transverse b-jet-energy ratio $\frac{E_{\mathrm{T,gen}}}{E_{\mathrm{T,reco}}}$ fitted by a two-tailed crystal-ball function (Eq. 5.18) shown in red on a signal sample with a heavy Higgs boson mass of 300 GeV. The ratios are shown for jets with $|\eta| < 1.2$ (left) and $|\eta| \geq 1.2$ (right). The E_{T} range of the jets are $E_{\mathrm{T}} < 25\,\mathrm{GeV}$ (top), $25\,\mathrm{GeV} < E_{\mathrm{T}} < 30\,\mathrm{GeV}$ (middle), $30\,\mathrm{GeV} < E_{\mathrm{T}} < 40\,\mathrm{GeV}$ (bottom).

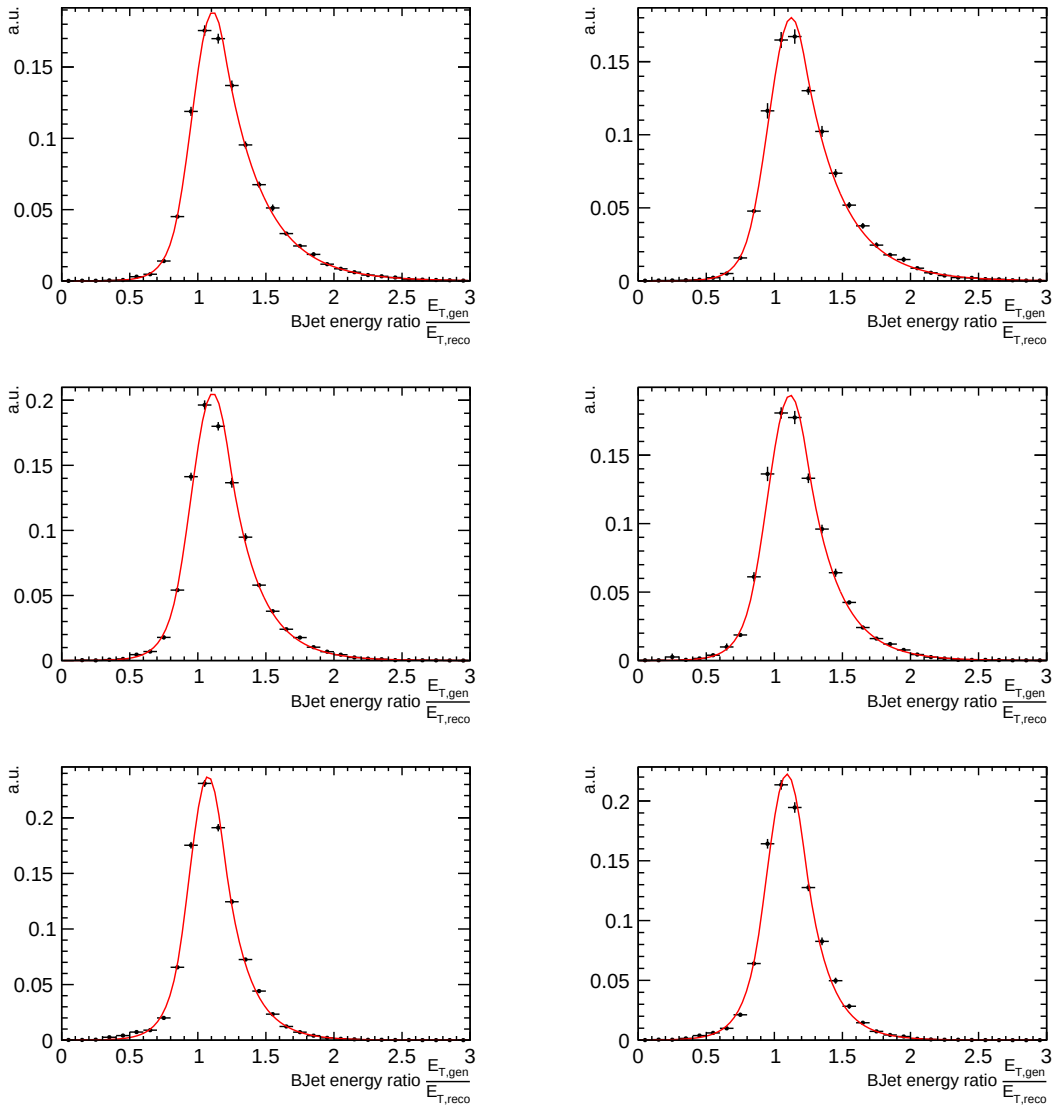

Figure A.2: Transverse b-jet-energy ratio $\frac{E_{\mathrm{T,gen}}}{E_{\mathrm{T,reco}}}$ fitted by a two-tailed crystal-ball function (Eq. 5.18) shown in red on a signal sample with a heavy Higgs boson mass of 300 GeV. The ratios are shown for jets with $|\eta| < 1.2$ (left) and $|\eta| \geq 1.2$ (right). The E_{T} range of the jets are $40\,\mathrm{GeV} < E_{\mathrm{T}} < 50\,\mathrm{GeV}$ (top), $50\,\mathrm{GeV} < E_{\mathrm{T}} < 60\,\mathrm{GeV}$ (middle) and $60\,\mathrm{GeV} < E_{\mathrm{T}} < 80\,\mathrm{GeV}$ (bottom).

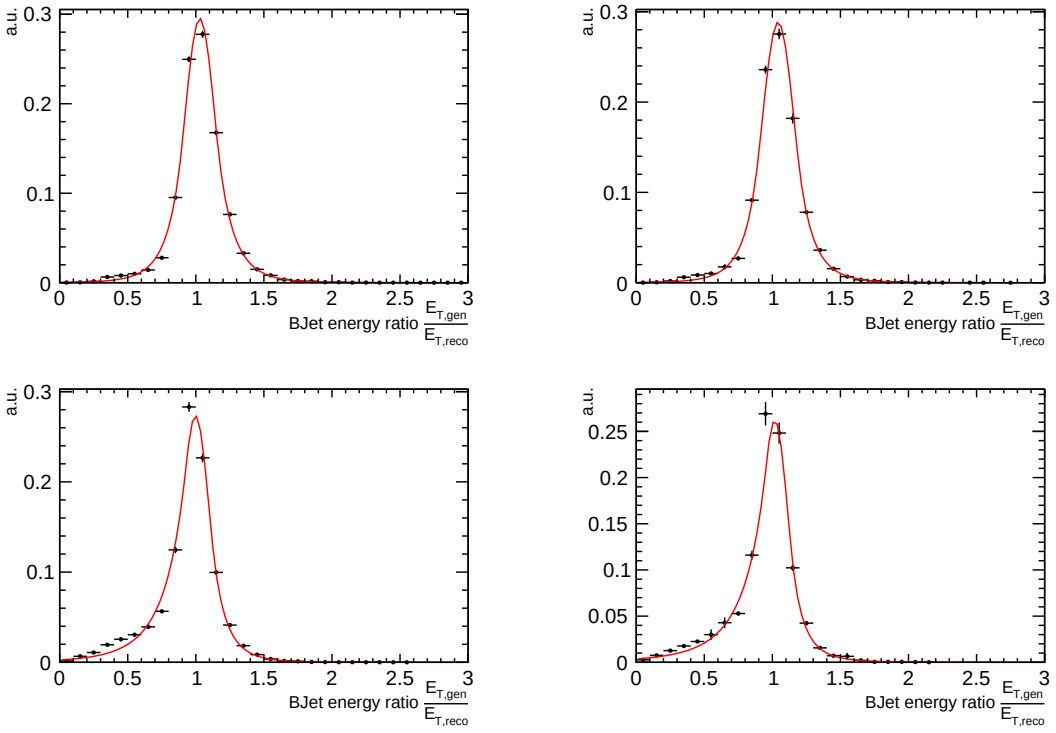

Figure A.3: Transverse b-jet-energy ratio $\frac{E_{\mathrm{T,gen}}}{E_{\mathrm{T,reco}}}$ fitted by a two-tailed crystal-ball function (Eq. 5.18) shown in red on a signal sample with a heavy Higgs boson mass of 300 GeV. The ratios are shown for jets with $|\eta| < 1.2$ (left) and $|\eta| \geq 1.2$ (right). The E_{T} range of the jets are , $80\,\mathrm{GeV} < E_{\mathrm{T}} < 120\,\mathrm{GeV}$ (top) and $E_{\mathrm{T}} > 120\,\mathrm{GeV}$ (bottom).

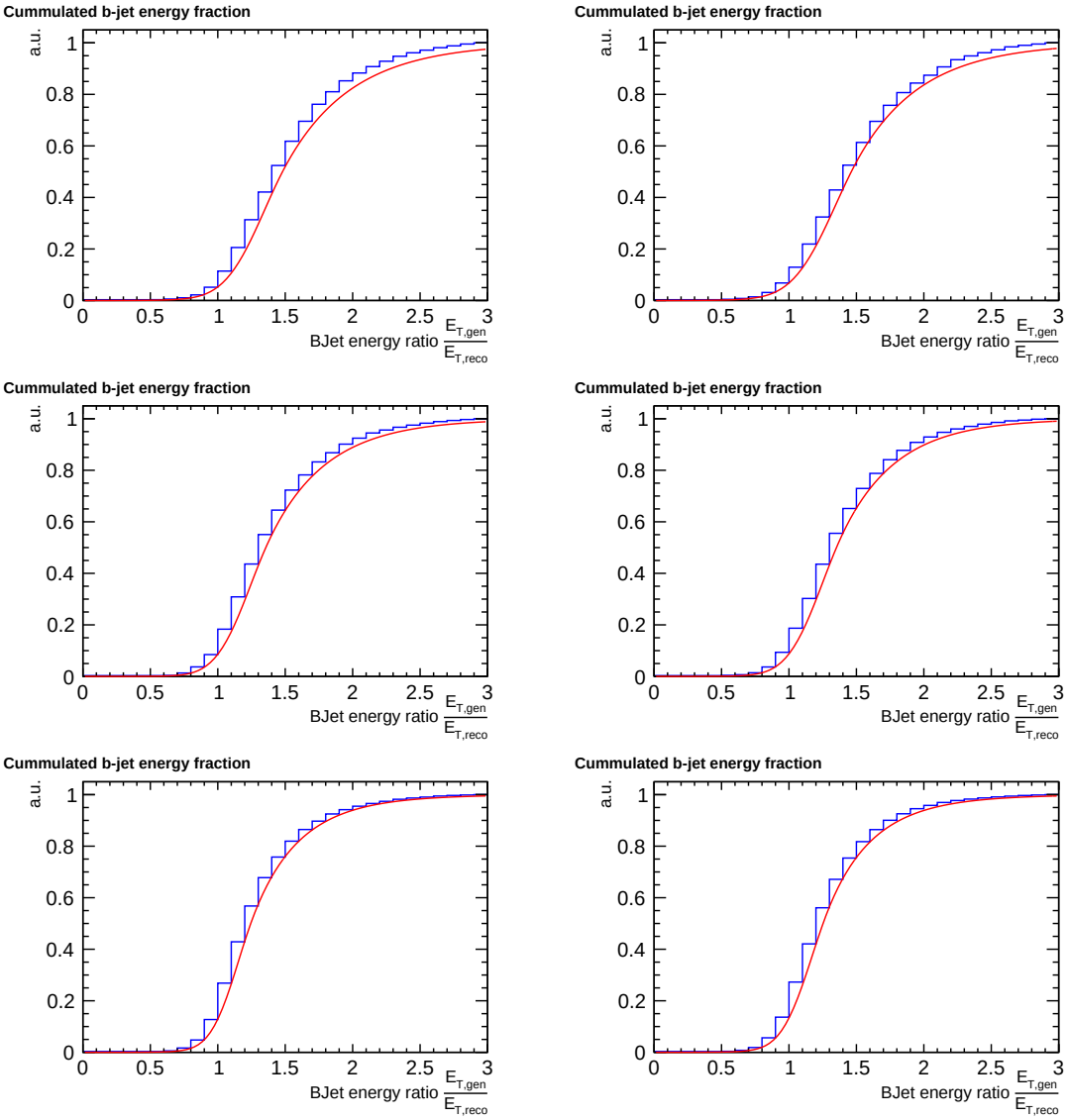

Figure A.4: Cumulative distribution functions (CDF) corresponding to the probability density functions (PDF) shown in Fig. A.1. The red line is the integral of the fitted two-tailed crystal-ball function. The CDFs are shown for jets with $|\eta| < 1.2$ (left) and $|\eta| \geq 1.2$ (right). The E_{T} range of the jets are $E_{\mathrm{T}} < 25\,\mathrm{GeV}$ (top), $25\,\mathrm{GeV} < E_{\mathrm{T}} < 30\,\mathrm{GeV}$ (middle) and $30\,\mathrm{GeV} < E_{\mathrm{T}} < 40\,\mathrm{GeV}$ (bottom).

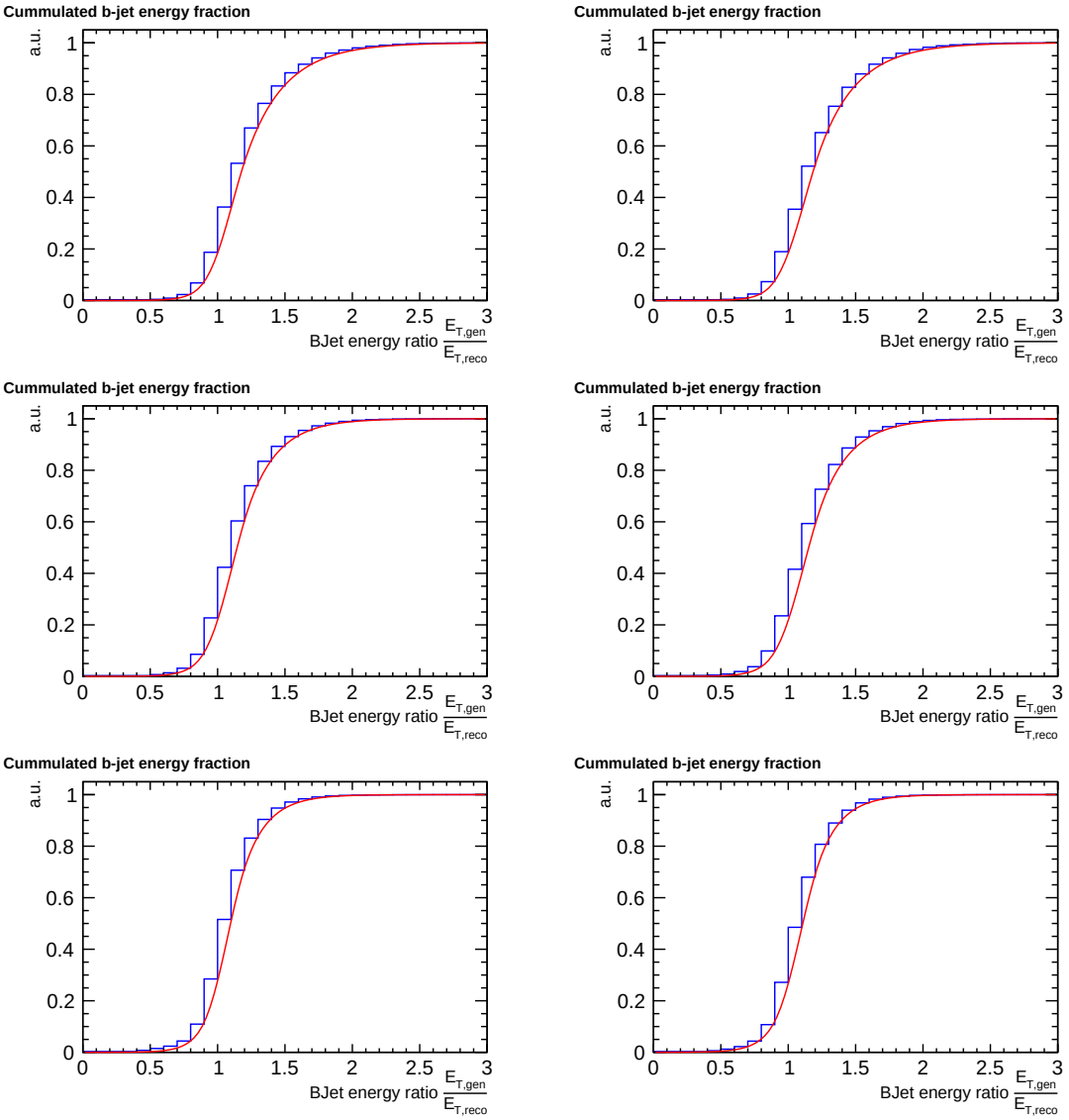

Figure A.5: Cumulative distribution functions (CDF) corresponding to the probability density functions (PDF) shown in Fig. A.2. The red line is the integral of the fitted two-tailed crystal-ball function. The CDFs are shown for jets with $|\eta| < 1.2$ (left) and $|\eta| \geq 1.2$ (right). The E_{T} range of the jets are $40\,\mathrm{GeV} < E_{\mathrm{T}} < 50\,\mathrm{GeV}$ (top), $50\,\mathrm{GeV} < E_{\mathrm{T}} < 60\,\mathrm{GeV}$ (middle) and $60\,\mathrm{GeV} < E_{\mathrm{T}} < 80\,\mathrm{GeV}$ (bottom).

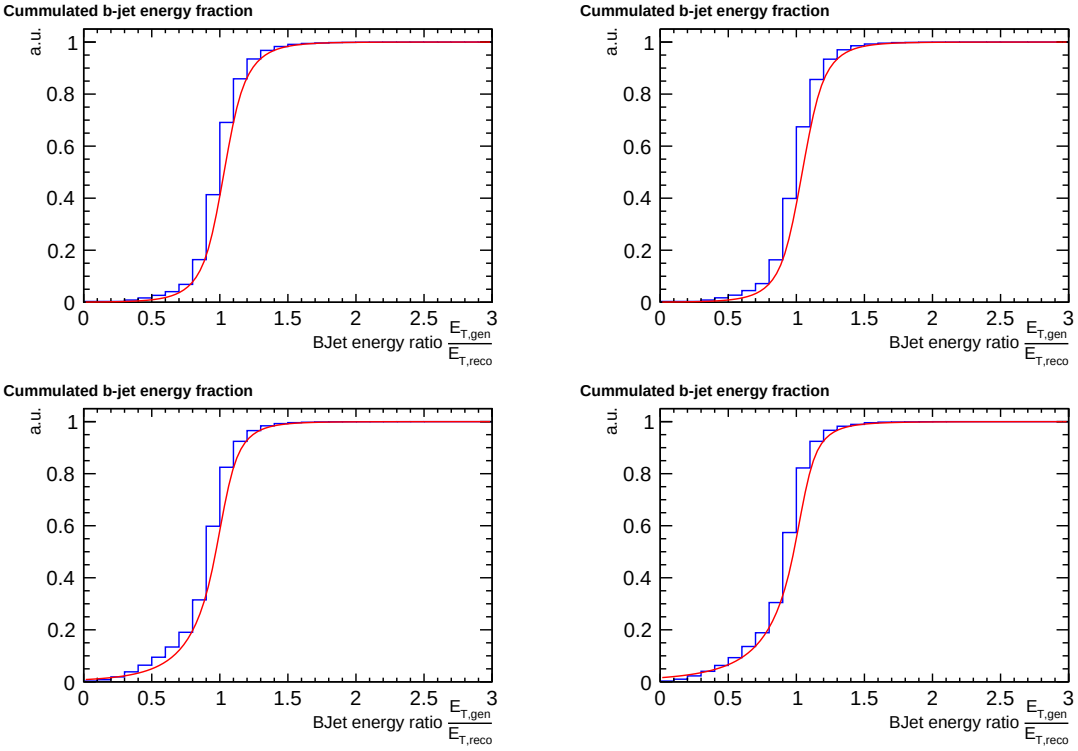

Figure A.6: Cumulative distribution functions (CDF) corresponding to the probability density functions (PDF) shown in Fig. A.3. The red line is the integral of the fitted two-tailed crystal-ball function. The CDFs are shown for jets with $|\eta| < 1.2$ (left) and $|\eta| \geq 1.2$ (right). The E_{T} range of the jets are $80\,\mathrm{GeV} < E_{\mathrm{T}} < 120\,\mathrm{GeV}$ (top) and $E_{\mathrm{T}} > 120\,\mathrm{GeV}$ (bottom).

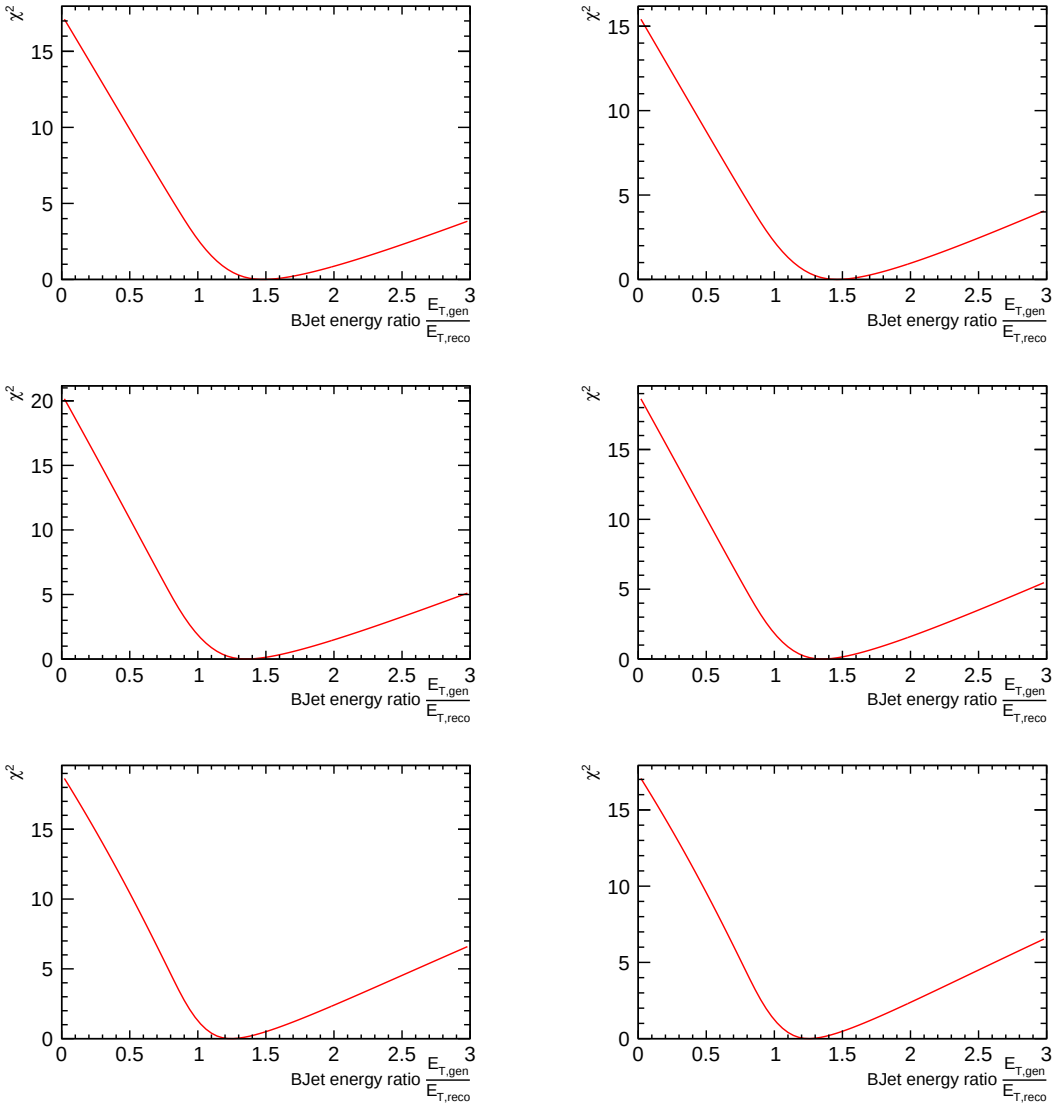

Figure A.7: χ^2 functions corresponding to the cumulative distribution functions (CDF) shown in Fig. A.4. The χ^2 functions were calculated according to 5.20. The functions are shown for jets with $|\eta| < 1.2$ (left) and $|\eta| \geq 1.2$ (right). The E_T range of the jets are $E_\mathrm{T} < 25\,\mathrm{GeV}$ (top), $25\,\mathrm{GeV} < E_\mathrm{T} < 30\,\mathrm{GeV}$ (middle) and $30\,\mathrm{GeV} < E_\mathrm{T} < 40\,\mathrm{GeV}$ (bottom).

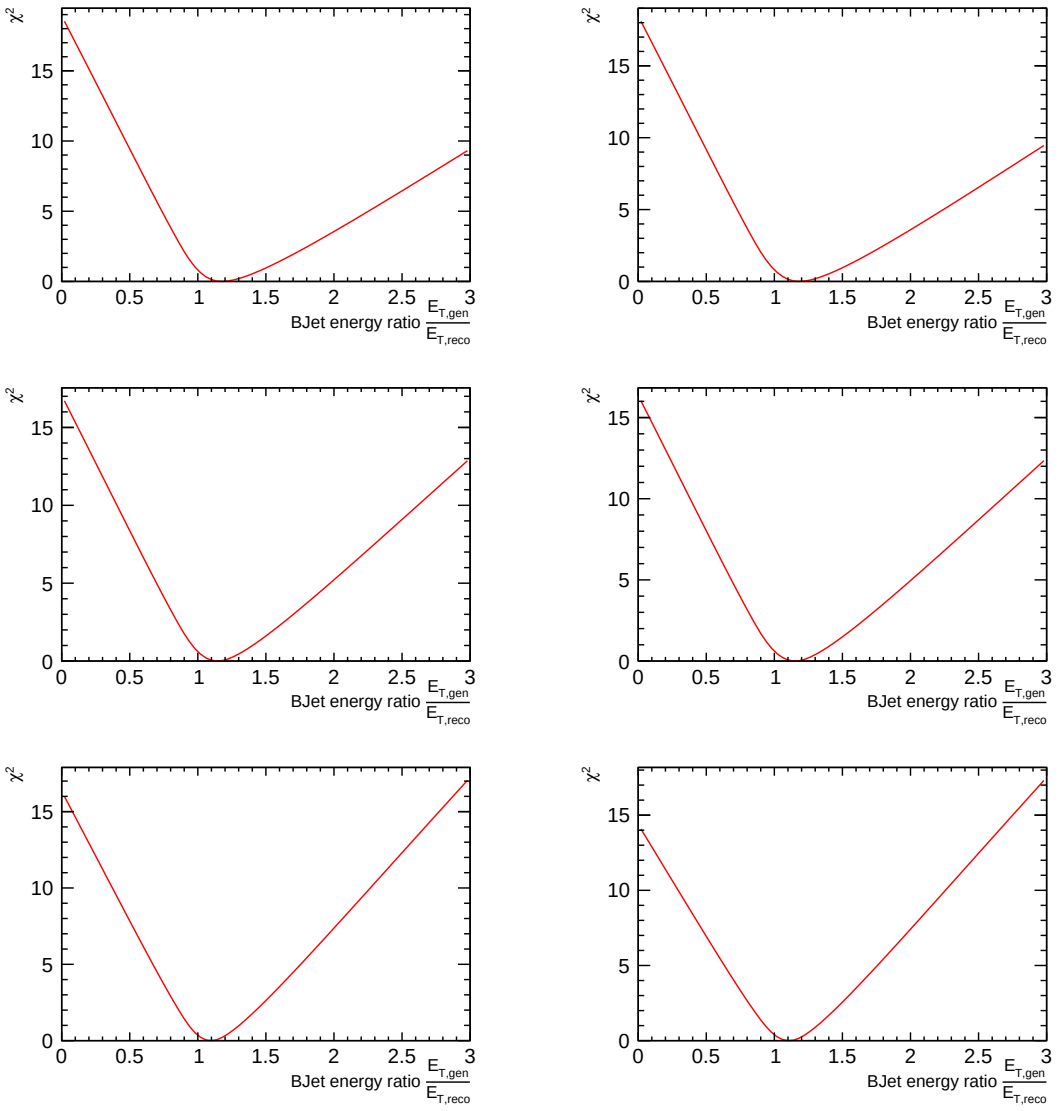

Figure A.8: χ^2 functions corresponding to the cumulative distribution functions (CDF) shown in Fig. A.5. The χ^2 functions were calculated according to 5.20. The functions are shown for jets with $|\eta| < 1.2$ (left) and $|\eta| \geq 1.2$ (right). The E_T range of the jets are $40\,\mathrm{GeV} < E_\mathrm{T} < 50\,\mathrm{GeV}$ (top), $50\,\mathrm{GeV} < E_\mathrm{T} < 60\,\mathrm{GeV}$ (middle) and $60\,\mathrm{GeV} < E_\mathrm{T} < 80\,\mathrm{GeV}$ (bottom).

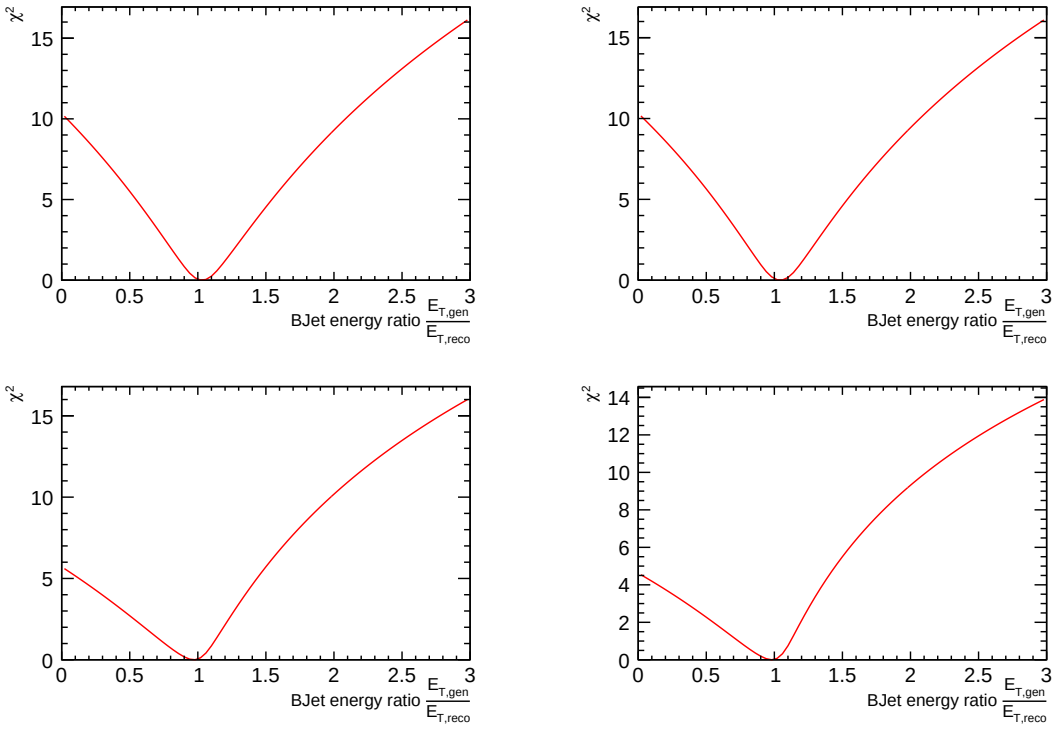

Figure A.9: χ^2 functions corresponding to the cumulative distribution functions (CDF) shown in Fig. A.6. The χ^2 functions were calculated according to 5.20. The functions are shown for jets with $|\eta| < 1.2$ (left) and $|\eta| \geq 1.2$ (right). The E_T range of the jets are $80\,\mathrm{GeV} < E_\mathrm{T} < 120\,\mathrm{GeV}$ (top) and $E_\mathrm{T} > 120\,\mathrm{GeV}$ (bottom).

A.2 Correlations of Cut-Optimization Observables

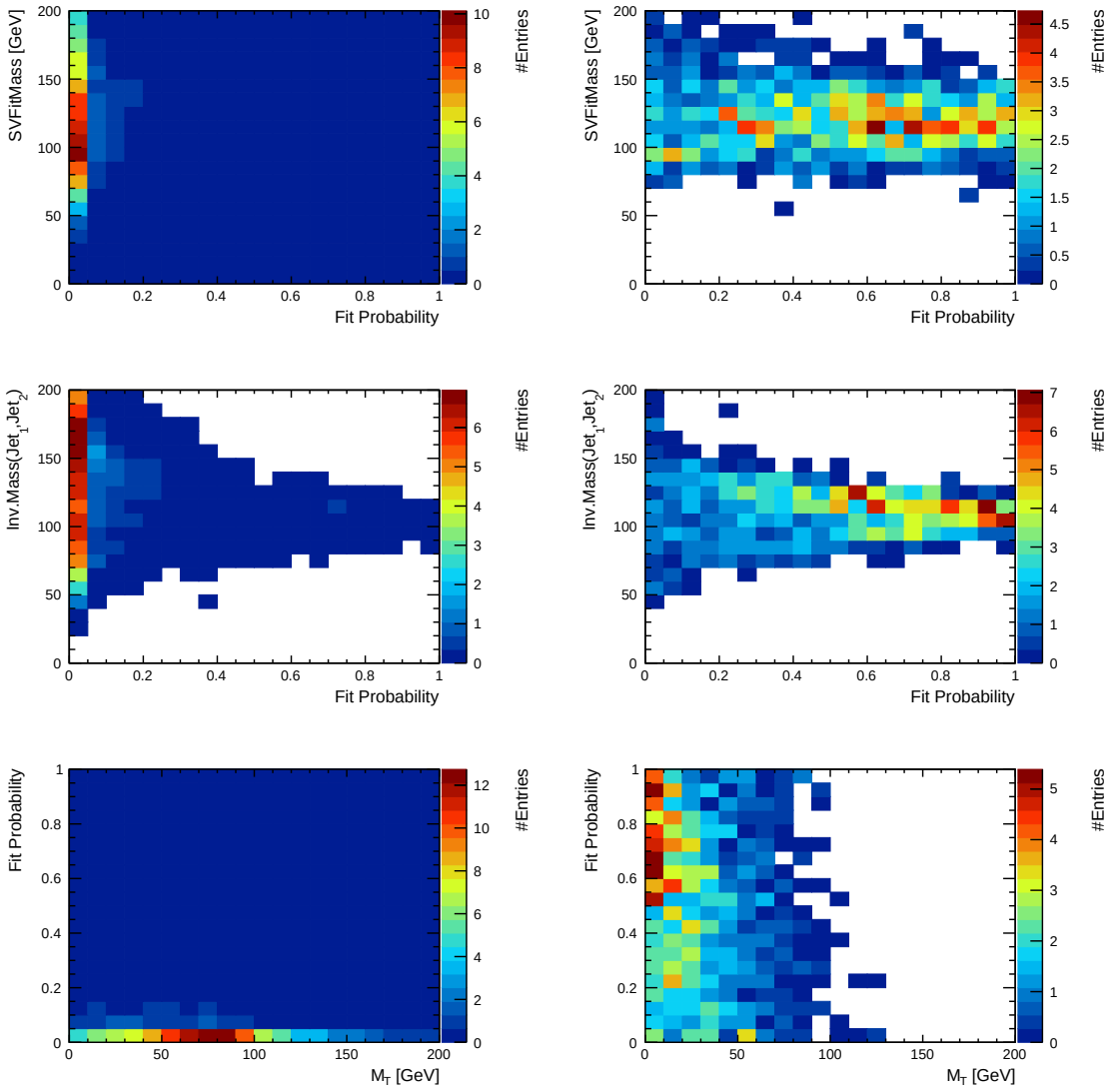

Figure A.10: Correlations for events with a reconstructed heavy Higgs boson mass of 290 GeV$< m_H <$ 310 GeV and at least two b-tagged jets for background events (left) and signal events (right) for a signal with a simulated heavy Higgs boson mass of 300 GeV. The plots show correlation between the fit probability and the SVFit mass (top), the invariant mass of the di-jet system (middle) and the transverse, invariant mass (bottom).

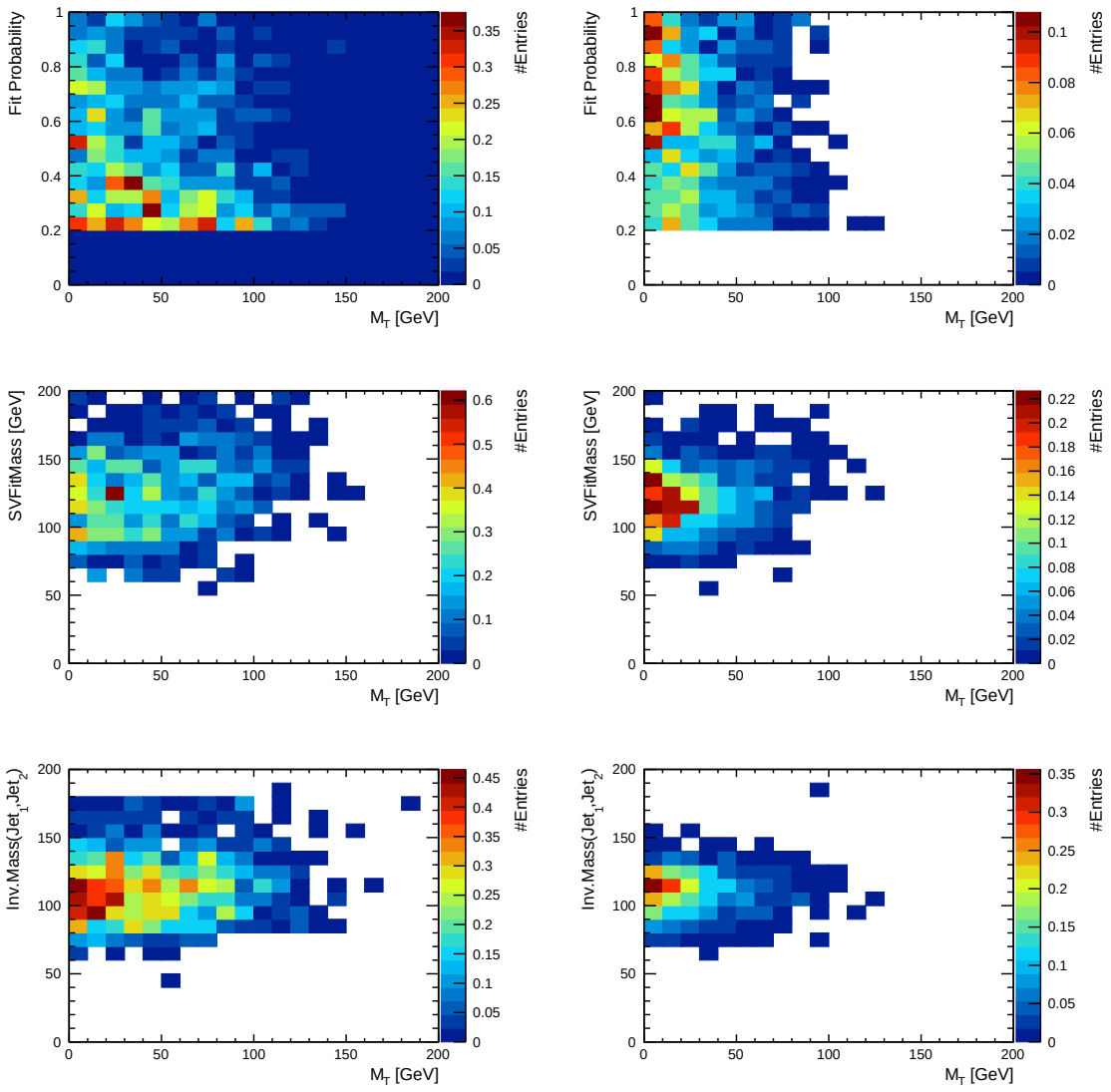

Figure A.11: Correlations for events with a reconstructed heavy Higgs boson mass of 290 GeV$< m_H <$ 310 GeV, an invariant di-jet mass of $m_{\mathrm{inv}}(\mathrm{jet}_1, \mathrm{jet}_2) > 70$ GeV and at least two b-tagged jets after the probability cut as as shown in Fig. 6.16 has been applied. Correlations are shown for background events (left) and signal events (right) for a signal with a simulated heavy Higgs boson mass of 300 GeV. The plots show correlations between the transverse, invariant mass and the fit probability (top), SVFit mass (middle) and the invariant mass of the di-jet system (bottom).

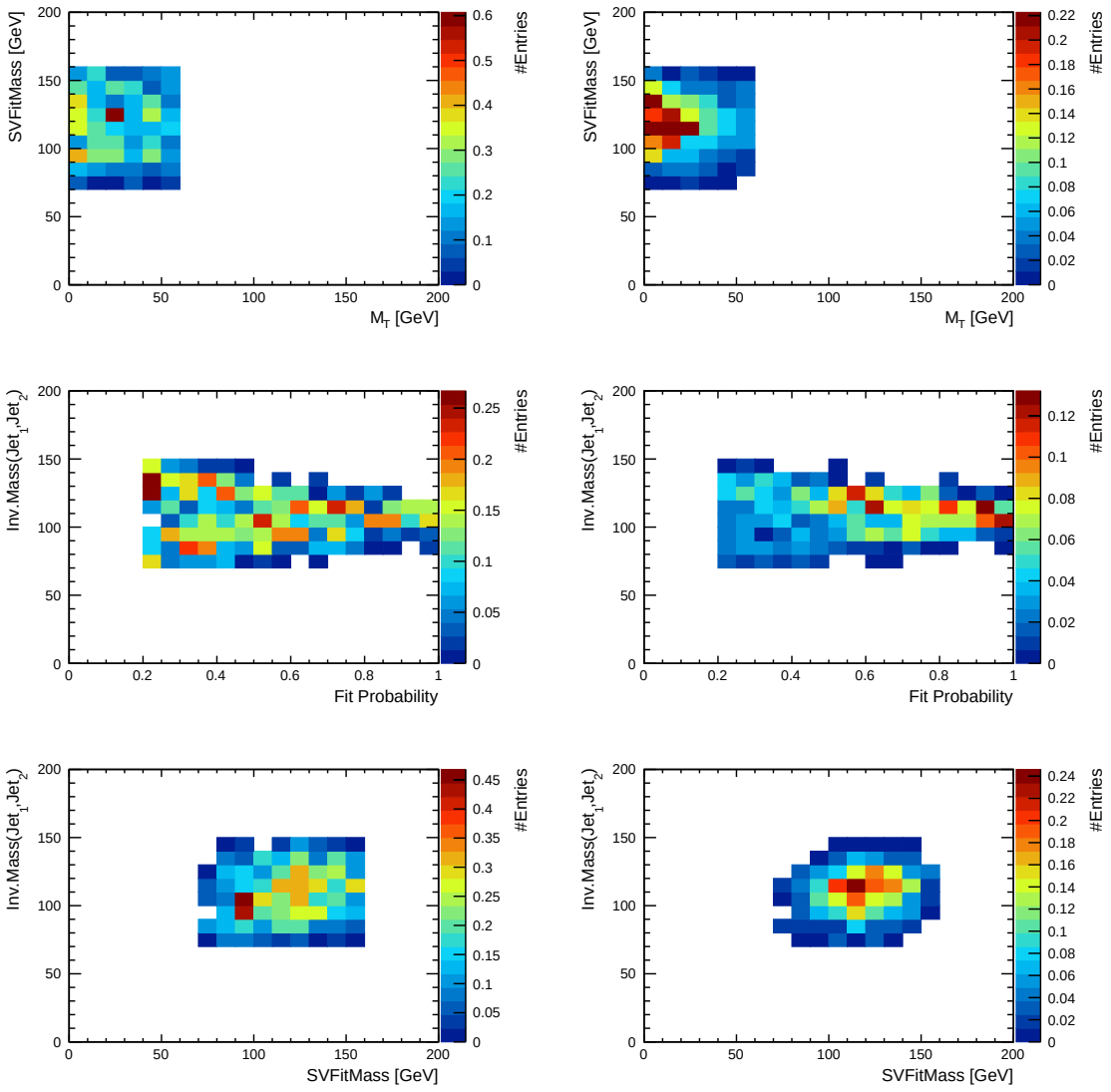

Figure A.12: Correlations for events with a reconstructed heavy Higgs boson mass of 290 GeV$< m_H <$ 310 GeV and at least two b-tagged jets after all cuts have been applied. Correlations are shown for background events (left) and signal events (right) for a signal with a simulated heavy Higgs boson mass of 300 GeV. The plots show correlations between the transverse, invariant mass and the SVFit mass (top), the fit probability and the invariant mass of the di-jet system (middle) and the SVFit mass and the invariant mass of the di-jet system (bottom).

Bibliography

[1] C. Collaboration, "Searches for a heavy scalar boson h decaying to a pair of 125 gev higgs bosons hh or for a heavy pseudoscalar boson a decaying to zh, in the final states with h to tautau," arXiv:1510.01181.

[2] CMS Collaboration, "Search for resonant Higgs boson pair production in the $b\bar{b}\tau^{+}\tau^{-}$ final state,".

[3] ATLAS and CMS Collaborations, "Combined Measurement of the Higgs Boson Mass in pp Collisions at $\sqrt{s} = 7$ and 8 TeV with the ATLAS and CMS Experiments," arXiv:1503.07589.

[4] H. Spiesberger and M. Spira and P. M. Zerwas, "The standard model: Physical basis and scattering experiments," arXiv:hep-ph/0011255.

[5] M. Hoffmann, "Search for Supersymmetry in final states with photons, jets and missing energy,".

[6] P. D. G. Berkeley, "Review of Particle Physics, 2014-2015," *Chin. Phys. C 38 (2014) 090001* (2014) , arXiv:1412.1408.

[7] http://en.wikipedia.org/wiki/StandardModel.

[8] F. Englert, R. Brout, "Broken Symmetry and the Mass of Gauge Vector Mesons," *Phys.Rev.Lett. 13 321-323* (1964) .

[9] Peter W. Higgs, "Broken symmetries, massless particles and gauge fields," *Phys.Lett. 12 132-133* (1964) .

[10] Peter W. Higgs, "Broken Symmetries and the Masses of Gauge Bosons," *Phys.Rev.Lett. 13 508-509* (1964) .

[11] "The nobel prize in physics 2004." https://www.nobelprize.org/nobel_prizes/physics/laureates/2004/popular.html.

[12] http://de.wikipedia.org/wiki/Supersymmetrie.

[13] E. W. Kolb and M. S. Turner, *The early universe.* Westview Press, 1990.

[14] J. Ellis, J. Hagelin, D.V. Nanopoulos, K. Olive, M. Srednicki, "Supersymmetric relics from the big bang," *Nuclear Physics B 238 (435)* (1984) .

[15] Stephen P. Martin, "A Supersymmetry Primer," `arXiv:hep-ph/9709356`.

[16] Marcela Carena and Howard E. Haber, "Higgs Boson Theory and Phenomenology," `arXiv:hep-ph/0208209`.

[17] Damien M. Pierce, Jonathan A. Bagger, Konstantin T. Matchev, Ren-Jie Zhang, "Precision Corrections in the Minimal Supersymmetric Standard Model," `arXiv:hep-ph/9606211`.

[18] Lawrence J. Hall, David Pinner, Joshua T. Ruderman, "A Natural SUSY Higgs Near 125 GeV," `arXiv:1112.2703`.

[19] Abdelhak Djouadi and Jeremie Quevillon, "The MSSM Higgs sector at a high MSUSY: reopening the low $\tan\beta$ regime and heavy Higgs searches," `arXiv:1304.1787`.

[20] Nima Arkani-Hamed, Savas Dimopoulos, "Supersymmetric Unification Without Low Energy Supersymmetry And Signatures for Fine-Tuning at the LHC," `arXiv:hep-th/0405159`.

[21] Lawrence J. Hall, Yasunori Nomura, "A Finely-Predicted Higgs Boson Mass from A Finely-Tuned Weak Scale," `arXiv:0910.2235`.

[22] J. Ellis, T. Falk, K.A. Olive, Y. Santoso, "Exploration of the MSSM with Non-Universal Higgs Masses," `arXiv:hep-ph/0210205`.

[23] Ernesto Arganda, J. Lorenzo Diaz-Cruz, Alejandro Szynkman, "Decays of H^0/A^0 in supersymmetric scenarios with heavy sfermions," `arXiv:1211.0163`.

[24] L Maiani, AD Polosa, V Riquer, "Bounds to the Higgs Sector Masses in Minimal Supersymmetry from LHC Data," `arXiv:1305.2172`.

[25] A. Djouadi, L. Maiani, G. Moreau, A. Polosa, J. Quevillon, V. Riquer, "The post-Higgs MSSM scenario: Habemus MSSM?," `arXiv:1307.5205`.

[26] A. Djouadi, L. Maiani, A. Polosa, J. Quevillon, V. Riquer, "Fully covering the MSSM Higgs sector at the LHC," `arXiv:1502.05653`.

[27] Bagnaschi, Emanuele (DESY) ; Frensch, Felix (Karlsruhe, Inst. Technol.) ; Heinemeyer, Sven (Cantabria Inst. of Phys.) ; Lee, Gabriel (Technion) ; Liebler, Stefan Rainer (DESY) ; Muhlleitner, Milada (Karlsruhe, Inst. Technol.) ; Mc Carn, Allison Renae (Michigan U.) ; Quevillon, Jeremie (King's Coll. London) ;

Rompotis, Nikolaos (Seattle U.) ; Slavich, Pietro (Paris, LPTHE) ; Spira, Michael (PSI, Villigen) ; Wagner, Carlos (Chicago U., EFI ; Chicago U., KICP ; Argonne) ; Wolf, Roger (Karlsruhe, Inst. Technol.), "Benchmark scenarios for low tan β in the MSSM,".

[28] CMS Collaboration, "Summary results of high mass BSM Higgs searches using CMS run-I data," *CMS-PAS-HIG-16-007* (2016) .

[29] `https://twiki.cern.ch/twiki/bin/view/LHCPhysics/LHCHXSWGMSSMNeutral`.

[30] A. Djouadi, J. Kalinowski, M. Spira, "HDECAY: a Program for Higgs Boson Decays in the Standard Model and its Supersymmetric Extension," *Comput.Phys.Commun.108:56-74,1998* (1997) , `arXiv:hep-ph/9704448`.

[31] A. Djouadi, M.M. Muhlleitner, M. Spira, "Decays of Supersymmetric Particles: the program SUSY-HIT (SUspect-SdecaY-Hdecay-InTerface)," *Acta Phys.Polon.B38:635-644,2007* (2006) , `arXiv:hep-ph/0609292`.

[32] G. C. Branco, P. M. Ferreira, L. Lavoura, M. N. Rebelo, Marc Sher, Joao P. Silva, "Theory and phenomenology of two-Higgs-doublet models," `arXiv:1106.0034`.

[33] Jihn E. Kim, "Light pseudoscalars, particle physics and cosmology," *Phys. Rep. 150* (1987) .

[34] Mark Trodden, "Electroweak Baryogenesis: A Brief Review," *CWRU-P18-98* (1998) , `arXiv:hep-ph/9805252`.

[35] Sheldon L. Glashow and Steven Weinberg, "Natural conservation laws for neutral currents," *Phys. Rev. D 15, 1958* (1977) .

[36] Emmanuel A. Paschos, "Diagonal neutral currents," *Phys. Rev. D 15, 1966* (1977) .

[37] Howard E. Haber, Oscar Stal, "New LHC Benchmarks for the CP-conserving Two-Higgs-Doublet Model," *Eur.Phys. J. C75 (2015) 491* (2015) , `arXiv:1507.04281`.

[38] Robert V. Harlander, Stefan Liebler, Hendrik Mantler (Wuppertal U.), "SusHi: A program for the calculation of Higgs production in gluon fusion and bottom-quark annihilation in the Standard Model and the MSSM," *Comput.Phys.Commun. 184 (2013) 1605-1617* (2012) .

[39] K.G. Chetyrkin, Johann H. Kuhn (Karlsruhe U., TTP) , M. Steinhauser (Hamburg U.) , "RunDec: A Mathematica package for running and decoupling of the strong coupling and quark masses," *Comput.Phys.Commun. 133 (2000) 43-65* (2000) .

[40] Robert Harlander, Philipp Kant (Karlsruhe U., TTP) , "Higgs production and decay: Analytic results at next-to-leading order QCD," *JHEP 0512 (2005) 015* (2005) .

[41] David Eriksson, Johan Rathsman, Oscar Stal (Uppsala U.) , "2HDMC: Two-Higgs-Doublet Model Calculator Physics and Manual," *Comput.Phys.Commun. 181 (2010) 189-205* (2009) .

[42] R. Bonciani (LPSC, Grenoble) , G. Degrassi (Rome III U. and INFN, Rome3) , A. Vicini (Milan U. and INFN, Milan), "On the Generalized Harmonic Polylogarithms of One Complex Variable," *Comput.Phys.Commun. 182 (2011) 1253-1264* (2010) .

[43] U. Aglietti (Rome U. and INFN, Rome) , R. Bonciani (Freiburg U.) , G. Degrassi (Rome III U. and INFN, Rome3) , A. Vicini (Milan U. and INFN, Milan) , "Two loop light fermion contribution to Higgs production and decays," *Phys.Lett. B595 (2004) 432-441* (2004) .

[44] Robert V. Harlander (CERN) , William B. Kilgore (Brookhaven), "Higgs boson production in bottom quark fusion at next-to-next-to leading order," *Phys.Rev. D68 (2003) 013001* (2003) .

[45] Robert V. Harlander (CERN) , William B. Kilgore (Brookhaven) , "Next-to-next-to-leading order Higgs production at hadron colliders," *Phys.Rev.Lett. 88 (2002) 201801* (2002) .

[46] Robert V. Harlander (RWTH Aachen U.) , Stefan Liebler (DESY) , Hendrik Mantler (Karlsruhe U., ITP and KIT, Karlsruhe, IKP), "SusHi Bento: Beyond NNLO and the heavy-top limit," *DESY-16-061* (2016) , `arXiv:1605.03190`.

[47] L. Evans and P. Bryant, "LHC Machine," *JINST 3 S08001* (2008) .

[48] CERN, "The four main LHC experiments." `http://cdsweb.cern.ch/record/40525`.

[49] ATLAS Collaboration, "The ATLAS Experiment at the CERN Large Hadron Collider," *JINST 3 S08003* (2008) .

[50] CMS Collaboration, "The CMS experiment at the CERN LHC ," *JINST 3 S08004* (2008) .

[51] ALICE Collaboration, "The ALICE experiment at the CERN LHC," *JINST 3 S08002* (2008) .

[52] LHCb Collaboration, "The LHCb Detector at the LHC," *JINST 3 S08005* (2008) .

[53] C. C. ATLAS, "Combined measurement of the higgs boson mass in pp collisions at $\sqrt{s} = 7$ and 8 tev with the atlas and cms experiments," arXiv:1503.07589.

[54] CMS Collaboration, "CMS Luminosity - Public Results." https://twiki.cern.ch/twiki/bin/view/CMSPublic/LumiPublicResults.

[55] C. Collaboration, "Cms tracking performance results from early lhc operation," arXiv:1007.1988.

[56] CMS Collaboration, "Images of the CMS ECAL Barrel." http://cdsweb.cern.ch/record/1431477.

[57] CMS ECAL/HCAL Collaborations, "The CMS barrel calorimeter response to particle beams from 2 to 350 GeV/c," *Eur. Phys. J. C60* (2009) .

[58] CMS Collaboration, "Images of the CMS HCAL Barrel." http://cdsweb.cern.ch/record/1431485.

[59] CMS Collaboration, "Images of CMS Muons - Drift Tubes." http://cdsweb.cern.ch/record/1431514.

[60] CMS Collaboration, "CMS TriDAS project: Technical Design Report," *CERN-LHCC-2000-038* (2011) .

[61] The CMS Trigger and Data Acquisition Group, "The CMS High Level Trigger," arXiv:hep-ex/0512077.

[62] CMS Collaboration, "Particle-Flow Event Reconstruction in CMS and Performance for Jets, Taus, and MET," *CMS-PAS-PFT-09-001* (2009) . http://cdsweb.cern.ch/record/1194487.

[63] C. Collaboration, "Performance of CMS muon reconstruction in pp collision events at sqrt(s) = 7 TeV," *CMS-MUO-10-004; CERN-PH-EP-2012-173* (2013) , arXiv:1206.4071.

[64] Gavin P. Salam, "Towards jetography," arXiv:0906.1833.

[65] Matteo Cacciari and Gavin P. Salam and Gregory Soyez, "The anti-k_t jet clustering algorithm," arXiv:0802.1189.

[66] CMS Collaboration, "Determination of jet energy calibration and transverse momentum resolution in cms," arXiv:1107.4277.

[67] C. Collaboration, "Identification of b-quark jets with the CMS experiment," arXiv:1211.4462.

[68] C. Collaboration, "Identification of b quark jets at the CMS Experiment in the LHC Run 2,".

[69] CMS Collaboration, "Performance of tau-lepton reconstruction and identification in cms," *JINST 7 (2012) P01001* (2011) , arXiv:1109.6034.

[70] Bianchini, Lorenzo and Conway, John and Friis, Evan Klose and Veelken, Christian, "Reconstruction of the Higgs mass in $H \to \tau\tau$ Events by Dynamical Likelihood techniques," *J. Phys. Conf. Ser.* (2014) .

[71] M. L. N. T. Daniele Bertolini, Philip Harris, "Pileup Per Particle Identification," arXiv:1407.6013.

[72] A. Dominguez, D. Abbaneo, K. Arndt, N. Bacchetta, A. Ball, E. Bartz, W. Bertl, G. M. Bilei, G. Bolla, H. W. K. Cheung, M. Chertok, S. Costa, N. Demaria, A. Dominguez, K. Ecklund, W. Erdmann, K. Gill, G. Hall, K. Harder, F. Hartmann, R. Horisberger, W. Johns, H. C. Kaestli, K. Klein, D. Kotlinski, S. Kwan, M. Pesaresi, H. Postema, T. Rohe, C. Schäfer, A. Starodumov, S. Streuli, A. Tricomi, P. Tropea, J. Troska, F. Vasey, and W. Zeuner, "CMS Technical Design Report for the Pixel Detector Upgrade," Tech. Rep. CERN-LHCC-2012-016. CMS-TDR-11, CERN, Geneva, Sep, 2012. https://cds.cern.ch/record/1481838.

[73] W. ERDMANN, "THE CMS PIXEL DETECTOR," *Int. J. Mod. Phys. A* **25** no. 07, (Mar, 2010) 1315–1337. http://dx.doi.org/10.1142/S0217751X10049098.

[74] S. Spannagel, "Test Beam Measurements for the Upgrade of the CMS Pixel Detector and Measurement of the Top Quark Mass from Differential Cross Sections," 2015.

[75] I.-M. G. T. H. U. K. I.-A. M.-P. N. M. J. M. F. S. Ties Behnke, Erika Garutti, "Test Beams at Desy," *EUDET-Memo-2007-11* (2007) . http://www.eudet.org/e26/e28/e182/e283/eudet-memo-2007-11.pdf.

[76] E. Consortium, "Infrastructure for detector research and development towards the international linear collider," 2012.

[77] C. Hu-Guo, J. Baudot, G. Bertolone, A. Besson, A.S. Brogna, C. Colledani, G. Claus, R. De Masi (Strasbourg, IPHC) , Y. Degerli (DAPNIA, Saclay) , A. Dorokhov et al., "First reticule size MAPS with digital output and integrated zero suppression for the EUDET-JRA1 beam telescope," 2010.

[78] Simon Spannagel and Hendrik Jansen, "GBL Track Resolution Calculator," 2014.

[79] E. Corrin, "EUDAQ Software User Manual," 2010.

[80] Spannagel, Simon (DESY) ; Meier, Beat (PSI, Villigen) ; Perrey, Hanno Christopher (DESY), "The pxarCore Library - Technical Documentation, Reference Manual, and Sample Applications," 2015.

[81] V. Blobel, "A new fast track-fit algorithm based on broken lines," 2006.

[82] Claus Kleinwort, "General Broken Lines as advanced track fitting method," 2012.

[83] I. Rubinskiy, "EUTelescope. Offline track reconstruction and DUT analysis software.," 2010.

[84] S. S. for the CMS Collaboration, "Test beam campaigns for the cms phase i upgrade pixel readout chip," 2014.

[85] University of Hamburg Higgs Group, "HHKinFit – a kinematic fitting package to fit heavy Higgs decays," *unpublished* (2014) .

[86] B. Vormwald, "From Neutrino Physics to Beam Polarisation - a High Precision Story at the ILC,".

[87] The ATLAS and CMS Collaborations and The LHC Higgs Combination Group, "Procedure for the LHC Higgs boson search combination in Summer 2011,".

[88] Read, A L, "Modified frequentist analysis of search results (the CL_s method)," *CERN-2000-005* (2000) .

[89] Glen Cowan, Kyle Cranmer, Eilam Gross, Ofer Vitells, "Asymptotic formulae for likelihood-based tests of new physics," *The European Physical Journal C* (2011) .

Declaration of Authorship

Eidesstattliche Versicherung

Hiermit erkläre ich an Eides statt, dass ich die vorliegende Dissertationsschrift selbst verfasst und keine anderen als die angegebenen Quellen und Hilfsmittel benutzt habe.

Hamburg, den: _____

Unterschrift: _____

Acknowledgements

I would like to thank all the people who helped me along the way during my time as a PhD student.
Foremost I want to thank Peter Schleper, who was always able to point me in the right direction when I was stuck, managed to motivate me with fresh ideas when things were moving slowly and provided a very friendly working atmosphere.
I have to also thank Alexei Raspereza, the second referre for my dissertation for beeing available on such short notice.
I thank all members of my examination comission, consisting of Erika Garutti, Johannes Haller, Alexei Raspereza, Peter Schleper and Günter Sigl for beeing available for this task.
There were many people whithout whom this thesis would not have been possible. Benedikt Vormwald was always available to talk through and to elaborate on ideas and problems and gave invaluable comments on every part of my thesis. Daniel Tröndle was one of the developers of the framework I used day in and day out for my thesis and helped immensely by answering all of my technical questions. I was often able to benefit from the fruitful comments made by Adrian Perieanu on my work.
Erika Garutti guided me through my time in the detector lab and was always able to nudge me in the right direction. Valentina Sola, Daniel Pitzl and Simon Spannagel provided additional important support during my time at the DESY testbeam.
I thank Hartmut Stadie for taking me on as a member of the computing team.
I also want to thank all of the members of the UHH Particle Physics and Detector Development group for providing a great working atmosphere. In this regard I have to give some special thanks to my trusty lunch companions Daniele Marconi, Marek Niedziela and Lukas Vanelderen.
Ich möchte weiterhin all meinen Freunden in Hamburg und anderswo für ihre Unterstützung in dieser Zeit danken.
Ich danke all meinen Verwandten, welche meine Arbeit als Physiker stets mit Interesse verfolgt haben. Insbesondere meinen Schwestern Anna und Sandra und meiner Oma Anni gebühren besonderer Dank fr ihre Unterstützung auf meinem Weg.
Meinen Eltern Helga und Bernd danke ich dafür, mich immer ermutigt zu haben mir meine eigenen Ziele zu setzen und für meine mir heiligste geborgene Kindheit in der ich mich zu dem Menschen entwickeln konnte, der ich heute bin.
Der größte Dank geht an meine Frau Caroline. Danke, dass du mich wieder aufgerichtet hast, wenn ich mal frustriert war und dafür, dass du dich so aufopferungsvoll für unser Team eingesetzt hast.
Vielen Dank Emmy, für die extra Portion Sonnenschein welche ich an den letzten Tage meiner Doktorarbeit gut gebrauchen konnte.